

Tools for Electromagnetic Field Simulation in the
KATRIN Experiment

by

Thomas Joseph Corona

Submitted to the Department of Physics
in partial fulfillment of the requirements for the degree of

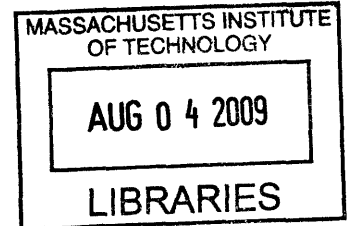
Master of Science

at the

MASSACHUSETTS INSTITUTE OF TECHNOLOGY

February 2009

© Massachusetts Institute of Technology 2009. All rights reserved.



ARCHIVES

Author
.....
Department of Physics
December 1, 2008

Certified by
.....
Joseph Formaggio
Assistant Professor
Thesis Supervisor

Accepted by
.....
Thomas J. Greytak
Associate Department Head for Education

Tools for Electromagnetic Field Simulation in the KATRIN Experiment

by

Thomas Joseph Corona

Submitted to the Department of Physics
on December 1, 2008, in partial fulfillment of the
requirements for the degree of
Master of Science

Abstract

The Karlsruhe Tritium Neutrino (KATRIN) experiment is a tritium beta decay experiment designed to make a direct, model independent measurement of the electron neutrino mass. To accomplish this task, the experiment employs precisely defined electric and magnetic fields for particle transport and mass spectroscopy. In order to simulate particle trajectories in the experiment, it is essential to have methods for calculating these fields quickly and accurately. The application of the methods of direct elliptic integral calculation, zonal harmonic expansion and interpolation from an adaptive-refinement field mesh is described within the object-oriented `KatrinField` framework, as well as an analysis of their comparative strengths and weaknesses in reproducing the electromagnetic fields found in KATRIN.

Thesis Supervisor: Joseph Formaggio
Title: Assistant Professor

Acknowledgments

I owe my deepest gratitude to my advisor Dr. Joseph Formaggio for providing me with equal measures of guidance, compassion and encouragement throughout my tenure at MIT, and to Dr. Ferenc Glück of KIT, whose genius in the field of computational physics is equalled by his warmth and willingness to help others who share a passion for his pursuits. I am also indebted to the members of the Neutrino and Dark Matter Group at MIT, and most especially Dr. Benjamin Monreal, Dr. Michael Miller and Richard Ott, for their tireless enthusiasm, advice and their willingness to lend me their technical expertise on almost every subject imaginable. I am grateful towards the Neutrino Group at Duke University for instilling in me a profound love and appreciation towards neutrino physics. Finally, I would like to thank my family, whose continual love and support have carried me through my most difficult times and have helped me to achieve more than I have ever thought possible.

Contents

1	Introduction	15
1.1	Motivation for measurement of the neutrino mass	15
1.1.1	Evidence for neutrino mass from flavor oscillation	15
1.1.2	Significance of neutrino mass	18
1.2	Tritium β decay experiments	22
1.2.1	Kinematics of tritium β decay	22
1.2.2	Signature of massive $\bar{\nu}_e$	24
1.2.3	Impact on neutrino physics theory	24
1.3	Summary	25
2	The KATRIN Experiment	26
2.1	Introduction	26
2.2	Tritium Source and β Transport System	26
2.3	Pre- and Main Spectrometers	27
2.3.1	Properties of a MAC-E-Filter	27
2.3.2	KATRIN MAC-E Filters	32
2.4	Detector	35
2.5	The role of simulation in electrode and magnet design	36
3	Direct Calculation of Electric and Magnetic Fields	38
3.1	Introduction	38
3.2	Boundary Element Method	39
3.2.1	General description of the Boundary Element Method	39

3.2.2	Definitions	40
3.2.3	Derivation from Green's second identity	40
3.2.4	Singularities	41
3.2.5	Extending R_{Σ} to ∞	44
3.2.6	Connection to indirect BEM	45
3.2.7	Relation to electrostatics	48
3.3	Electrostatics	49
3.3.1	Introduction	49
3.3.2	Geometry Primitives	49
3.3.3	Implementation of the indirect BEM with electrode primitives	58
3.4	Magnetostatics	58
3.4.1	Introduction	58
3.4.2	Geometry Primitives	59
3.5	Summary	66
4	Calculation of Electric and Magnetic Fields via Zonal Harmonic Ex-	
	pansion	67
4.1	Introduction	67
4.2	Legendre polynomials in electrostatics	68
4.2.1	Regions of convergence	68
4.2.2	Derivation of electric field components from electric potential .	70
4.2.3	Calculating Source Constants	72
4.3	Legendre polynomials in magnetostatics	78
4.3.1	Regions of convergence	79
4.3.2	Derivation of magnetic field components from magnetic scalar potential	80
4.3.3	Calculating Source Constants	81
4.4	Summary	88
5	Field Interpolation with an Adaptive Refinement Field Map	89
5.1	Introduction	89

5.1.1	Features of current routines	89
5.1.2	General features of a field map	90
5.2	Interpolation technique	91
5.2.1	Reduced multivariate Hermite interpolation	91
5.2.2	Features of the interpolator	92
5.2.3	Derivation of the interpolator in d dimensions	92
5.3	Adaptive-Refinement Field Map	96
5.3.1	General technique	96
5.3.2	Quad-trees and oct-trees	97
5.3.3	Constructing the field map	98
5.4	Summary	100
6	Validation	101
6.1	Introduction	101
6.2	BEM and direct calculation tests	101
6.3	Comparison between direct calculation and zonal harmonic methods .	105
6.4	Field map tests	107
6.5	Summary	107
7	Conclusion	109
A	Formulae for the potential of a right triangular sub-element	111
B	Zonal Harmonic Expansion Relations	115
B.1	Recursion relation for the remote source points of a solenoid	115
B.2	Relating the boundary conditions for a solenoid to the boundary conditions for two rings at its edges	117
C	KatrinField	120
C.1	Components of KatrinField	121
C.1.1	Geometry	121
C.1.2	Elliptic	125

C.1.3 Legendre 125
C.1.4 FieldMap 126
C.1.5 Field 127
C.2 Summary 128

List of Figures

1-1	Feynman diagram for $0\nu\beta\beta$. This interaction is only allowed if the neutrino is its own antiparticle (i.e. Majorana).	20
1-2	(A) The normal and (B) inverted hierarchy configurations for the neutrino mass eigenstates. In each representation, the mass eigenstates are represented as a composite of the flavor states according to the MNS matrix.	21
1-3	The (A) total and (B) endpoint of the electron energy spectrum of tritium β decay for $m_\nu = 0$ eV and $m_\nu = 1$ eV. The shaded region denotes the measurable difference between the massive and massless neutrino spectra (representing only 2×10^{-13} of the total β spectrum). Images taken from [28].	24
2-1	A schematic of the KATRIN beamline, including the windowless gaseous tritium source (WGTS), the rear system and the β transport system.	27
2-2	General setup of a MAC-E-Filter. (Top) experimental configuration and (bottom) the adiabatic momentum transformation of charged particle through the filter.	29
2-3	Graphical description of the transmission function of a MAC-E filter.	32
2-4	Schematic of the inner wire electrodes in the pre-spectrometer. Similar wire electrodes are present in the main spectrometer.	32
2-5	Schematic of the pre-spectrometer.	33
2-6	Schematic of the electromagnetic configuration of the main spectrometer.	34

2-7	Image of the segmented detector.	35
2-8	Equipotential lines at the exit of the pre-spectrometer. Image taken from [28].	36
3-1	A graphical depiction of the regions Ω (in white) and Σ (in grey). \vec{n} describes the unit normal vector to the boundaries (Γ_Ω and Γ_Σ) of these regions, and \vec{r} is the observation point.	40
3-2	By including a small Γ_ϵ , we are able to avoid the divergence of $W(\vec{r})$. Taking the limit as $\epsilon \rightarrow 0$, we recover our original domain.	42
3-3	By deforming Γ_Ω to include a small circular segment of radius ϵ , we are able to avoid the singularity of $\nabla^2 W(\vec{r})$ at the boundary. Taking the limit as $\epsilon \rightarrow 0$, we recover our original boundary.	43
3-4	The equivalent figure to 3-1 for internal problems. The shaded region denotes the domain of interest for computation.	46
3-5	Discretization of Γ_Ω into n sub-elements for numerical computation. Charge densities are constant along a sub-element.	47
3-6	A charged line segment with endpoints \vec{x}_1 and \vec{x}_2 and charge density λ , and a field point \vec{P} with minimal distance z from the infinite line on which the line segment is located (the point of intersection is labeled \vec{x}_0). Distances between the field point and x_1 and x_2 are r_1 and r_2 , respectively.	50
3-7	A rectangular sub-element defined by the position of a corner \vec{P}_0 , the lengths of the sides a and b , and the unit vectors in the directions of sides a and b , labeled \vec{n}_1 and \vec{n}_2 . The field point is defined as \vec{P} , with local coordinates (u_p, v_p, w_p) . An arbitrary point \vec{Q} located on the surface of the sub-element is shown, with local coordinates $(u, v, 0)$. The distance between \vec{P} and \vec{Q} is z	52

3-8	A right triangular sub-element defined by the position of the corner opposite the hypotenuse \vec{P}_0 , the lengths of the sides a and b , and the unit vectors in the directions of sides a and b , labeled \vec{n}_1 and \vec{n}_2 . The field point is defined as \vec{P} , with local coordinates $(0, 0, z)$. The corners of the triangle are recast into local coordinates to facilitate integration.	53
3-9	A ring sub-element in an axially symmetric system, defined by the generating point (R, Z) and charge Q . The field point is located at \vec{P} .	55
3-10	A conic section sub-element defined by the generating line connecting the points (R_a, Z_a) and (R_b, Z_b) , and surface charge density σ . The field point is defined as \vec{P} .	57
3-11	A circular current loop with current \vec{I} , generating point (R, Z) , and an off-axis field point (r, z) .	60
3-12	A solenoid with a circular cross-section of radius R , with endpoints at Z_a and Z_b , axial surface current \vec{K} , and an off-axis field point (r, z) .	63
3-13	A thick coil with volume current density \vec{J} , generated by rotating a rectangle with corners (R_a, Z_a) and (R_b, Z_b) about the z -axis, and an off-axis field point (r, z) .	65
4-1	(A) A 3-dimensional rendering of an axially symmetric charged cylindrical electrode and (B) the regions of convergence for central and remote zonal harmonic expansion from a source point S .	69
4-2	Graphical depiction of a charged ring with generating point (R, Z) , a central source point (S) , and an arbitrary on-axis field point (F) .	73
4-3	Graphical depiction of a charged ring with generating point (R, Z) , a remote source point (S) , and an arbitrary on-axis field point (F) .	75
4-4	Graphical depiction of a charged conic section generated by the line connecting (R_a, Z_a) and (R_b, Z_b) with length L , and a central source point (S) .	76
4-5	(A) An axially symmetric wire configuration and (B) its electrode approximation.	77

4-6	(A) A 3-dimensional rendering of an axially symmetric magnetic coil and (B) the regions of convergence for central and remote zonal harmonic expansion from a source point S	79
4-7	Graphical depiction of a current loop with generating point (R, Z) , a central source point (S) , and an arbitrary on-axis field point (F) . . .	82
4-8	Graphical depiction of a current loop with generating point (R, Z) , a remote source point (S) , and an arbitrary on-axis field point (F) . . .	83
4-9	Graphical depiction of a solenoid generated by the line connecting (R, Z_a) and (R, Z_b) with surface current density \vec{k} , and a central source point (S)	85
4-10	Graphical depiction of a thick coil generated by the rectangle with corners (R_a, Z_a) and (R_b, Z_b) with volume current density \vec{J} , and a central source point (S)	87
5-1	For $d = 3$, a cube centered at the origin with sides of length 2 used for interpolation. Axes are labeled as \hat{i} , $i = 1, 2, 3$. Vertices are labeled as \vec{u}_j , $j = 1, 2, \dots, 8$	93
5-2	For $d = 3$, a depiction of a parent cube and its 8 subcubes.	97
5-3	For $d = 2$, (A) an example of an adaptive refinement field mesh and (B) its corresponding quad-tree. In (B), Shaded regions represent boxes where the error of interpolation is acceptable for computation, and white regions represent boxes that required further splitting. Though only the shaded boxes are used for field computation (assuring a uniform maximal error), the white boxes are kept in the tree to facilitate the searching process.	98
B-1	(A) A 3-dimensional rendering of an axially symmetric solenoid and (B) the regions of convergence for central zonal harmonic expansion of the z and r -components of the magnetic field from a source point S . In both images, $(Z_a - z_0) = (z_0 - Z_b)$ (in other words, the source point is located in the middle of the geometries).	117

- C-1 A graphical representation of magnetic coils that share different axes. 124
- C-2 A graphical representation of the central regions of convergence for three source points. Within each region of convergence, the coefficients corresponding to the nearest source point can be used in an expansion to solve for the fields. By using multiple source points, the technique of zonal harmonic expansion can be applied in a larger region of space. 126

List of Tables

1.1	Current limits on the mass squared differences of the neutrino.	18
2.1	Magnet specifications for the WGTS and β -transport system.	28
2.2	(A) Wires placed inside the main spectrometer, in order to deflect incident negatively charged particles. (B) A module holding wire electrodes. (C) Wire module placement in the main spectrometer. Images taken from [32].	34
3.1	Conversion from the input parameters of a thick coil to the parameters used in the calculation of its field.	65
5.1	Features of field computation methods (assuming that the desired accuracy from each method is equivalent)	91
6.1	(A) Measurement of the capacitance of a unit disc by discretizing the disc into concentric circles with decreasing thicknesses at the edge and center. (B) Comparative accuracy of the computed capacitance and (C) the time of computation with respect to the number of circular sub-elements.	102
6.2	(A) Measurement of the capacitance of a unit cube by discretizing the cube faces into rectangles with decreasing areas at the edges. (B) Comparative accuracy of the computed capacitance and (C) the time of computation with respect to the number of rectangle sub-elements. (D) Same test as performed in (B), but with each rectangle split into two right triangles.	103

6.3	A comparison of the direct computation method for a cylinder described by conic sections and by rectangles. Figure (A): The difference between the electric potential values for the two geometries. Figure (B): The difference between the magnitude of the computed \vec{E} -field values for the two geometries. Figure (C): The angle θ between the computed \vec{E} -field vectors for the two geometries.	104
6.4	Figure (A): Comparison of the direct and zonal harmonic field computation techniques for a cylinder electrode. Figure (B): The difference between the two methods' values for computing the electric potential. Figure (C): The difference between the magnitude of the \vec{E} -field computed by the two methods. Figure (D): The angle θ between the two \vec{E} -field vectors computed by the two methods.	105
6.5	Figure (A): Comparison of the direct and zonal harmonic field computation techniques for a thick coil magnet. Figure (B): The difference between the magnitude of the \vec{B} -field computed by the two methods. Figure (C): The angle θ between the two \vec{B} -field vectors computed by the two methods.	106
6.6	A 2-dimensional field map, with tolerance 10^{-6} and 8 levels of cube splitting, of a sample function. Figure (A): an image of the original function. Figure (B): the original function with an overlay of the field map cubes. Figure (C): an image of the difference between the original and interpolated field values.	108
C.1	Available geometry primitives.	122
C.2	Table of available parameters to be set by the user.	128

Chapter 1

Introduction

1.1 Motivation for measurement of the neutrino mass

1.1.1 Evidence for neutrino mass from flavor oscillation

The canonical Standard Model of particle physics, a theory that has successfully predicted the experimental results of almost all particle physics experiments in the past thirty years, presupposes the neutrino to be massless. Several experiments performed within the past decade have uncovered compelling evidence to the contrary, linking the mass of the neutrino to an observable phenomenon known as *flavor oscillation*. In the commonly accepted 3-neutrino model, flavor oscillation is the result of a neutrino interacting according to its flavor eigenstates ($|\nu_\alpha\rangle$, $\alpha = e, \mu, \tau$) and propagating through space according to its mass eigenstates ($|\nu_i\rangle$, $i = 1, 2, 3$). The mass and flavor eigenstates of a neutrino are related by the unitary Maki-Nakagawa-Sakata (MNS) matrix $U_{\alpha i}$:

$$|\nu_i\rangle = \sum_{\alpha} U_{\alpha i} |\nu_\alpha\rangle. \quad (1.1)$$

When a neutrino is created, it is in a flavor eigenstate ($|\nu_\alpha\rangle$). As it propagates through space, it becomes a time-varying superposition of the three flavor eigenstates ($|\nu(t)\rangle = \sum_{\alpha} C_{\alpha}(t) |\nu_\alpha\rangle$) whose amplitudes $C_{\alpha}(t)$ are determined by components of the MNS ^{α} matrix, the time of propagation, the momentum of the neutrino and

the mass squared differences between neutrino mass eigenstates. Upon detection via *charged-current* weak interaction¹, the neutrino wave function collapses back into one of the three flavor eigenstates with the probability $P(\nu_\alpha)(t) = |C_\alpha(t)|^2$.

In the case of two-flavor oscillations, $U_{\alpha i}$ can be represented as a simple rotation matrix dependent upon a single mixing angle θ , and the probability of neutrino oscillation is expressed as

$$P(\nu_\alpha \rightarrow \nu_\beta) = \sin^2(2\theta) \times \sin^2\left(\frac{1.27\Delta m_{12}^2 L}{E}\right), \quad (1.2)$$

where $\Delta m_{12}^2 = m_1^2 - m_2^2$ is the mass squared difference of the mass eigenstates in eV^2 , $L = c \cdot t$ is the distance from the neutrino's creation to detection in kilometers, and E is the neutrino energy in GeV [1]. For three-flavor oscillations for Dirac neutrinos, there are six parameters intrinsic to the neutrino that determine its oscillatory properties: two mass squared differences ($\Delta m_{21}^2 \simeq \Delta m_\odot^2$, $\Delta m_{32}^2 \simeq \Delta m_{atm}^2$), three mixing angles (θ_{12} , θ_{23} , and θ_{13}), and a CP violating phase (δ).

Experimental Observation of Neutrino Oscillation

Common sources for the experimental measurement of neutrino oscillation are neutrinos created in the Earth's atmosphere, neutrinos created from fusion reactions within the sun, and neutrino production from nuclear reactors and particle accelerators. Due to the different parameters present in these sources (such as varying energy spectra and differing baselines), experiments measuring neutrino oscillation from these different sources will have different sensitivities to the physical parameters $\sin^2(2\theta)$ and Δm^2 described in Equation 1.2. In addition, these experiments can quantify neutrino oscillations by either an excess or deficit in the expected neutrino flux from a given source, classifying these experiments as "appearance" and "disappearance" experiments.

Measurements of the solar neutrino flux have been ongoing since the late 1960's [2]. Using both radiochemical and real-time detection methods, a deficit in the solar

¹an interaction mitigated by a W^\pm boson

ν_e flux has been confirmed to high precision in several experiments, including the Homestake experiment [2], SAGE [3], Gallex [4], Kamiokande and SuperKamiokande [5] [6]. In 2001, the SNO collaboration finally solved the solar ν_e deficit problem by measuring both the ν_e and total ν ($\nu_e + \nu_\mu + \nu_\tau$) solar fluxes, and confirmed that, while the total ν flux is consistent with theoretical prediction, there is a substantial deficit in the solar ν_e flux [7]. The observation was a strong indicator for ν_e oscillation and was later confirmed by the KamLAND experiment [8], setting the most competitive limits on Δm_{\odot}^2 to date (see Table 1.1).

The dominant process for the creation of atmospheric neutrinos is from charged pion decay in the upper atmosphere,

$$\pi^\pm \rightarrow \mu^\pm + \nu_\mu (\bar{\nu}_\mu), \quad (1.3)$$

which creates a muon and a neutrino. The muon then decays:

$$\mu^\pm \rightarrow \bar{\nu}_\mu (\nu_\mu) + e^\pm + \nu_e (\bar{\nu}_e), \quad (1.4)$$

producing an electron, a muon neutrino and an electron neutrino. Due to these processes, the ratio of the flux of ν_μ to ν_e at the Earth's surface without oscillation should be approximately 2 : 1. Several experiments, including NUSEX [9], Soudan [10], IBM [11], Frejus [12] and Kamiokande [5], measured a significant deficit in the expected ratio of atmospheric ν_μ to ν_e [6]. The best known limits on atmospheric ν_μ disappearance has been measured by Super-Kamiokande, providing evidence for ν_μ oscillation [13]. By employing directional analysis of the Super-K data in tandem with neutrino energy reconstruction, high statistics that covered a broad spectrum of $\frac{L}{E}$ values (see Eq. 1.2) were used to place limits on the atmospheric mass squared difference Δm_{atm}^2 . These results were later confirmed by the K2K experiment [14] and by MINOS [15], placing the best current limits on Δm_{atm}^2 (see Table 1.1). It is interesting to note that the current evidence for atmospheric ν_μ disappearance is at $> 15\sigma$ [16].

neutrino parameter	value	C.L.	experiment
θ_{atm}	$45^\circ \pm 8^\circ$	90%	Super-Kamiokande [13]
Δm_{atm}^2	$(2.86 \pm 0.32) \cdot 10^{-3} \text{ eV}^2$	90%	K2K [14], MINOS [15]
θ_\odot	$(34.4^{+1.3}_{-1.2})^\circ$	68%	SNO [17], KamLAND [8]
Δm_\odot^2	$(7.95 \pm 0.55) \cdot 10^{-5} \text{ eV}^2$	68%	KamLAND [8]
θ_{13}	$< 10^\circ$		CHOOZ [18]

Table 1.1: Current limits on the mass squared differences of the neutrino.

1.1.2 Significance of neutrino mass

By measuring nonzero splittings between the mass eigenstates, neutrino oscillation implies that at least two of the three neutrinos are not massless. The evidence of massive neutrinos has given rise to several interesting questions in neutrino physics theory. The three most prominent questions related to neutrino mass are:

- are neutrinos *Dirac* (ν and $\bar{\nu}$ are distinct) or *Majorana* ($\nu = \bar{\nu}$) particles,
- what is the ordering of the mass eigenstates, and
- what is the overall scale of the neutrino masses?

While the KATRIN experiment is designed to measure the overall scale of the neutrino masses, a brief description of these three topics is given in order to provide a more complete understanding of the implications of massive neutrinos.

Neutrinos as Dirac & Majorana particles

In the standard model representation, the mass coupling is represented by the second term in the Dirac Lagrangian:

$$\mathcal{L} = \bar{\Psi}(i\gamma^\mu\partial_\mu - m_D)\Psi = 0, \quad (1.5)$$

where γ^μ represents the μ -th Dirac matrix, and Ψ is a Dirac spinor representing the spin states of the particle and antiparticle. Since Ψ can be represented as a sum of chiral eigenstates,

$$\Psi = (P_L + P_R)\Psi = \Psi_L + \Psi_R, \quad (1.6)$$

the mass term in Equation 1.5 can be rewritten as

$$\mathcal{L}^D = m_D \bar{\Psi} \Psi = m_D (\bar{\Psi}_R \Psi_L + \bar{\Psi}_L \Psi_R), \quad (1.7)$$

where the terms $\bar{\Psi}_R \Psi_R$ and $\bar{\Psi}_L \Psi_L$ necessarily vanish due to the properties of the chiral projection operator ($\bar{P}_{L/R} = P_{R/L}$, $P_L P_R = 0$), and m_D must be real. Since the canonical Standard Model precludes the existence of right-handed neutrinos (Ψ_R , $\bar{\Psi}_R$), the mass term vanishes, resulting in a description of the neutrino as massless [19].

One way to adjust the Standard Model to accommodate massive neutrinos is to purpose the existence of right-handed *sterile* neutrinos, whose properties justify their absence in experimental measurements to date. Another method describes the neutrino and antineutrino as the left and right-handed chiral states of a single Majorana neutrino [20]. To understand Majorana mass, we first construct a Majorana spinor entirely from Ψ_L : by noting that $\Psi_R^c = C \bar{\Psi}_L^T$ Lorentz transforms identically to Ψ_R (where C is the charge conjugation operator), we can define $\Psi = \Psi_L + \Psi_R^c$ [21]. Using this spinor, we get a Lorentz-invariant mass term

$$\mathcal{L}^L = m_L (\bar{\Psi}_L \Psi_R^c + \bar{\Psi}_R^c \Psi_L) + h.c. \quad (1.8)$$

If we allow neutrinos to have both a Dirac and a Majorana mass, an additional mass term can be constructed from $\Psi = \Psi_L^c + \Psi_R$:

$$\mathcal{L}^R = m_R (\bar{\Psi}_L^c \Psi_R + \bar{\Psi}_R \Psi_L^c) + h.c. \quad (1.9)$$

In its most general form (containing both Majorana and Dirac mass terms), the neutrino mass can be represented as a combination of Equations 1.7, 1.8 and 1.9:

$$(\bar{\Psi}_L, \bar{\Psi}_L^c) \begin{pmatrix} m_L & m_D \\ m_D & m_R \end{pmatrix} \begin{pmatrix} \Psi_R^c \\ \Psi_R \end{pmatrix} + h.c. \quad (1.10)$$

The description of massive neutrinos as Majorana particles has many exciting

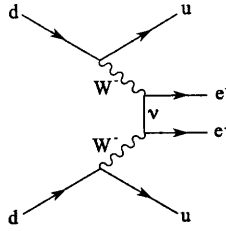


Figure 1-1: Feynman diagram for $0\nu\beta\beta$. This interaction is only allowed if the neutrino is its own antiparticle (i.e. Majorana).

implications in particle physics theory. See-saw theories involve the ratios of the intrinsic mass properties of the neutrino to provide justification for the unusually small neutrino mass. In addition, many theories that attempt to explain the matter/anti-matter asymmetry in the universe depend on Majorana nature of the neutrino. The description of the neutrino and antineutrino as two chirality states of the same particle also provides an explanation for why neutrinos and antineutrinos are only observed as left and right-handed, respectively, producing a theory that does not require the incorporation of heretofore unobserved neutrino states.

Several experiments designed to determine whether neutrinos are Majorana particles are currently in progress. These experiments exploit the fact that *neutrinoless double β -decay* ($0\nu\beta\beta$), a process that is forbidden in the canonical Standard Model but allowed if the neutrino is Majorana, has a distinctive energy signature that can be singled out in measurement. If observed, neutrinoless double β -decay will not only prove the Majorana nature of the neutrino, but will also be able to set competitive limits on the mass of the neutrino. Though, to date, there is no confirmed experimental evidence for neutrinos as Majorana particles², it is not difficult to understand the theory's appeal.

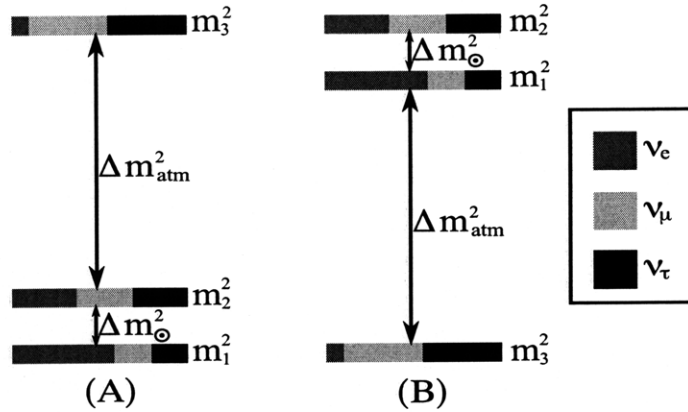


Figure 1-2: (A) The normal and (B) inverted hierarchy configurations for the neutrino mass eigenstates. In each representation, the mass eigenstates are represented as a composite of the flavor states according to the MNS matrix.

Hierarchy of the three neutrino masses

While neutrino oscillation experiments provide strong evidence for massive neutrinos, they are only sensitive to the differences between the mass eigenstates (rather than the masses themselves). Due to this fact, an ambiguity arises in the ordering of the mass eigenstates. Using the mass squared differences measured in neutrino oscillation experiments, two³ mass orderings are possible, referred to as *normal* and *inverted* hierarchies (see Fig. 1-2). In the normal hierarchy, $|\Delta m_{31}^2| > |\Delta m_{32}^2|$, while in the inverted hierarchy the inequality is reversed [24]. The normal hierarchy is so named because it roughly follows the mass hierarchy of the electron, muon and tau: m_1 , the most “e-like” mass eigenstate, is the lightest, while m_3 , the mass eigenstate that has the largest ratio of ν_τ , is the heaviest. Current experiments designed to determine which hierarchy is correct include NO ν A [25] and T2K [26]. Understanding the mass hierarchy will help to fill the gaps in our understanding of neutrino mass, and will result in more precise constraints on the mixing angles in the MNS matrix.

²Unconfirmed evidence for $0\nu\beta\beta$ decay has been reported by [22].

³The ordering of m_1^2 with respect to m_2^2 can be determined by the properties of solar neutrino measurements [23].

Absolute mass scale

A lower limit on the mass of the heaviest neutrino mass state is obtained by allowing the lightest mass state to be exactly zero. Since the largest mass squared difference is given in Table 1.1, we know the mass m of the heaviest neutrino to be

$$m > 0.045 \text{ eV} \tag{1.11}$$

Many models for massive neutrinos beyond the canonical Standard Model predict the absolute mass scale to be higher than this, however. In general, theoretical models that incorporate neutrino mass fall into two categories: a hierarchical mass spectrum (described in the previous Section), and a nearly degenerate spectrum⁴, where

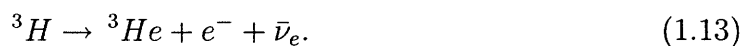
$$m_1 \approx m_2 \approx m_3 \tag{1.12}$$

and $m_i \geq 200 \text{ meV}$. Determining whether neutrinos are hierarchical or nearly degenerate has significant impact on particle theory in general, as it is believed that the absolute energy scale will dictate the scale of new physics beyond the standard model [27]. To date, the most precise theory-independent techniques for measuring the absolute neutrino mass scale involve studying the kinematics of tritium β decay [27].

1.2 Tritium β decay experiments

1.2.1 Kinematics of tritium β decay

Tritium β decay is described by the following reaction:



⁴The mass splittings measured in oscillation experiments are still valid in nearly degenerate models, but are orders of magnitude less than the absolute neutrino mass.

Noting that $\bar{\nu}_e$ is a superposition of the three mass eigenstates, the energy spectrum of the outgoing electron in this process is

$$\frac{dN}{dE} = C \times F(Z, E)p(E + m_e c^2)(E_0 - E) \sum_i |U_{ei}|^2 [(E_0 - E)^2 - m_i^2]^{\frac{1}{2}} \Theta(E_0 - E - m_i), \quad (1.14)$$

where E is the electron energy, m_e is the mass of the electron, p is the electron momentum, E_0 represents the maximum electron energy (corresponding to $m_\nu = 0$), $F(Z, E)$ is the Fermi function (accounting for the Coulomb interaction between the outgoing electron and the ${}^3\text{He}^+$ nucleus), $\Theta(E_0 - E - m_\nu)$ is the Heaviside step function (to ensure energy conservation), and

$$C = \frac{G_F^2}{2\pi^3} \cos^2 \theta_C |M|^2, \quad (1.15)$$

where G_F is the Fermi constant, θ_C is the Cabibbo angle and M is the nuclear matrix element [28]. Three properties of Equation 1.14 are particularly worthy of note, as we will refer back to them in subsequent sections: first, the measurement of the β energy spectrum is independent of whether the neutrino is Majorana or Dirac. Second, if the energy resolution of the experiment is less than the splittings between the mass eigenstates of the neutrino, the mass m_ν can be treated as a superposition of the neutrino mass eigenstates that comprise $\bar{\nu}_e$ [19]. In other words, we can replace m_ν^2 in Equation 1.14 with

$$m^2(\bar{\nu}_e) = \sum_i |U_{ei}|^2 m_i^2, \quad (1.16)$$

producing a single observable in experiment that is dependent upon all three neutrino mass eigenstates. Finally, the count rate of electrons near the end-point energy can be determined by Equation 1.14 to be proportional to $(E_0 - E)^3$, which quickly approaches zero at the endpoint.

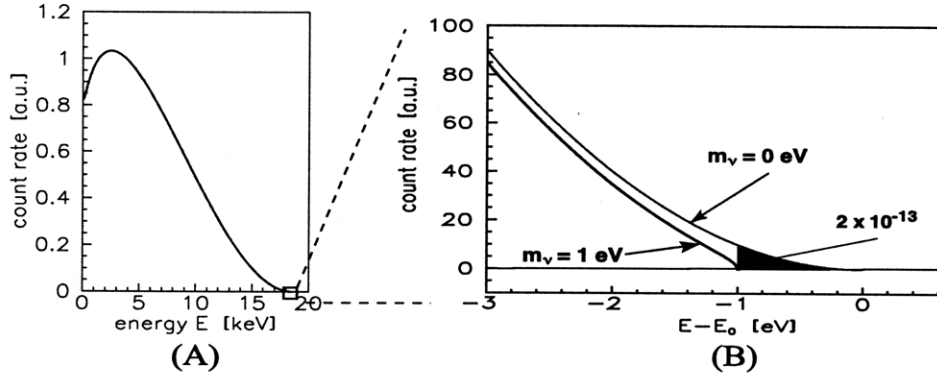


Figure 1-3: The (A) total and (B) endpoint of the electron energy spectrum of tritium β decay for $m_\nu = 0 \text{ eV}$ and $m_\nu = 1 \text{ eV}$. The shaded region denotes the measurable difference between the massive and massless neutrino spectra (representing only 2×10^{-13} of the total β spectrum). Images taken from [28].

1.2.2 Signature of massive $\bar{\nu}_e$

Using Equation 1.14, tritium β decay experiments measure the neutrino mass by calculating the variance of the endpoint of the electron energy spectrum from the $m_\nu = 0$ endpoint. As depicted in Figure 1-3, the fraction of events that result in the positive signature of a massive $\bar{\nu}_e$ is very small: for example, only 2×10^{-13} of the emitted β decays account for the last 1 eV of the spectrum. The ability to accurately obtain a signal for a significantly small neutrino mass is therefore strongly dependent upon the luminosity of the tritium source, as well as the ability to precisely filter the emitted electrons below a given energy threshold [28].

1.2.3 Impact on neutrino physics theory

Given the current range of sensitivities attainable by tritium β decay experiments, the presence (or absence) of a signal in an experiment of this type will yield important results to determining the nature of neutrino mass. If a signal is detected and a value for the mass m_ν can be determined to a given tolerance, we will be able to fix the absolute mass spectrum of the mass eigenstates. Because the splittings of the mass eigenstates are an order of magnitude smaller than the current sensitivity levels of tritium β decay experiments, the reconstructed neutrino mass will be a

weighted average of the three mass eigenstates according to Equation 1.16 and, while not sensitive to mass ordering, would determine that the neutrino masses are nearly degenerate. Such a measurement could also be used in tandem with $0\nu\beta\beta$ experiments to determine whether neutrinos are Majorana particles. The absence of a signal would result in the most competitive limit on the absolute neutrino mass scale to date.

1.3 Summary

In the past decade we have been witness to a complete paradigm shift in our understanding of neutrinos. The confirmation of the theory of neutrino oscillation has raised as many questions as it has answered, as the task of accommodating massive neutrinos in the Standard Model that fit experimental measurements is a nontrivial task. At present, the questions of the Majorana versus Dirac nature of neutrinos, the ordering of the neutrino mass hierarchy and the absolute neutrino mass scale comprise the bulk of the remaining questions to be answered in neutrino physics. Tritium β decay experiments are currently the most competitive method for determining the absolute neutrino mass scale, whose determination would help to solve the remaining outstanding questions surrounding the neutrino mass.

Chapter 2

The KATRIN Experiment

2.1 Introduction

The Karlsruhe Tritium Neutrino Experiment (KATRIN) is a next-generation tritium β -decay experiment in Karlsruhe, Germany. The goal of the experiment is to measure the absolute mass scale of the neutrino with a sensitivity of $m(\nu_e) = 0.2$ eV (90% C.L.), an order of magnitude lower than the current established limit. Achieving this goal requires improvements over previous direct measurement experiments in both the tritium-decay β luminosity and the resolution of the spectrometers [27]. Since the focus of this thesis concerns the electrostatic and magnetostatic aspects of the KATRIN experiment, the following sections serve as a general description of the components of the experiment with respect to these topics.

2.2 Tritium Source and β Transport System

The tritium-decay β beam for the KATRIN experiment is provided by the windowless gaseous tritium source (WGTS) (see Fig. 2-1). Ultra-cold (27 K) gaseous tritium is injected into the middle of the 10 m long, 90 mm diameter WGTS tube, and pumped out at the ends of the tube, creating a tritium column density $\rho d = 5 \cdot 10^{17}$ molecules/cm². The tritium emits a β -decay luminosity of $9.5 \cdot 10^{10}$ β /second isotropically. These electrons are guided adiabatically to either end of the WGTS tube

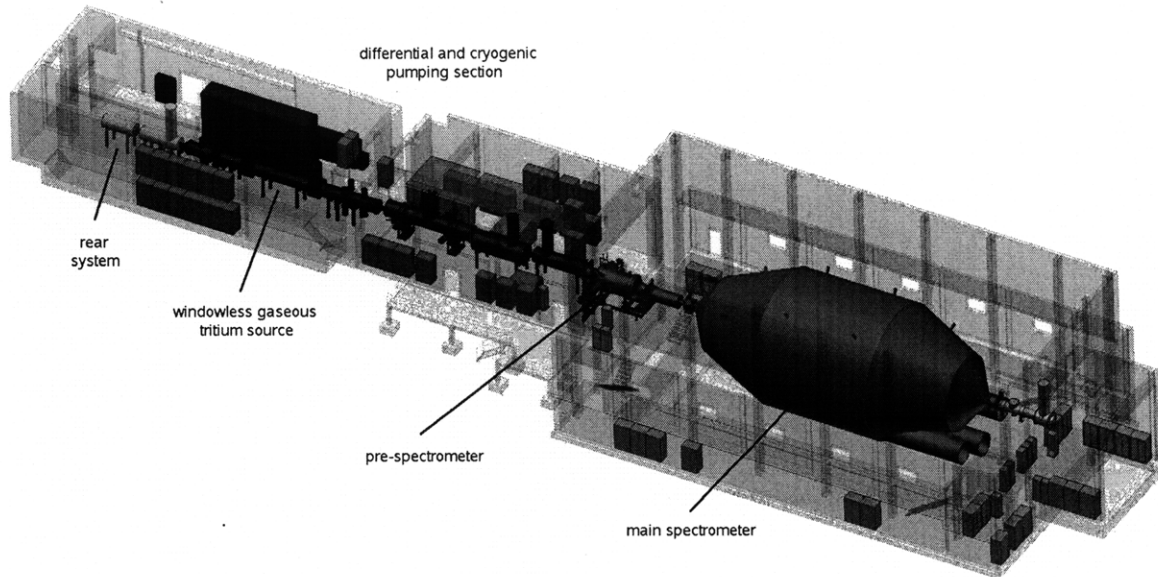


Figure 2-1: A schematic of the KATRIN beamline, including the windowless gaseous tritium source (WGTS), the rear system and the β transport system.

by a 3.6 T magnetic field.¹ The collimated electrons then enter the transport system, where they are transported adiabatically to the spectrometers via 21 solenoids that produce a magnetic field along the axis of the transport system of 5.6 T. In order to restrict tritium flow into the spectrometers, the transport system contains 20° tilts in the magnetic flux tube, preventing line-of-sight between the WGTS and the spectrometers [28]. The parameters of the magnets in the WGTS and β transport system are described in Table 2.1.

2.3 Pre- and Main Spectrometers

2.3.1 Properties of a MAC-E-Filter

A MAC-E-Filter (an acronym for Magnetic Adiabatic Collimation followed by an Electrostatic Filter) is an integrating spectrometer designed to maximize the luminosity and kinetic energy resolution of a beam of charged particles [29]. It exploits the

¹The strength of the magnetic field in the WGTS is chosen to be 60% of the largest magnetic field in the KATRIN experiment, in order to produce a magnetic mirror that rejects electrons with a high pitch angle. Electrons with a high pitch angle are unfavorable since they are more likely to multiply scatter before leaving the WGTS.

Magnet #	J (A/mm ²)	R _i (mm)	R _o (mm)	Z ₁ (mm)	Z ₂ (mm)
1	150.45	111.62	148.33	-4026.99	-4853.49
2	150.45	116.5	135.53	-4829.57	-1765.33
3	150.45	115	143.55	-1743.52	-1668.48
4	150.45	115	143.55	-1628.97	-1553.93
5	150.45	116.5	135.53	-1532.12	1532.12
6	150.45	115	143.55	1553.93	1628.97
7	150.45	115	143.55	1668.48	1743.52
8	150.45	116.5	135.53	1765.33	4829.57
9	150.45	111.62	148.33	4853.49	4926.99
10	152.2	115	144.91	-5455.15	-5357.14
11	152.2	114	133.03	-6248.69	-5466.17
12	152.2	113.5	143.41	-6357.71	-6259.70
13	152.2	118	147.91	-6885.87	-6787.86
14	152.2	114	133.03	-7679.41	-6896.89
15	152.2	122	150.55	-7788.43	-7690.43
16	100.63	209.50	115	6787.86	6885.87
17	100.63	209.50	119	6896.89	7679.41
18	100.63	209.50	122	7690.43	7788.43
19	100.63	209.50	120	5357.14	5455.15
20	100.63	209.50	119	5466.17	6248.69
21	100.63	209.50	115	6259.70	6357.71

Table 2.1: Magnet specifications for the WGTS and β -transport system.

adiabatic invariance of the magnetic moment of the particle's cyclotron orbit (defined as the ratio of the particle's transverse² kinetic energy to the strength of the magnetic field, $|\mu| = T_{\perp}/|B|$) for non-relativistic charged particles in a magnetostatic field [30].

The general design of a MAC-E-Filter is depicted in Figure 2-2: the entrance and exit of the spectrometer are constrained by strong magnetic fields (B_{max}) (located at x_0 and x_2 in Fig. 2-2), and the field reaches a minimum (B_{min}) at the spectrometer's center (at x_1). The magnets at the entrance and exit of the spectrometer are designed to cover the same flux tube, so that particles entering the spectrometer are confined to helical trajectories about the resulting magnetic field lines. This results in an initial transmission of $\approx 50\%$, since all charged particles with forward momentum will follow a magnetic field line into the spectrometer. In addition, a retarding electric field parallel to the magnetic field is formed by electrodes surrounding the flux tube,

²For this discussion, the *transverse* and *longitudinal* directions refer to directions perpendicular and parallel to the beam line, respectively.

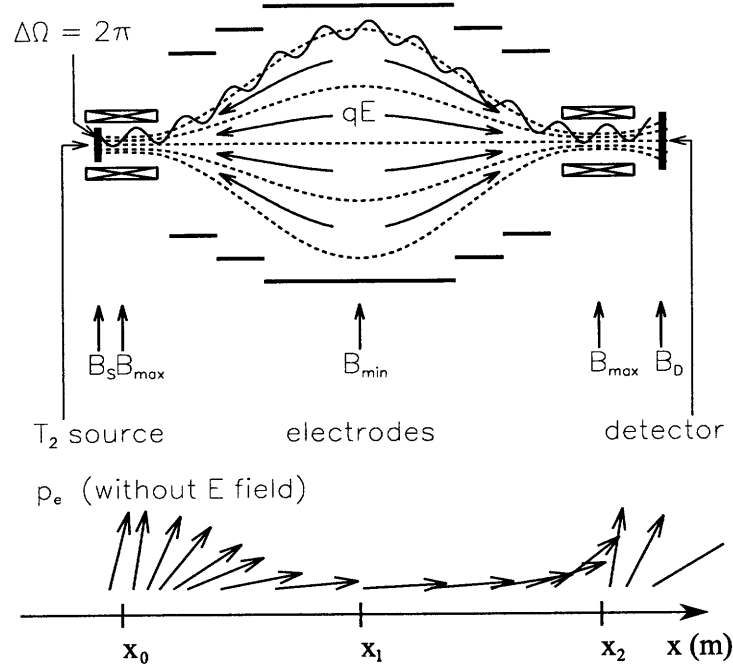


Figure 2-2: General setup of a MAC-E-Filter. (Top) experimental configuration and (bottom) the adiabatic momentum transformation of charged particle through the filter.

with maximum potential U_0 at x_1 .

By conservation of energy, we can equate the energy of a particle at positions x_0 and x_1 as follows:

$$T_0 = T_1 + qU_0, \quad (2.1)$$

where T_i represents the kinetic energy of a particle at x_i , and q is the particle's charge.

Since $T = T^{\parallel} + T^{\perp}$, Equation 2.1 can be rewritten as

$$T_1^{\parallel} + T_1^{\perp} = T_0 - qU_0. \quad (2.2)$$

In order for the particle to pass through the filter, T_1^{\parallel} must be greater than zero. Combining this with Equation 2.2, we get the following condition for particles that pass through the spectrometer:

$$T_0 - T_1^{\perp} - qU_0 > 0. \quad (2.3)$$

Due to the adiabatic invariance of $|\mu|$, the following relation holds between a particle's transverse kinetic energy and the magnetic field strength at x_0 and x_1 :

$$\frac{T_0^\perp}{|B_{max}|} = |\mu| = \frac{T_1^\perp}{|B_{min}|} \Rightarrow \frac{T_1^\perp}{T_0^\perp} = \frac{B_{min}}{B_{max}}. \quad (2.4)$$

From Equation 2.4 and the condition that $0 \leq T_0^\perp \leq T_0$, we obtain the following limits on the distribution T_1^\perp :

$$0 \leq T_1^\perp \leq \frac{B_{min}}{B_{max}} T_0. \quad (2.5)$$

Combining Equations 2.3 and 2.5, we can determine the energy interval ΔU over which the transmission of particles through the spectrometer rises from 0 to 1 to be

$$q U_0 \leq T_0 \leq q U_0 \left(1 + \frac{B_{min}}{B_{max}} \right), \quad (2.6)$$

corresponding to a resolving power of

$$\frac{T_0}{\Delta T} = \frac{U_0}{\Delta U} = \frac{B_{max}}{B_{min}}. \quad (2.7)$$

In order to derive an explicit form for the transmission function $f(T_0, U_0)$ within the region defined in 2.6 (derived from [31]), we must integrate over the pitch angle of the particles for a given initial energy T_0 that pass through the filter:

$$f(T_0, U_0) = \int_0^{\frac{\pi}{2}} n(\theta) \cdot \Theta(T_1^\parallel) \cdot d\theta, \quad (2.8)$$

where $n(\theta) \cdot d\theta$ represents the differential solid angle, and $\Theta(T_1^\parallel)$ is the Heaviside step function that returns 1 for all $T_1^\parallel > 0$. The differential solid angle is easily solved to be

$$n(\theta) \cdot d\theta = \sin \theta \cdot d\theta \quad (2.9)$$

and, from Equations 2.2 and 2.4, we can modify T_1^{\parallel} in 2.8 to be

$$T_1^{\parallel} = T_0 - q U_0 - \left(\frac{B_{min}}{B_{max}} \right) T_0 \sin^2 \theta. \quad (2.10)$$

Using these values in Equation 2.8, we get

$$f(T_0, U_0) = \int_0^{\frac{\pi}{2}} \sin \theta \cdot \Theta \left(T_0 - q U_0 - \left(\frac{B_{min}}{B_{max}} \right) T_0 \sin^2 \theta \right) \cdot d\theta. \quad (2.11)$$

We can substitute for the Heaviside function in Equation 2.11 a modified region of integration as follows:

$$f(T_0, U_0) = \int_0^{\theta'} \sin \theta \cdot d\theta, \quad (2.12)$$

with

$$\sin^2 \theta' = \frac{T_0 - q U_0}{T_0} \cdot \frac{B_{max}}{B_{min}}. \quad (2.13)$$

Computing this integral is now a straightforward process:

$$\begin{aligned} f(T_0, U_0) &= \int_0^{\theta'} \sin \theta \cdot d\theta \\ &= 1 - \cos \theta' = 1 - \sqrt{1 - \sin^2 \theta'} \\ &= 1 - \sqrt{1 - \frac{T_0 - q U_0}{T_0} \cdot \frac{B_{max}}{B_{min}}} \end{aligned} \quad (2.14)$$

With Equations 2.6 and 2.14 (normalized to unity), we obtain the following full equation for the transmission function of a MAC-E filter:

$$f(T_0, U_0) = \begin{cases} 0 & T_0 \leq q U_0 \\ \frac{1 - \sqrt{1 - \frac{T_0 - q U_0}{T_0} \cdot \frac{B_{max}}{B_{min}}}}{1 - \sqrt{1 - \frac{1}{1 + \frac{B_{min}}{B_{max}}}}} & q U_0 < T_0 < q U_0 \left(1 + \frac{B_{min}}{B_{max}} \right) \\ 1 & T_0 \geq q U_0 \left(1 + \frac{B_{min}}{B_{max}} \right) \end{cases}, \quad (2.15)$$

displayed graphically in Figure 2-3. The result is an integrating mass spectrometer with a high transmission ($\approx 50\%$) and a scalable resolution dependent upon the strengths of the magnetic fields [29].

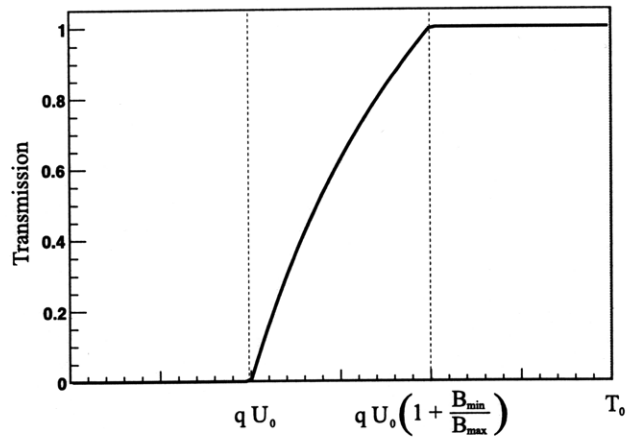


Figure 2-3: Graphical description of the transmission function of a MAC-E filter.

2.3.2 KATRIN MAC-E Filters

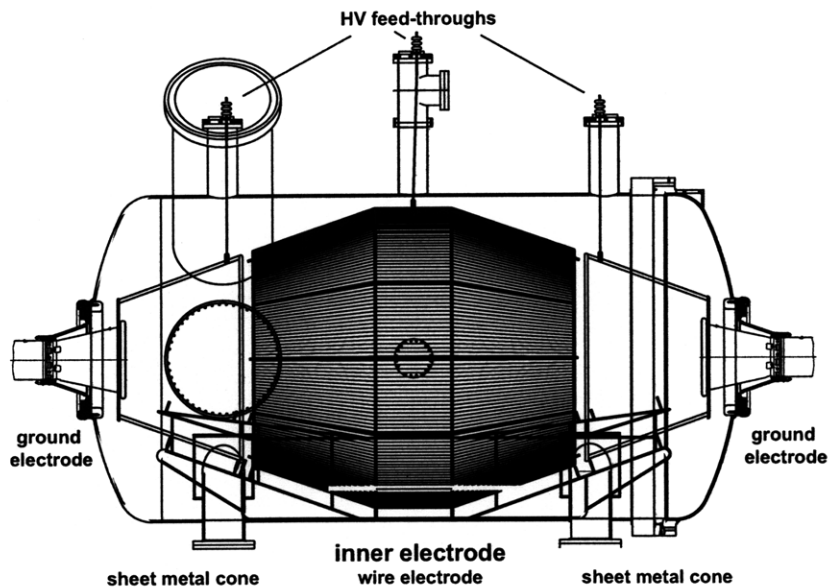


Figure 2-4: Schematic of the inner wire electrodes in the pre-spectrometer. Similar wire electrodes are present in the main spectrometer.

Immediately downstream from the transport system described in Section 2.2 are two MAC-E filters placed in sequence. The filters employ a novel electrode design system, where the retarding high voltage is connected to the hulls of the spectrometers themselves. Immediately inside the hulls are wire electrodes held at slightly lower

potential, designed to reject background particles and to fine-tune the electric fields within the spectrometers (see Fig. 2-4) [28]. Wires are used to minimize the surface area of the electrode, reducing the probability of background particles due to cosmic ray scattering.

Pre-spectrometer

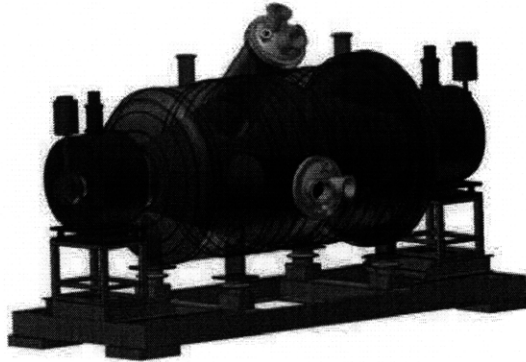


Figure 2-5: Schematic of the pre-spectrometer.

The first filter, known as the pre-spectrometer, acts as a pre-filter to the β stream by rejecting electrons with energy < 18.3 keV (see Fig. 2-5). Since its primary function during operation is to decrease the flux of incoming electrons, it has relatively small dimensions (3.38 m long, 1.70 m diameter) and a modest energy resolution $\Delta U \approx 100$ eV. The magnets at the ends of the pre-spectrometer create a 4.5 T magnetic field, with a minimum field of 0.02 T in the analyzing plane.

Main spectrometer

The main spectrometer is essentially a scaled-up version of the pre-spectrometer. The electrodes comprising the hull of the spectrometer create a potential difference between the entrance and the analyzing plane $U_0 \approx -18.55$ keV. The spectrometer has a magnetic field strength $B_{min} \approx 3 \times 10^{-4}$ T at the analyzing plane (see Fig. 2-6). In addition to the magnets at the entrance and exit, axially symmetric air coils around the circumference of the detector allow for finer control of the magnetic flux

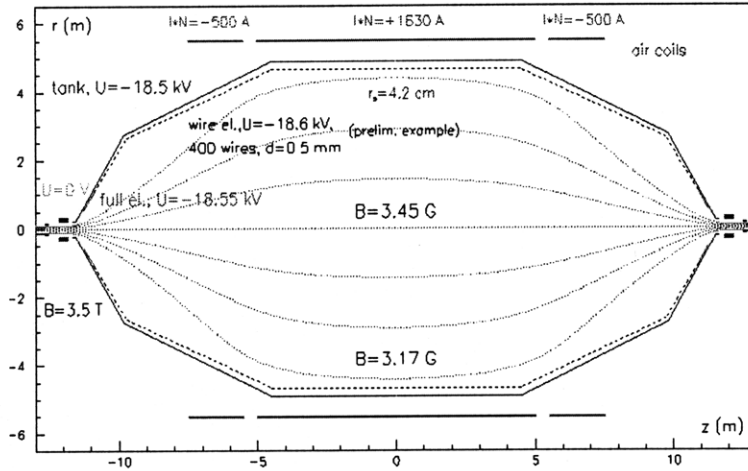


Figure 2-6: Schematic of the electromagnetic configuration of the main spectrometer.

tube and provide compensation for the earth's magnetic field. The relative differences of the magnetic field strengths at the entrance and the analyzing plane necessitate the large dimensions of the spectrometer, which are about 10 m in diameter and 22.3 m in length. By allowing the magnetic field lines within the spectrometer to diverge to such a large flux tube diameter, the main spectrometer is able to attain energy resolutions $\Delta U \approx 1$ eV, a factor of 5 better than the leading MAC-E filters do date [28].

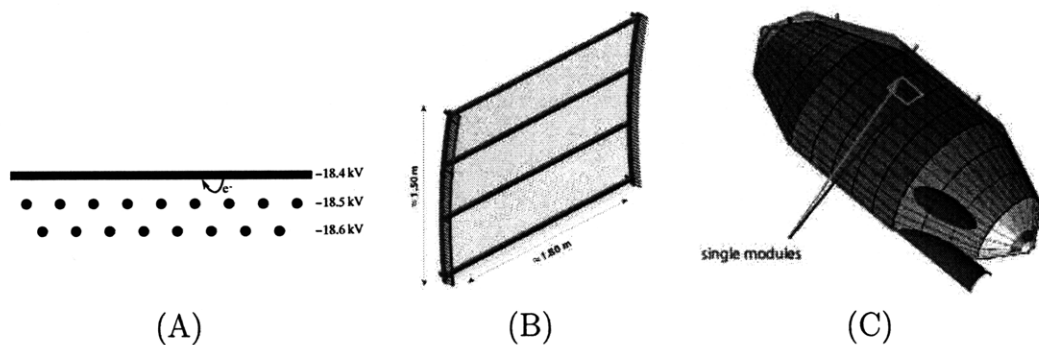


Table 2.2: (A) Wires placed inside the main spectrometer, in order to deflect incident negatively charged particles. (B) A module holding wire electrodes. (C) Wire module placement in the main spectrometer. Images taken from [32].

To decrease background particles due to cosmic rays and radioactive isotopes within the electrodes, the interior of the main spectrometer is lined with ≈ 1300 modules of wire electrodes held at a slightly negative potential with respect to the

spectrometer hull (see Table 2.2). The wires provide a screening factor S ,

$$S = \frac{U_{wire} - U_{vessel}}{U_{wire} - U_{inner}} \approx 1 + \frac{2\pi(l/s)}{\ln(s/(\pi d))}, \quad (2.16)$$

where l represents the wire length, s is the distance between the wires, and d denotes the diameter of each wire. A large S -value corresponds to more effective screening of background particles. The wire modules an outer and inner layer of wire electrodes with diameters of 3 and 2 mm, respectively.

2.4 Detector

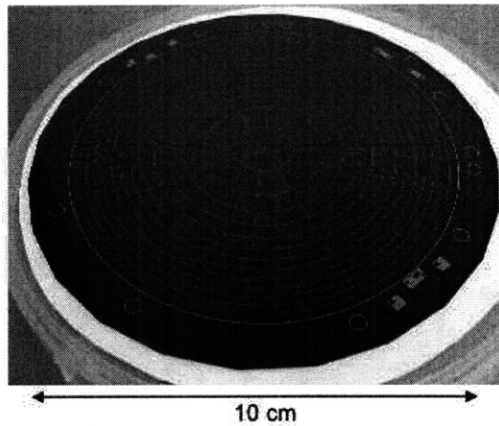


Figure 2-7: Image of the segmented detector.

The tritium-decay β -electrons that pass through the main spectrometer then enter the detector region. The detector region of the KATRIN experiment consists of a multi-pixel silicon semiconductor detector, with energy resolution $\Delta E < 600\text{eV}$, within a 5.6 T magnetic field. The size of the detector is closely linked to the ratio of the magnetic field strengths at the the entrance to the detector region (B_{max}) and at the detector itself (B_{det}). The maximum angle $\theta_{det,max}$ that electrons incident on the detector may have is determined by

$$\theta_{det,max} \approx \arcsin\left(\frac{B_{det}}{B_{max}}\right). \quad (2.17)$$

The current configuration of the detector region is designed so that $\theta_{det,max} \approx 45^\circ$, corresponding to a detector with diameter $d_{det} \approx 9$ cm to encompass the magnetic flux tube. The detector is segmented into 148 divisions in order to provide spacial resolution, allowing for localization of each incident particle's track coordinates (see Fig. 2-7).

Electrons incident on the detector are post-accelerated by up to 30 keV by a conical electrode. This post-acceleration electrode helps to decrease background by translating the signal above low-energy noise intrinsic to the detector and by reducing backscattering off of the detector. Background signal is further suppressed by a veto shield encompassing the detector region, able to reject events coincident with cosmic ray background.

2.5 The role of simulation in electrode and magnet design

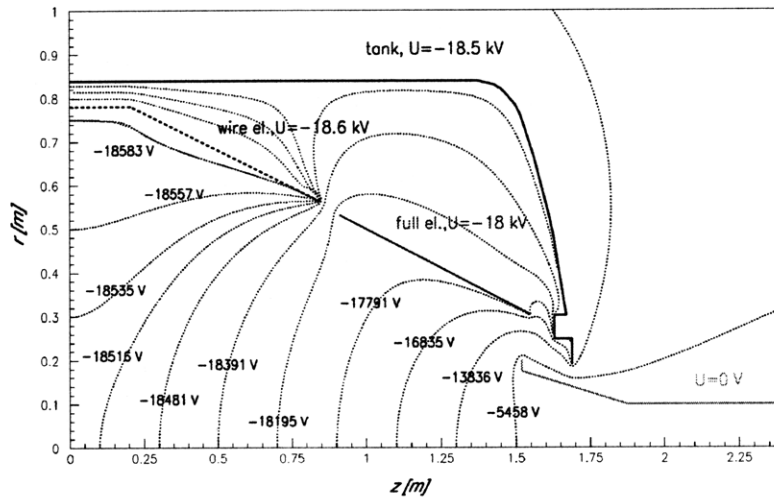


Figure 2-8: Equipotential lines at the exit of the pre-spectrometer. Image taken from [28].

It is evident from the previous sections that deviations from the electrostatic and magnetostatic fields from the design values can contribute significantly to the systematic design of the KATRIN experiment. Understanding the systematic errors

and optimizing the fields associated with the electrodes and magnets is a nontrivial endeavor. For example, one of the leading concerns within the collaboration with respect to the electrode and magnet design is that an effect called a Penning Trap may arise. Penning Traps are potential wells along the magnetic field lines. The task of eliminating Penning traps is best suited to simulations of the electrostatic and magnetostatic fields, since the fields can quickly become rather complex for even a simple electrode and magnet configuration (see Fig. 2-8), and since it is difficult to experimentally locate Penning traps.

Additionally, it is important to understand the systematic errors that occur due to electrode and magnet misalignment. Since the placement of field-inducing elements inherently must have tolerances, and since the electrostatic and magnetostatic fields are extremely sensitive to the placement of these elements, tests must be conducted in order to understand how the errors intrinsic to misalignment propagate through the fields to errors in a measurement of the signal. Once again, the only practical method of performing these tests is through simulation.

Chapter 3

Direct Calculation of Electric and Magnetic Fields

3.1 Introduction

Three techniques used to calculate electromagnetic fields are described in this thesis. The first of these techniques is the direct calculation method; so named because it makes the least number of approximations in its application of the fundamental laws of electromagnetism. The method calculates the electric potential (and, subsequently, the electric field) directly from charge distributions, and the magnetic vector potential and magnetic field from current distributions. While basic in theory, the techniques employed are mathematically nontrivial, and it is therefore necessary to describe them with a fair amount of rigor.

The first section describes a method used in engineering practices known as the Boundary Element Method (BEM). It is relevant to the material in this chapter because, in application to electrostatics, it provides a means of determining the charge distribution from a general configuration of electrodes held at various potentials. Since in the KATRIN experiment only the electric potential of the electrodes are known, application of the BEM is an essential step to performing direct calculations of electric fields.¹

¹In fact, the charge distribution obtained by employing the BEM is critical to all of the electric

The next section develops the mathematical tools necessary for the computation of the electric potential due to electrodes of various shapes with constant charge densities. Care is taken to provide an unambiguous description of the parameters of each electrode primitive, so that the parameters used in the formula associated with it match the input parameters used in the program `KatrinField`. The primitives described are so chosen for their ability to reproduce a discretized description of the electrodes used in the KATRIN experiment, while still being tractable for practical computation.

The final section describes the requisite formulae for reproducing the magnetic fields from the magnets used in the KATRIN experiment. Once again, parameters are described to replicate the input parameters used in `KatrinField`.

3.2 Boundary Element Method

3.2.1 General description of the Boundary Element Method

The BEM is a computational technique for solving linear partial differential equations. Compared to other popular methods (such as the Finite Element and Finite Difference Methods [33]) designed to accomplish the same goal, the BEM differs in many respects, favoring its use in an important subset of problems. Instead of discretizing the entire region of interest, the main technique of the BEM is to discretize only the surfaces of the geometries in the region. This effectively reduces the dimensionality of the problem and facilitates the calculation of fields for regions that extend out to infinity (rather than restricting computation to a finite region).[34] These two features make the BEM faster and more versatile than competing methods when it is applicable.

It should be noted that, while our interest in the BEM is limited to the field of electrostatics, the method itself is a general technique whose application is rather diverse. As a result, the following derivations (a composite of the techniques described

field-solving techniques described in this thesis.

in [35], [34], [36], [37], [38] and [39]) will be performed in an abstract setting and, once the necessary results are obtained, we will relate the method back to the determination of charge distributions from potential distributions.

3.2.2 Definitions

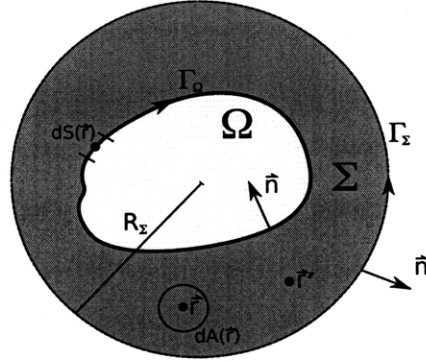


Figure 3-1: A graphical depiction of the regions Ω (in white) and Σ (in grey). \vec{n} describes the unit normal vector to the boundaries (Γ_Ω and Γ_Σ) of these regions, and \vec{r}' is the observation point.

We begin by defining a two-dimensional region Ω , bounded by a piecewise smooth contour Γ_Ω with clockwise orientation. Next, we bound the region Ω with a circularly shaped two-dimensional encompassing region Σ , bounded externally by a circular, counterclockwise oriented contour Γ_Σ of radius R_Σ and internally by the contour Γ_Ω (see Fig. 3-1). We will frequently refer to fixed points in space, known hereafter as *observation points*, with the label \vec{r}' . Furthermore, we define $dS(\vec{r}')$, $\vec{r}' \in (\Gamma_\Omega \cup \Gamma_\Sigma)$, as an infinitesimal line segment centered at \vec{r}' and tangent to the boundary on which it is located. Finally, we define $dA(\vec{r}')$, $\vec{r}' \in \Sigma$, as an infinitesimal area centered about \vec{r}' .

3.2.3 Derivation from Green's second identity

We are looking for solutions to the Laplace equation for regions of Φ where no charge is enclosed,

$$\nabla^2 \Phi = 0, \quad (3.1)$$

in the region Σ . We begin by applying Green's second identity to Σ , as follows:

$$\int_{\Sigma} (U\nabla^2 W + W\nabla^2 U) dA(\vec{r}) = \int_{\Gamma_{\Sigma} + \Gamma_{\Omega}} \left(U \frac{\partial W}{\partial n} - W \frac{\partial U}{\partial n} \right) dS(\vec{r}), \quad (3.2)$$

where $U(\vec{r})$ and $W(\vec{r})$ are twice continuously differentiable scalar functions in Σ and on its boundaries. We now take $U(\vec{r})$ to be the solution to Equation 3.1. Applying this to Equation 3.2 eliminates one of the terms on the left-hand side, leaving us with

$$\int_{\Sigma} U\nabla^2 W dA(\vec{r}) = \int_{\Gamma_{\Sigma} + \Gamma_{\Omega}} \left(U \frac{\partial W}{\partial n} - W \frac{\partial U}{\partial n} \right) dS(\vec{r}). \quad (3.3)$$

Next, we choose a suitable $W(\vec{r})$ to eliminate the remaining domain integral on the left-hand side of Equation 3.3, so that only calculations around the boundary of Ω remain. This is done by letting $W(\vec{r})$ be the fundamental solution of the Laplace equation, with the property that

$$\nabla^2 W(\vec{r}) = -\delta(\boldsymbol{z}), \quad (3.4)$$

where $\boldsymbol{z} = |\vec{r} - \vec{r}'|$.

In two dimensions², the fundamental solution to the Laplace equation is defined as

$$W(\vec{r}) = -\frac{1}{2\pi} \ln(\boldsymbol{z}). \quad (3.5)$$

Immediately, it can be seen that this choice of $W(\vec{r})$ causes singularities to arise in Equation 3.3 when $\vec{r} = \vec{r}'$ in Σ (where $\ln(\boldsymbol{z})$ is undefined) and when $\vec{r}' \in (\Gamma_{\Omega} \cup \Gamma_{\Sigma})$ (where $\delta(\boldsymbol{z})$ is undefined). It is necessary to handle these singularities before any further progress can be made.

3.2.4 Singularities

We begin by dealing with the singularity that occurs when $\vec{r} = \vec{r}'$, and $\vec{r}' \in \Sigma$. By excluding from Σ a small circular region Σ_{ϵ} with boundary Γ_{ϵ} , characterized by a

²The three-dimensional fundamental solution to the laplace equation is $W(\vec{r}) = \frac{1}{4\pi\boldsymbol{z}}$.

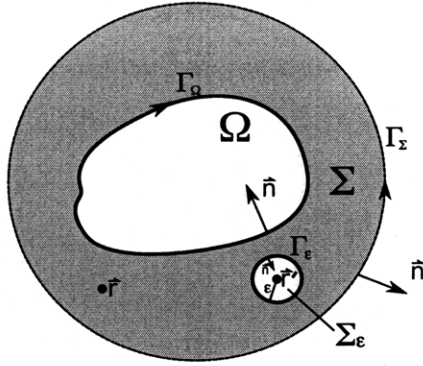


Figure 3-2: By including a small Γ_ϵ , we are able to avoid the divergence of $W(\vec{r})$. Taking the limit as $\epsilon \rightarrow 0$, we recover our original domain.

radius ϵ centered at our observation point \vec{r}' (see Fig. 3-2), we modify Equation 3.3 to be

$$\int_{\Sigma - \Sigma_\epsilon} U \nabla^2 W dA(\vec{r}) = \int_{\Gamma_\Sigma + \Gamma_\Omega - \Gamma_\epsilon} \left(U \frac{\partial W}{\partial n} - W \frac{\partial U}{\partial n} \right) dS(\vec{r}). \quad (3.6)$$

The left-hand side of this equation is zero (since $\nabla^2 W(\vec{r}) = 0 \forall \vec{r} \in (\Sigma - \Sigma_\epsilon)$), and we are left with additional terms on the right-hand side. Making the following changes in variables:

$$\begin{aligned} |\vec{r} - \vec{r}'| &= \epsilon, \\ \frac{\partial}{\partial n} &= -\frac{\partial}{\partial \epsilon}, \\ dS(\vec{r}) &= \epsilon \cdot d\theta, \end{aligned} \quad (3.7)$$

we evaluate the first additional term on the right-hand side to be

$$\begin{aligned} - \int_{\Gamma_\epsilon} U(\vec{r}) \frac{\partial}{\partial n} W(\vec{r}) \cdot dS(\vec{r}) &= \frac{1}{2\pi} \int_0^{2\pi} U(\vec{r}) \left(-\frac{1}{\epsilon} \right) \epsilon \cdot d\theta = \\ &= -\frac{1}{2\pi} \int_0^{2\pi} U(\vec{r}) \cdot d\theta, \end{aligned} \quad (3.8)$$

which, as $\epsilon \rightarrow 0$, approaches $-U(\vec{r}')$. The second additional term on the right-hand side of Equation 3.6 becomes

$$\begin{aligned} - \int_{\Gamma_\epsilon} \frac{\partial}{\partial n} U(\vec{r}) \cdot W(\vec{r}) \cdot dS(\vec{r}) &= \frac{1}{2\pi} \int_0^{2\pi} \frac{\partial U(\vec{r})}{\partial n} \ln(\epsilon) \epsilon \cdot d\theta = \\ &= \frac{\epsilon \ln(\epsilon)}{2\pi} \int_0^{2\pi} \frac{\partial U(\vec{r})}{\partial n} \cdot d\theta, \end{aligned} \quad (3.9)$$

which approaches 0 as $\epsilon \rightarrow 0$. Therefore, when $\vec{r} = \vec{r}'$, $\vec{r}' \in \Sigma$, Equation 3.3 becomes

$$U(\vec{r}') = \int_{\Gamma_\Sigma + \Gamma_\Omega} \left(U \frac{\partial W}{\partial n} - W \frac{\partial U}{\partial n} \right) dS(\vec{r}). \quad (3.10)$$

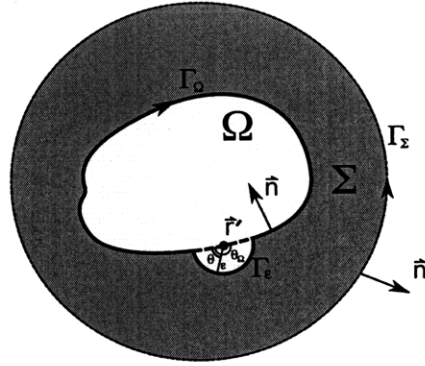


Figure 3-3: By deforming Γ_Ω to include a small circular segment of radius ϵ , we are able to avoid the singularity of $\nabla^2 W(\vec{r})$ at the boundary. Taking the limit as $\epsilon \rightarrow 0$, we recover our original boundary.

Next, we deal with the singularity that occurs on the boundaries of Ω . To avoid the ambiguity of the delta function at Γ_Ω , the boundary is deformed to incorporate the arc of a circle with radius ϵ , and the limit is taken as ϵ approaches zero (see Fig. 3-3). By including the boundary Γ_ϵ (formed by the circular arc of radius ϵ subtending an angle θ_Ω) in Equation 3.10, we get

$$U(\vec{r}') = \int_{\Gamma_\Sigma + \Gamma_\epsilon + \Gamma_\Omega} \left(U \frac{\partial W}{\partial n} - W \frac{\partial U}{\partial n} \right) dS(\vec{r}). \quad (3.11)$$

Evaluating the extra terms on the right-hand side of Equation 3.11 in a similar manner as before (with a change in sign, since the boundary normal is reversed), we get for

the first additional term

$$\begin{aligned} \int_{\Gamma_\epsilon} U(\vec{r}) \frac{\partial W}{\partial n} dS(\vec{r}) &= -\frac{1}{2\pi} \int_0^{\theta_\Omega} U(\vec{r}) \left(\frac{1}{\epsilon}\right) \epsilon \cdot d\theta = \\ &= \frac{1}{2\pi} \int_0^{\theta_\Omega} U(\vec{r}) \cdot d\theta, \end{aligned} \quad (3.12)$$

which approaches $\frac{\theta_\Omega}{2\pi} \cdot U(\vec{r}')$ as $\epsilon \rightarrow 0$. The second additional term becomes

$$\begin{aligned} \int_{\Gamma_\epsilon} \frac{\partial}{\partial n} U(\vec{r}) \cdot W(\vec{r}) \cdot dS(\vec{r}) &= -\frac{1}{2\pi} \int_0^{\theta_\Omega} \frac{\partial U(\vec{r})}{\partial n} \ln(\epsilon) \epsilon \cdot d\theta = \\ &= -\frac{\epsilon \ln(\epsilon)}{2\pi} \int_0^{\theta_\Omega} \frac{\partial U(\vec{r})}{\partial n} \cdot d\theta, \end{aligned} \quad (3.13)$$

which approaches zero as $\epsilon \rightarrow 0$. It is now possible to rewrite Equation 3.10 to include the boundaries Γ_Σ and Γ_Ω (since this approach works for deforming Γ_Σ as well) as

$$c(\vec{r}') \cdot U(\vec{r}') = \int_{\Gamma_\Omega + \Gamma_\Sigma} \left(U \frac{\partial W}{\partial n} - W \frac{\partial U}{\partial n} \right) dS(\vec{r}), \quad (3.14)$$

where

$$c(\vec{r}') = \begin{cases} 1 & \vec{r}' \in \Sigma \\ 1 - \frac{\theta_\Omega}{2\pi} & \vec{r}' \in (\Gamma_\Omega \cup \Gamma_\Sigma) \\ 0 & \vec{r}' \notin \Sigma \end{cases} . \quad (3.15)$$

3.2.5 Extending R_Σ to ∞

By enforcing the condition that, for large $|\vec{r}'|$, $U(\vec{r}') \sim O(\frac{1}{R_\Sigma})$, we can make the following substitutions to observe the behavior of Equation 3.14 as $R_\Sigma \rightarrow \infty$:

$$\begin{aligned} |\vec{r} - \vec{r}'| &\sim R_\Sigma, \\ \frac{\partial}{\partial n} &= \frac{\partial}{\partial R_\Sigma}, \\ dS(\vec{r}) &= R_\Sigma \cdot d\theta. \end{aligned}$$

The first term involving Γ_Σ in Equation 3.14 now becomes

$$\int_{\Gamma_\Sigma} U(\vec{r}) \frac{\partial W(\vec{r})}{\partial n} dS(\vec{r}) \sim -\frac{1}{2\pi} \int_0^{2\pi} \left(\frac{1}{R_\Sigma} \right) \frac{\partial \ln(R_\Sigma)}{\partial R_\Sigma} \cdot R_\Sigma d\theta = \quad (3.16)$$

$$= -\frac{1}{2\pi} \int_0^{2\pi} \left(\frac{1}{R_\Sigma} \right) d\theta = \quad (3.17)$$

$$= \frac{1}{R_\Sigma}, \quad (3.18)$$

which approaches zero as $R_\Sigma \rightarrow \infty$. The second term in Equation 3.14 becomes

$$\int_{\Gamma_\Sigma} \frac{\partial U(\vec{r})}{\partial n} W(\vec{r}) dS(\vec{r}) \sim -\frac{1}{2\pi} \int_0^{2\pi} \left(-\frac{1}{R_\Sigma^2} \right) \ln(R_\Sigma) R_\Sigma d\theta = \quad (3.19)$$

$$= \frac{\ln(R_\Sigma)}{R_\Sigma}, \quad (3.20)$$

which also approaches zero as $R_\Sigma \rightarrow \infty$. We have now arrived at underlying equation for the Boundary Element Method in its final form:

$$c(\vec{r}') \cdot U(\vec{r}') = \int_{\Gamma_\Omega} \left(U \frac{\partial W}{\partial n} - W \frac{\partial U}{\partial n} \right) dS(\vec{r}), \quad (3.21)$$

$$c(\vec{r}') = \begin{cases} 1 & \vec{r}' \in \Sigma \\ 1 - \frac{\theta_\Omega}{2\pi} & \vec{r}' \in \Gamma_\Omega \\ 0 & \vec{r}' \notin \Sigma \end{cases} . \quad (3.22)$$

3.2.6 Connection to indirect BEM

We now have a formula relating a function that satisfies the Laplace equation in our region of interest to the properties of the function at the region's boundaries. With this, the standard application of the BEM is to discretize the boundary, thus converting Equation 3.21 into a soluble linear algebraic equation. There is another approach, however, whose derivation stems from this point in the derivation of the direct BEM, that proves to be better suited to our needs. The purpose of the indirect BEM (known by many other names, including Source Element Method (SEM), Source Integration Method (SIM), and Charge-Density (Integral) Method) is to apply Dirichlet bound-

ary conditions³ in order to solve for a source distribution, and then to use the source distribution to solve the function for all space.

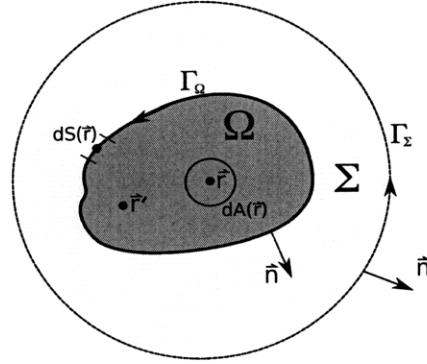


Figure 3-4: The equivalent figure to 3-1 for internal problems. The shaded region denotes the domain of interest for computation.

The preceding derivation for the BEM is specifically tailored to *exterior problems*, where the domain in which we wish to know the function that satisfies the laplace equation lies outside of the boundary. By a very similar approach, one can derive the underlying equation of the BEM for *interior problems* to be

$$c(\vec{r}^j) \cdot \tilde{U}(\vec{r}^j) = \int_{\Gamma_{\Omega}} \left(\tilde{U} \frac{\partial W}{\partial n} - W \frac{\partial \tilde{U}}{\partial n} \right) dS(\vec{r}), \quad (3.23)$$

$$c(\vec{r}^j) = \begin{cases} 1 & \vec{r}^j \in \Omega \\ \frac{\theta_{\Omega}}{2\pi} & \vec{r}^j \in \Gamma_{\Omega} \\ 0 & \vec{r}^j \notin \Omega \end{cases}, \quad (3.24)$$

which differs from Equation 3.21 by the definition of the boundary angle, the boundary's orientation and the direction of the boundary normal.

Since Equation 3.23 is defined with the orientation of Γ_{Ω} and its normal reversed, we modify the equation to be in the same terms as Equation 3.21 so that, for $\vec{r}^j \in \Sigma$,

³Boundary conditions are known as Dirichlet when the values of a function are fixed at the boundary.

Equation 3.23 becomes

$$0 = \int_{\Gamma_\Omega} \left(\tilde{U} \frac{\partial W}{\partial n} + W \frac{\partial \tilde{U}}{\partial n} \right) dS(\vec{r}). \quad (3.25)$$

By specifying that $\tilde{U}(\vec{r})$ gives the same values on Γ_Ω as $U(\vec{r})$ (so that $\tilde{U}(\vec{r}) = U(\vec{r}) \forall \vec{r} \in \Gamma_\Omega$), we are able to add Equations 3.25 and 3.21 for $\vec{r}' \in \Sigma$ to get

$$U(\vec{r}') = \int_{\Gamma_\Omega} W \left(\frac{\partial U}{\partial n} + \frac{\partial \tilde{U}}{\partial n} \right) dS(\vec{r}). \quad (3.26)$$

We can then define $\sigma = \left(\frac{\partial U}{\partial n} + \frac{\partial \tilde{U}}{\partial n} \right)$, where σ is the sum of the fluxes across Γ_Ω , [39] and rewrite Equation 3.26 as

$$U(\vec{r}') = \int_{\Gamma_\Omega} W \cdot \sigma \cdot dS(\vec{r}). \quad (3.27)$$

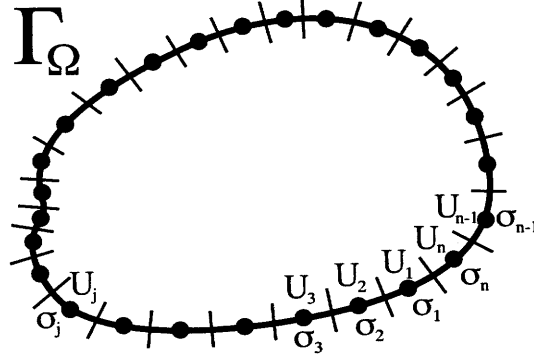


Figure 3-5: Discretization of Γ_Ω into n sub-elements for numerical computation. Charge densities are constant along a sub-element.

In order to compute Equation 3.27 numerically, we approximate Γ_Ω by discretizing it into n line segments, each with a constant value for σ (See Fig. 3-5). In doing so, Equation 3.27 is approximated as

$$U(\vec{r}') = \sum_{j=1}^n \sigma_j \cdot \int_{\Gamma_j} W(\vec{r}_j) \cdot dS(\vec{r}), \quad (3.28)$$

where \vec{r}_j is the position of the j -th sub-element, Γ_j is the j -th discretized segment of Γ_Ω , and σ_j is the sum of the fluxes across Γ_j . If we choose our observation points to be $\vec{r}_i, i = \{1, 2, \dots, n\}$, we can convert Equation 3.28 into a linear algebraic equation in terms of our known functional values and our unknown fluxes at the boundary. Thus, Equation 3.28 becomes

$$U_i = W_{ij} \cdot \sigma_j, \quad (3.29)$$

where $U_i = U(\vec{r}_i)$, $W_{ij} = \int_{\Gamma_j} W(\vec{r}_j) \cdot dS(\vec{r})$ with \vec{r}_i as the observation point, and there is an implicit sum over j . Solving this equation for σ_j , we can obtain values for the boundary fluxes and can then use Equation 3.28 to solve for $U(\vec{r}')$ in all space.

It should be noted that, while the above derivation was completed in the 2-dimensional case, the 3-dimensional derivation is very similar (differing mainly in the definition of the fundamental solution to the Laplace equation, $W(\vec{r})$, and the method of discretization), and provides no new insight into the theory of the technique. The resulting formulae for the 3-dimensional indirect BEM are identical to Equations 3.28 and 3.29, where $W(\vec{r})$ is redefined accordingly for 3-dimensional solutions.

3.2.7 Relation to electrostatics

Applying the results of the derivation of the indirect BEM to electrostatics, we begin by noting that the potential in charge-free regions must satisfy the Laplace equation. It is therefore apparent that our function $U(\vec{r}')$ represents the electric potential at a point \vec{r}' , and that the Dirichlet boundary conditions imply that the potential is known on the surfaces of all of the electrodes. Observing the form of the fundamental solution to the Laplace equation, it also becomes clear that $W(\vec{r})$ is merely the geometric component of the definition of the electric potential due to a point charge.⁴ Finally, σ_i can be seen as the charge density of the i -th sub-element multiplied by $\frac{1}{\epsilon_0}$ by the property of electrostatic boundary conditions that

$$\frac{\partial V_{above}}{\partial n} - \frac{\partial V_{below}}{\partial n} = -\frac{\sigma}{\epsilon_0}, \quad (3.30)$$

⁴This conclusion is more transparent in the 3-dimensional case, where the fundamental solution to the Laplace equation is $W(\vec{r}) = \frac{1}{4\pi\epsilon_0 r}$.

where the difference becomes a sum due to the reversal of the unit normal in Equation 3.25.[40] Given these relations, Equation 3.28 can be interpreted as a reiteration of the law of superposition, where the potential at a given point is the sum of the potential contributions from each of the discretized sub-elements.

By discretizing our boundary, we have effectively made the assumption of a constant charge density on a small, but not infinitesimal, region of our boundary. In order to obtain a charge distribution for any nontrivial electrode configuration, this approximation is unfortunately a necessity. Using decreasingly smaller sub-elements, we approach the actual charge configuration present for a given electrode configuration, at the expense of computational time (the scaling of accuracy to computation time is discussed in Chapter 6).

3.3 Electrostatics

3.3.1 Introduction

The electric fields in the KATRIN experiment are produced using fixed electrodes held at different potentials. This configuration lends itself nicely to analysis via the BEM with Dirichlet boundary conditions. The method of employing the BEM to KATRIN's electrode geometry has been developed by Glück [41][42][43], using discretization methods for both a full 3-dimensional asymmetric geometry and an approximately axially symmetric configuration. The purpose of this section is to introduce the geometry primitives used for discretization and to describe how they are used with the indirect BEM.

3.3.2 Geometry Primitives

Implementation of the BEM requires the discretization of electrode surfaces into sub-elements, or *primitives*, that have a fixed charge density. While a fully 3-dimensional discretization of the electrode surfaces provides for higher accuracy and a more realistic depiction of the geometry, the electrode configuration in KATRIN is well suited

to an axially symmetric approximation. Exploiting this axial symmetry drastically reduces computation time and memory usage, but is only accurate to the degree that the approximation of axial symmetry holds valid (a comparison of the axially symmetric and asymmetric field computation routines can be found in Chapter 6). Therefore, it is necessary to use both axially symmetric and asymmetric discretization methods to maximize computation efficiency, while still maintaining acceptable accuracy in computation of the electric field.

Wire segments, rectangles and right triangles are employed for the asymmetric description of KATRIN's electrode geometry, and rings and conic sections are used for the axially symmetric approximations to this geometry. The original derivation for the electric potential from these electrode primitives (with the exception of the triangle primitive) was originally performed by Glück [42] [43]. In order to implement these shapes for computational analysis via the BEM, a uniform method of description must be provided, as well as a means for determining the electric potential from each primitive held at a constant charge density. We shall examine the five primitives sequentially.

Wire segments

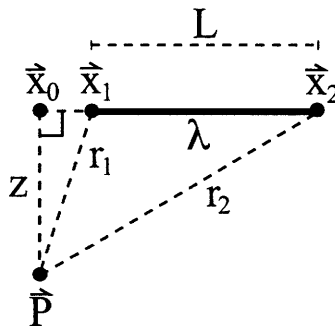


Figure 3-6: A charged line segment with endpoints \vec{x}_1 and \vec{x}_2 and charge density λ , and a field point \vec{P} with minimal distance z from the infinite line on which the line segment is located (the point of intersection is labeled \vec{x}_0). Distances between the field point and x_1 and x_2 are r_1 and r_2 , respectively.

We define a wire segment sub-element by its endpoints \vec{x}_1 and \vec{x}_2 , as well as its diameter d . For the sake of brevity, the following derivation of electric potential from a wire segment is performed under the assumption that d is small compared to the distance between the field point and the wire segment⁵. It is assumed that the wire segment has a constant charge density λ .

We begin by defining the scalars $x_1 = |\vec{x}_1 - \vec{x}_0|$ and $x_2 = |\vec{x}_2 - \vec{x}_0|$. We then introduce an infinitesimal dx along the wire segment, an infinitesimal charge $dQ = \lambda \cdot dx$, and an infinitesimal potential

$$dV = \frac{1}{4\pi\epsilon_0} \cdot \frac{dQ}{r} = \frac{1}{4\pi\epsilon_0} \cdot \frac{\lambda \cdot dx}{\sqrt{x^2 + z^2}}, \quad (3.31)$$

where $x_1 < x < x_2$, and z is defined in Figure 3-6. Integrating from x_1 to x_2 gives

$$V = \frac{\lambda}{4\pi\epsilon_0} \int_{x_1}^{x_2} \frac{dx}{\sqrt{x^2 + z^2}} = \frac{\lambda}{4\pi\epsilon_0} \ln \left(\frac{x_2 + r_2}{x_1 + r_1} \right), \quad (3.32)$$

where $r_1 = |\vec{x}_1 - \vec{P}|$ and $r_2 = |\vec{x}_2 - \vec{P}|$.

While Equation 3.32 is a perfectly viable solution for the electric potential from a charged wire segment, it is possible to simplify the method to facilitate speed of computation by recasting the equation in terms of $L = |\vec{x}_1 - \vec{x}_2| = x_2 - x_1$, the length of the wire segment [44]. With this substitution, Equation 3.32 can be expressed as

$$V = \frac{\lambda}{4\pi\epsilon_0} \ln \left(\frac{r_1 + r_2 + L}{r_1 + r_2 - L} \right), \quad (3.33)$$

which, while algebraically equivalent to Equation 3.32, is only in terms of the parameters r_1 , r_2 and L , which are more readily calculable.

Rectangular sub-elements

We define a rectangular sub-element by the position of one of its corners \vec{P}_0 , the lengths of its sides a and b , and the unit vectors defining the sides of the rectangle \vec{n}_1

⁵In practice, the diameter of the wire segment must be taken into account when computations are performed close to the wire segment.

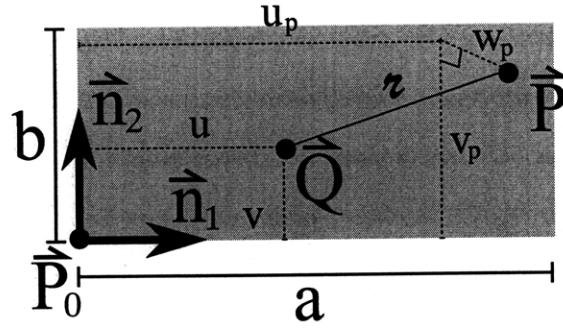


Figure 3-7: A rectangular sub-element defined by the position of a corner \vec{P}_0 , the lengths of the sides a and b , and the unit vectors in the directions of sides a and b , labeled \vec{n}_1 and \vec{n}_2 . The field point is defined as \vec{P} , with local coordinates (u_p, v_p, w_p) . An arbitrary point \vec{Q} located on the surface of the sub-element is shown, with local coordinates $(u, v, 0)$. The distance between \vec{P} and \vec{Q} is z .

and \vec{n}_2 (see Fig. 3-7). Using the local coordinate system defined in Figure 3-7, the electric potential from the rectangle with constant surface charge density σ is

$$V(\vec{P}) = \frac{\sigma}{4\pi\epsilon_0} \int_{-u_p}^{-u_p+a} \int_{-v_p}^{-v_p+b} \frac{1}{z} \cdot dy \cdot dx, \quad (3.34)$$

where $z = \sqrt{(u - u_p)^2 + (v - v_p)^2 + w_p^2} = \sqrt{x^2 + y^2 + w_p^2}$. Using the indefinite integral

$$I_1(x, y, z) = \int \frac{1}{z} \cdot dy = \ln(y + z), \quad (3.35)$$

Equation 3.34 becomes

$$V(\vec{P}) = \frac{\sigma}{4\pi\epsilon_0} \int_{-u_p}^{-u_p+a} (\ln((-v_p + b) + z) - \ln(-v_p + z)) \cdot dx. \quad (3.36)$$

Finally, applying the solution to the indefinite integral

$$I_2(x, y, z) = \int \ln(y + z) \cdot dx = z \arctan\left(\frac{x}{z}\right) - z \arctan\left(\frac{xy}{z^2}\right) - x + y \ln(x + z) + x \ln(y + z), \quad (3.37)$$

we arrive at an analytic solution to Equation 3.36:

$$V(\vec{P}) = \left(\frac{\sigma}{4\pi\epsilon_0} \right) \left(I_2((-u_p + a), (-v_p + b), w_p) - I_2(-u_p, (-v_p + b), w_p) - I_2((-u_p + a), -v_p, w_p) + I_2(-u_p, -v_p, w_p) \right), \quad (3.38)$$

which is the final form of the electric potential from a charged rectangular sub-element.

Right triangular sub-elements

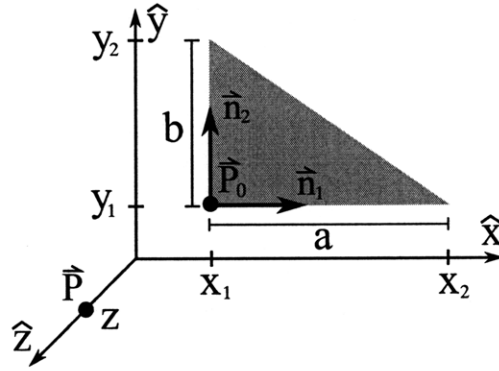


Figure 3-8: A right triangular sub-element defined by the position of the corner opposite the hypotenuse \vec{P}_0 , the lengths of the sides a and b , and the unit vectors in the directions of sides a and b , labeled \vec{n}_1 and \vec{n}_2 . The field point is defined as \vec{P} , with local coordinates $(0, 0, z)$. The corners of the triangle are recast into local coordinates to facilitate integration.

Right triangular sub-elements are described in a similar manner to rectangular sub-elements. They are defined by the position of the vertex opposite the hypotenuse \vec{P}_0 , the lengths of its sides a and b , and the unit vectors defining its sides \vec{n}_1 and \vec{n}_2 (see Fig. 3-8).

The analytic calculation of the potential from a right triangle is quite complex. The integral equation in terms of the local coordinates described in Figure 3-8 for the potential of a right triangle with surface charge density σ is

$$V = \frac{\sigma}{4\pi\epsilon_0} \int_{y_1}^{y_2} \int_{x_1}^{a+by} \frac{1}{\sqrt{x^2 + y^2 + z^2}} \cdot dx \cdot dy, \quad (3.39)$$

where $a = \frac{x_2 y_2 - x_1 y_1}{y_2 - y_1}$ and $b = \frac{x_1 - x_2}{y_2 - y_1}$. The inner integral can be evaluated using a common table of integrals, and after dividing by z to make the integral dimensionless, Equation 3.39 becomes

$$V = \frac{\sigma}{4\pi\epsilon_0} \cdot z \cdot \left[\int_{u_1}^{u_2} du \cdot \sinh^{-1} \left(\frac{a' + bu}{\sqrt{u^2 + 1}} \right) - \int_{u_1}^{u_2} du \cdot \sinh^{-1} \left(\frac{x'_1}{\sqrt{u^2 + 1}} \right) \right], \quad (3.40)$$

where $a' = \frac{a}{z}$, $u = \frac{y}{z}$, $u_i = \frac{y_i}{z}$, and $x'_1 = \frac{x_1}{z}$. If we define the following indefinite integrals

$$I_3(a, b, u) = \int \sinh^{-1} \left(\frac{a + bu}{\sqrt{u^2 + 1}} \right) \cdot du \quad (3.41)$$

and

$$I_4(x, u) = \int \sinh^{-1} \left(\frac{x}{\sqrt{u^2 + 1}} \right) \cdot du, \quad (3.42)$$

Equation 3.40 can be rewritten as

$$V = \frac{\sigma}{4\pi\epsilon_0} \cdot z \cdot [I_3(a', b, u_2) - I_3(a', b, u_1) - I_4(x_1, u_2) + I_4(x_1, u_1)]. \quad (3.43)$$

The analytic solutions for I_3 and I_4 are unfortunately rather unwieldy, and have therefore been reproduced in Appendix A. It should be noted that, while triangular sub-elements seem a much more versatile tool than rectangular sub-elements to use in replicating complicated geometries, the computational time for using triangular sub-elements is far greater than for their rectangular counterparts, and they are therefore used sparingly.

Ring sub-elements

A ring sub-element is defined in an axially symmetric coordinate system by a generating point $((R, Z)$ in Fig. 3-9), whose rotation about the z -axis defines the points on the ring. By symmetry, we can always define our field point to lie in the $\theta = 0$ plane, thus making the location of our field point $\vec{P} = (r, 0, z)$ in cylindrical coordinates. The distance from the field point to a point \vec{P}' on the ring (with coordinates (R, θ, Z))

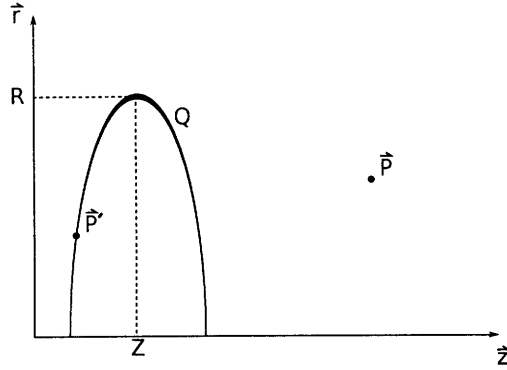


Figure 3-9: A ring sub-element in an axially symmetric system, defined by the generating point (R, Z) and charge Q . The field point is located at \vec{P} .

is defined as

$$\begin{aligned}
 |\vec{P} - \vec{P}'| &= \sqrt{(r - R \cos \theta)^2 + (R \sin \theta)^2 + (z - Z)^2} = \\
 &= \sqrt{R^2 + r^2 + (z - Z)^2 - 2Rr \cos \theta}.
 \end{aligned} \tag{3.44}$$

We refer to a linear charge density on the ring $\lambda = \frac{Q}{2\pi}$. With this, the formula for the potential at \vec{P} due to the ring generated by point \vec{P}' is

$$V = \frac{1}{4\pi\epsilon_0} \int_0^{2\pi} \frac{\lambda R \cdot d\theta}{\sqrt{R^2 + r^2 + (z - Z)^2 - 2Rr \cos \theta}}. \tag{3.45}$$

By noting that, for each point on the ring at θ , $0 < \theta < \pi$, there exists a corresponding point at $2\pi - \theta$ that contributes an equivalent amount to the electric potential, we can reduce the upper bound of the integral in Equation 3.45 by a factor of two, and double the value of the evaluated integral. Employing this trick and replacing λ with $\frac{Q}{2\pi}$, Equation 3.45 becomes

$$V = \frac{Q}{4\pi^2\epsilon_0} \int_0^{\pi} \frac{d\theta}{\sqrt{R^2 + r^2 + (z - Z)^2 - 2Rr \cos \theta}}. \tag{3.46}$$

Next, we can substitute $\alpha = \frac{\pi-\theta}{2}$ for θ , so that Equation 3.46 becomes

$$\begin{aligned} V &= \frac{Q}{4\pi^2\epsilon_0} \int_{\frac{\pi}{2}}^0 \frac{-2 \cdot d\alpha}{\sqrt{R^2 + r^2 + (z - Z)^2 - 2Rr \cos(\pi - 2\alpha)}} = \\ &= \frac{Q}{2\pi^2\epsilon_0} \int_0^{\frac{\pi}{2}} \frac{d\alpha}{\sqrt{R^2 + r^2 + (z - Z)^2 + 2Rr \cos(2\alpha)}}. \end{aligned} \quad (3.47)$$

By applying the double angle formula ($\cos(2x) = 1 - 2\sin^2(x)$) to Equation 3.47, we get

$$\begin{aligned} V &= \frac{Q}{2\pi^2\epsilon_0} \int_0^{\frac{\pi}{2}} \frac{d\alpha}{\sqrt{R^2 + r^2 + (z - Z)^2 + 2Rr(1 - 2\sin^2\alpha)}} = \\ &= \frac{Q}{2\pi^2\epsilon_0} \int_0^{\frac{\pi}{2}} \frac{d\alpha}{\sqrt{R^2 + r^2 + (z - Z)^2 + 2Rr - 4Rr \sin^2\alpha}}. \end{aligned} \quad (3.48)$$

We now introduce the parameters $S = \sqrt{(R+r)^2 + (z-Z)^2}$ and $k = \frac{2\sqrt{Rr}}{S}$, and recast Equation 3.48 in terms of these parameters:

$$V = \frac{Q}{2\pi^2\epsilon_0} \cdot \frac{1}{S} \cdot \int_0^{\frac{\pi}{2}} \frac{d\alpha}{\sqrt{1 - k^2 \sin^2\alpha}}. \quad (3.49)$$

The integral in Equation 3.49 is exactly the complete elliptic integral of the first kind $K(k)$, for which there are many well-known methods of calculation. The final form for the potential from a charged ring is therefore

$$V = \frac{Q}{2\pi^2\epsilon_0} \cdot \frac{K(k)}{S}. \quad (3.50)$$

Conic section sub-elements

A conic section sub-element is defined in an axially symmetric coordinate system by a generating line segment (connecting the points (R_a, Z_a) and (R_b, Z_b) as in Fig. 3-9, for example) and rotating it about the axis of symmetry. Using the results from the derivation of the potential from a charged ring, we can determine a formula for the potential due to a charged conic section by parameterizing Equation 3.50 and integrating over the length of the generating line. From Figure 3-10, it is clear that

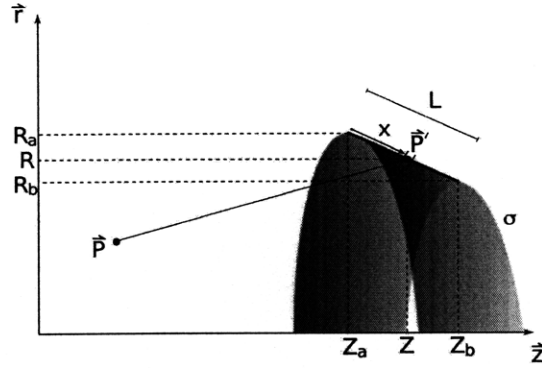


Figure 3-10: A conic section sub-element defined by the generating line connecting the points (R_a, Z_a) and (R_b, Z_b) , and surface charge density σ . The field point is defined as \vec{P} .

the length of the generating line is given by

$$L = \sqrt{(Z_a - Z_b)^2 + (R_a - R_b)^2}. \quad (3.51)$$

Our potential is therefore given by

$$V = \frac{\sigma}{\pi\epsilon_0} \cdot \int_0^L \frac{R(x) \cdot K(k(x))}{S(x)} \cdot dx, \quad (3.52)$$

where

$$R(x) = R_a + x \cdot \frac{R_b - R_a}{L} \quad (3.53)$$

and

$$Z(x) = Z_a + x \cdot \frac{Z_b - Z_a}{L} \quad (3.54)$$

define the (R, Z) coordinates of a ring generated by point \vec{P}' , and

$$S(x) = \sqrt{(R(x) + r)^2 + (z - Z(x))^2} \quad (3.55)$$

and

$$k(x) = \frac{2\sqrt{R(x) \cdot r}}{S(x)} \quad (3.56)$$

are the parameters introduced in Equation 3.49.

3.3.3 Implementation of the indirect BEM with electrode primitives

Now that we have defined our electrode primitives, we can use the indirect BEM to compute the resultant charge distributions across a configuration of primitives held at different potentials. For an arbitrary geometric configuration we consider a group of N sub-elements, each being a type of the aforementioned primitives. We define a geometric midpoint for each of the sub-elements, so that for each sub-element i there is an associated point \vec{r}_i that describes its location. Since we now have the equations necessary for computing the potential due to each sub-element for all points in space, we can construct the \overleftarrow{W} matrix defined in Equation 3.29, where $\frac{1}{\epsilon_0} \cdot W_{ij}$ represents the electric potential contribution of sub-element i with unit charge density at the field point \vec{r}_j . The vector \vec{U} is simply a vector of the potentials at which each sub-element is being held (i.e. U_i is the user-defined potential of the i -th sub-element).

There exist many techniques for solving the equation

$$\vec{U} = \overleftarrow{W} \cdot \vec{\sigma} \quad (3.57)$$

for $\vec{\sigma}$, but perhaps the most well-known approach is the method of Gaussian elimination [42] [43]. Regardless of how the equation is solved, the resultant σ_i components represent the charge distribution of sub-element i necessary to satisfy the given potential boundary conditions. With these charge distributions, the electric potential (and by differentiation, the electric field) due to the entire electrode configuration can be computed in all regions of space.

3.4 Magnetostatics

3.4.1 Introduction

While the BEM has been developed to facilitate the computation of magnetic fields, the configuration of the magnets in KATRIN make this approach unnecessary. Be-

cause the current applied to each of the magnets is independent of the other magnets in the experiment, its magnitude can be treated as an independent parameter, unlike the charge distribution for the electric components. It is therefore possible to directly calculate the magnetic field as a superposition of all of the magnets in the system, each with a user-defined current.

3.4.2 Geometry Primitives

The type of magnet that is of interest for use the KATRIN simulation is a superconducting magnet composed of axisymmetric coils with a rectangular cross-section, hereafter referred to as a *thick coil* (see Fig. 3-13). The formulae used to describe the scalar potential and magnetic fields for a thick coil are stated by Garrett [45] and described in greater detail by Glück [46] [47]. Due to the complexity of the calculations necessary to compute the field from such a magnet, only a semi-analytic computation of the field is used. In order to arrive at the formula for this computation, it is necessary to first understand the analytic solutions for computing the magnetic field from a circular current loop, and then from an infinitely thin solenoid. The magnetic field due to a thick coil is derived from these formulae.

Magnetic vector potential due to a circular current loop

We begin by defining a circular loop of current, generated by rotating point (R, Z) about the azimuthal axis, with current \vec{I} . We then define our field point $(r, 0, z)$ in a similar manner to the derivation of the potential due to a charged loop. A formula for the magnetic field is obtained by first deriving the magnetic vector potential \vec{A} , and then by taking its curl ($\vec{B} = \nabla \times \vec{A}$).

Using the coordinate frame described in Figure 3-11, we set up our equation for the magnetic vector potential as

$$\vec{A} = \frac{\mu_0 I}{4\pi} \int_0^{2\pi} \frac{R \cdot d\theta}{\sqrt{R^2 + r^2 + (z - Z)^2 - 2Rr \cos \theta}} \cdot \hat{\theta}, \quad (3.58)$$

where the denominator in the integral of Equation 3.58 is simply the distance from

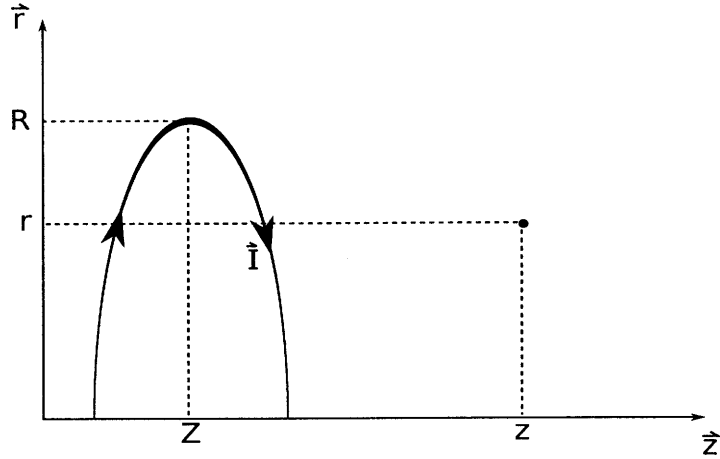


Figure 3-11: A circular current loop with current \vec{I} , generating point (R, Z) , and an off-axis field point (r, z) .

the field point to a point on the ring, taken from Equation 3.44, and \vec{A} is in the same direction as \vec{I} (in other words, $\frac{\vec{A}}{|\vec{A}|} = \frac{\vec{I}}{|\vec{I}|}$). By converting $\hat{\theta}$ into Cartesian coordinates, Equation 3.58 becomes

$$\vec{A} = \frac{\mu_0 I}{4\pi} \left[\int_0^{2\pi} \frac{-R \sin(\theta) \cdot d\theta}{\sqrt{R^2 + r^2 + (z - Z)^2 - 2Rr \cos \theta}} \cdot \hat{x} + \int_0^{2\pi} \frac{R \cos(\theta) \cdot d\theta}{\sqrt{R^2 + r^2 + (z - Z)^2 - 2Rr \cos \theta}} \cdot \hat{y} \right]. \quad (3.59)$$

By symmetry, we can see that the first integral in Equation 3.59 must equal zero (since, for $0 < \theta < \pi$, there exists a contribution equal in magnitude and opposite in sign from $\theta' = 2\pi - \theta$). Furthermore, symmetry dictates that the contribution of the second integral from $0 \rightarrow \pi$ is identical in magnitude to the the contribution from $\pi \rightarrow 2\pi$, so we are able to halve the upper limit of integration and count its contribution twice (as was done for the calculation of the electric potential from a charged ring). Applying these symmetry arguments and converting back into cylindrical coordinates, Equation 3.59 becomes

$$\vec{A} = \frac{\mu_0 I}{2\pi} \int_0^\pi \frac{R \cdot \cos(\theta) \cdot d\theta}{\sqrt{R^2 + r^2 + (z - Z)^2 - 2Rr \cos \theta}} \cdot \hat{\theta}. \quad (3.60)$$

As was done in Equation 3.47 for the charged ring, we substitute $\alpha = \frac{\pi-\theta}{2}$ for θ , so that Equation 3.60 becomes

$$\vec{A} = \frac{\mu_0 I}{2\pi} \cdot R \cdot \int_0^{\frac{\pi}{2}} \frac{-2 \cdot \cos(2\alpha) \cdot d\alpha}{\sqrt{R^2 + r^2 + (z - Z)^2 + 2Rr \cos 2\alpha}} \cdot \hat{\theta}. \quad (3.61)$$

By applying the double angle formula ($\cos(2x) = 1 - 2\sin^2(x)$) to Equation 3.61, our formula becomes

$$\vec{A} = \frac{\mu_0 I}{2\pi} \cdot R \cdot \int_0^{\frac{\pi}{2}} \frac{-2 \cdot (1 - 2\sin^2(\alpha)) \cdot d\alpha}{\sqrt{R^2 + r^2 + (z - Z)^2 + 2Rr(1 - 2\sin^2(\alpha))}} \cdot \hat{\theta}. \quad (3.62)$$

By substituting $S = \sqrt{(R + r)^2 + (z - Z)^2}$ and $k = \frac{2\sqrt{Rr}}{S}$ into Equation 3.62, we get

$$\vec{A} = \frac{\mu_0 I}{\pi} \cdot \frac{R}{S} \cdot \left[\int_0^{\frac{\pi}{2}} \frac{-d\alpha}{\sqrt{1 - k^2 \sin^2(\alpha)}} + \int_0^{\frac{\pi}{2}} \frac{2\sin^2(\alpha) \cdot d\alpha}{\sqrt{1 - k^2 \sin^2(\alpha)}} \right] \cdot \hat{\theta}. \quad (3.63)$$

The first integral in Equation 3.63 is clearly in the form of the complete elliptic integral of the first kind ($K(k)$). For the second integral, we note that its integrand can be rewritten as

$$\frac{\sin^2(\alpha)}{\sqrt{1 - k^2 \sin^2(\alpha)}} = \frac{1}{k^2} \left(\frac{1}{\sqrt{1 - k^2 \sin^2(\alpha)}} - \sqrt{1 - k^2 \sin^2(\alpha)} \right) \quad (3.64)$$

and that the complete elliptic integral of the second kind is defined as

$$E(k) = \int_0^{\frac{\pi}{2}} \sqrt{1 - k^2 \sin^2(\alpha)} \cdot d\alpha. \quad (3.65)$$

Using these relations, we redefine Equation 3.63 as

$$\vec{A} = \frac{\mu_0 I}{\pi} \cdot \frac{R}{S} \cdot \left[\frac{2(K(k) - E(k))}{k^2} - K(k) \right] \cdot \hat{\theta}, \quad (3.66)$$

which is the final form of the magnetic vector potential for a circular current loop.

Since \vec{A} only contains an azimuthal component, we can rewrite Equation 3.66 as

$$\vec{A} = A_\theta^L \cdot \hat{\theta}, \quad (3.67)$$

where the subscript θ implies that A_θ^L represents the θ -component of the vector potential, and the superscript L denotes that the calculation was made for a current loop. Using this formalism, the magnetic field can be written as

$$\vec{B}^L = (B_r^L, B_\theta^L, B_z^L) = \left(-\frac{\partial A_\theta^L}{\partial z}, 0, \frac{1}{r} \cdot \frac{\partial(r \cdot A_\theta^L)}{\partial r} \right). \quad (3.68)$$

In order to solve for B_r^L and B_z^L , it is necessary to know the derivatives of the complete elliptic integrals of the first and second kind. They are given by Durand [48] as

$$\frac{dK(k)}{dk} = \frac{E(k)}{k(1-k^2)} - \frac{K(k)}{k} \quad (3.69)$$

and

$$\frac{dE(k)}{dk} = \frac{E(k) - K(k)}{k}. \quad (3.70)$$

Using Equations 3.69 and 3.70, it is possible to explicitly solve for B_r and B_z in Equation 3.68 to be

$$B_r^L = \frac{\mu_0 I}{4\pi} \cdot \frac{(z-Z)R}{S} \left[\frac{2}{k^2 S^2} (E(k) - K(k)) + \frac{1}{D^2} E(k) \right] \quad (3.71)$$

and

$$B_z^L = \frac{\mu_0 I}{2\pi S} \left[K(k) - E(k) + 2 \frac{R(R-r)}{D^2} E(k) \right], \quad (3.72)$$

where $D = \sqrt{(R-r)^2 + (z-Z)^2}$.

Magnetic vector potential due to an infinitely thin solenoid

The magnetic scalar potential from a solenoid with dimensions described in Figure 3-12 can be analytically determined by integrating Equation 3.66 from Z_a to Z_b . The technique for performing this integral involves exploiting the recursive nature of the

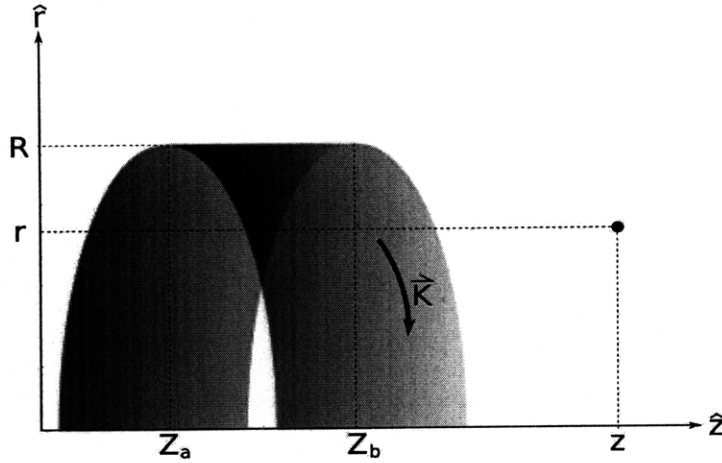


Figure 3-12: A solenoid with a circular cross-section of radius R , with endpoints at Z_a and Z_b , axial surface current \vec{K} , and an off-axis field point (r, z) .

derivatives of all three complete elliptic integrals. The first two elliptic integrals and their derivatives are defined in Equations 3.49, 3.65, 3.69 and 3.70, and the definition of the third complete elliptic integral and its partial derivative are

$$\Pi(m, k) = \int_0^{\frac{\pi}{2}} \frac{d\alpha}{(1 - m \sin^2 \alpha) \sqrt{1 - k^2 \sin^2 \alpha}} \quad (3.73)$$

and

$$\left(1 - \frac{m^2}{k^2}\right) \frac{\partial \Pi(m, k)}{\partial k} = \frac{1}{k} \left(\frac{E(k)}{1 - k^2} - \Pi(m, k) \right). \quad (3.74)$$

By manipulating these formulae, it can be shown that the equation for the magnetic vector potential from a solenoid is

$$\vec{A}^S = |\vec{K}| \cdot \left(\tilde{A}_\theta(Z_b) - \tilde{A}_\theta(Z_a) \right) \cdot \hat{\theta} = A_\theta^S \cdot \hat{\theta}, \quad (3.75)$$

where

$$\begin{aligned} \tilde{A}_\theta(Z) &= \int \frac{A_\theta^L}{I} \cdot dZ = & (3.76) \\ &= \frac{\mu_0}{\pi} \cdot \frac{R(z - Z)}{S} \cdot \left\{ \frac{1}{k^2} (E(k) - K(k)) + \left(\frac{1}{c^2 - 1} \right) (\Pi(c, k) - K(k)) \right\}, \end{aligned}$$

and $c = \frac{2\sqrt{Rr}}{R+r}$.

Once again, we can determine the magnetic field by computing the curl of the vector potential:

$$\vec{B}^S = (B_r^S, B_\theta^S, B_z^S) = \left(-\frac{\partial A_\theta^S}{\partial z}, 0, \frac{1}{r} \cdot \frac{\partial(r \cdot A_\theta^S)}{\partial r} \right). \quad (3.77)$$

It is beneficial to introduce the terms $\tilde{B}_r(Z) = \frac{-\partial \tilde{A}_\theta}{\partial z}$ and $\tilde{B}_z(Z) = \frac{1}{r} \cdot \frac{\partial(r \cdot \tilde{A}_\theta)}{\partial r}$, so that

$$B_r^S = |\vec{K}| \cdot \left(\tilde{B}_r(Z_b) - \tilde{B}_r(Z_a) \right) \quad (3.78)$$

and

$$B_z^S = |\vec{K}| \cdot \left(\tilde{B}_z(Z_b) - \tilde{B}_z(Z_a) \right). \quad (3.79)$$

By once again exploiting the recursive properties of the complete elliptic integrals, it is possible to compute $\tilde{B}_r(Z)$ and $\tilde{B}_z(Z)$ to be

$$\tilde{B}_r(Z) = -\frac{\mu_0}{\pi} \cdot \frac{R}{S} \left\{ \frac{2}{k^2} (E(k) - K(k)) + K(k) \right\} \quad (3.80)$$

and

$$\tilde{B}_z(Z) = -\frac{\mu_0}{\pi} \cdot \frac{R(z-Z)}{S(R+r)} \left\{ K(k) + \frac{R-r}{2R} (\Pi(c, k) - K(k)) \right\}. \quad (3.81)$$

Magnetic vector potential due to a thick coil

Having described the magnetic fields for the cases of a circular current loop and an infinitely thin solenoid, we now have the requisite tools for describing the properties of a magnetic field from a thick coil symmetric about the z -axis.⁶ A thick coil is defined by the z -coordinate of the middle of the coil Z_{mid} , the magnitude of its inner radius R_a , the thickness of the coil in the radial direction R_{th} , its length in the z -dimension L , and the magnitude of its current density J . Converting from these parameters to the ones used to compute the field (described in Fig. 3-13) is a trivial operation,

⁶For *tilted coils*, or thick coils whose axis of symmetry is not the z -axis, the field can be solved using the general methods for thick coils in a local coordinate frame, and then converted back to the global frame.

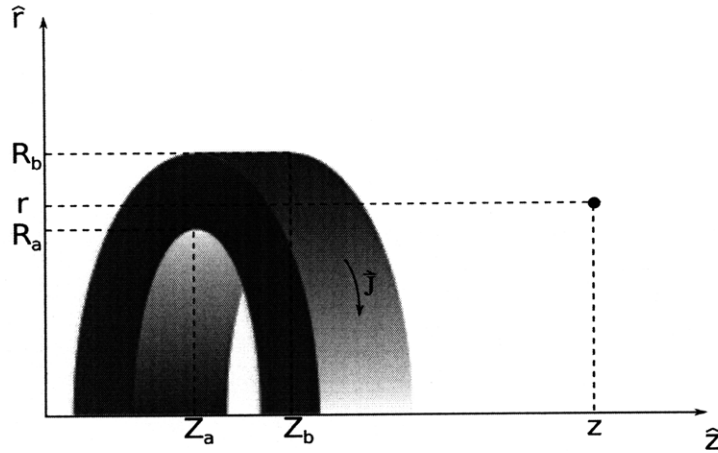


Figure 3-13: A thick coil with volume current density \vec{J} , generated by rotating a rectangle with corners (R_a, Z_a) and (R_b, Z_b) about the z -axis, and an off-axis field point (r, z) .

described in Table 3.1.

Parameters used in Field Computation	Equivalent Parameters in Thick Coil Description
R_a	R_a
R_b	$R_a + R_{th}$
Z_a	$Z_{mid} - \frac{L}{2}$
Z_b	$Z_{mid} + \frac{L}{2}$
$ \vec{J} $	J

Table 3.1: Conversion from the input parameters of a thick coil to the parameters used in the calculation of its field.

To compute the magnetic vector potential from a thick coil, we perform an integration over Equation 3.75, as follows:

$$\vec{A}^{TC} = \left(\int_{R_a}^{R_b} A_\theta^S \cdot dR \right) \cdot \hat{\theta} = |\vec{J}| \cdot \left(\int_{R_a}^{R_b} \left(\tilde{A}_\theta(Z_b) - \tilde{A}_\theta(Z_a) \right) \cdot dR \right) \cdot \hat{\theta}. \quad (3.82)$$

Equation 3.82 can be solved by numerical integration techniques. Similarly, the r and z -components of the magnetic field can be determined by performing a numerical

integration over Equations 3.78 and 3.79:

$$B_r^{TC} = \int_{R_a}^{R_b} B_r^S \cdot dR = |\vec{J}| \cdot \int_{R_a}^{R_b} \left(\tilde{B}_r(Z_B) - \tilde{B}_r(Z_A) \right) \cdot dR, \quad (3.83)$$

and

$$B_z^{TC} = \int_{R_a}^{R_b} B_z^S \cdot dR = |\vec{J}| \cdot \int_{R_a}^{R_b} \left(\tilde{B}_z(Z_B) - \tilde{B}_z(Z_A) \right) \cdot dR. \quad (3.84)$$

3.5 Summary

The techniques described in this chapter provide a means for the direct computation of electrostatic and magnetostatic fields in all regions of the KATRIN experiment (provided that a combination of the defined sub-elements can accurately describe the actual geometry of the experiment). As a standalone set of routines, the direct calculation method is a theoretically sufficient toolkit for field generation. However, it will be shown in Chapter 6 that this method is somewhat limited in practical application, due to the time required to perform the required calculations for each sub-element. Even with the inclusion of streamlined computational techniques (such as those present in mathematics libraries, for example) and the utilization of more powerful computers, the direct calculation method suffers from the fact that its computation time scales with the accuracy of the discretization of the geometry. As a result, the method is best suited as a fail-safe; in regions where faster methods fail, the direct calculation method will always hold valid.

Chapter 4

Calculation of Electric and Magnetic Fields via Zonal Harmonic Expansion

4.1 Introduction

The next technique used to calculate electrostatic and magnetostatic fields is the method of zonal harmonic expansion. Though the principle concepts surrounding the method are well established in the field of electricity and magnetism, the application of the technique to computational analysis has been developed in great detail by Garrett [49] for magnetostatic systems, and by Glück for both magnetostatic [46][50] and electrostatic [46][51] systems. The general idea of the method is to expand the equation for the field of an axially symmetric system into a convergent sum of terms involving previously computed source constants and Legendre polynomials, where each term individually satisfies the Laplace equation. While the restrictions of axial symmetry and confinement to regions of convergence limit its applicability, this method facilitates the rapid computation of electric and magnetic fields because the terms in the series are largely recursive, and because the series expansions tend to converge rapidly in practice (see Chapter 6 for comparisons of computation speed to other methods.) These benefits make the method very useful for applied use in simulations that require the repeated calculation of fields.

The first half of this chapter is devoted to the description, derivation and imple-

mentation of the method of zonal harmonics in electrostatics. The axially symmetric electrode geometry primitives introduced in Section 3.3 are used in the method's application. The latter half of the chapter describes the utilization of the method in magnetostatics, with specific application to the magnetic geometry primitives defined in Section 3.4.

4.2 Legendre polynomials in electrostatics

The Legendre polynomials arise naturally in electrostatics for the computation of electric potential, as they are a complete set of orthonormal functions which satisfy the *Laplace equation* ($\nabla^2\Phi = 0$) in spherical coordinates. In particular, the use of Legendre polynomials to describe electric fields generated by charge distributions having azimuthal symmetry is well covered in most electromagnetism texts [30] [40]. The canonical general solution to these problems is of the form

$$\Phi(r, \theta) = \sum_{n=0}^{\infty} [A_n r^n + B_n r^{-(n+1)}] P_n(\cos \theta), \quad (4.1)$$

where $P_n(x)$ represents the Legendre polynomial of order n . The addends of the summation in equation 4.1 are also referred to as zonal harmonics [51] [49].

4.2.1 Regions of convergence

The Laplace equation is only valid in regions with no electric charge (it is a special case of the Poisson equation, $\nabla^2\Phi = -\frac{\rho}{\epsilon_0}$, where the charge density $\rho = 0$). As a result, solutions to the Laplace equation have restricted domains where they are valid (with the trivial exception where $\rho = 0$ for all space).

As can be seen in Eq. 4.1, there are two sets of coefficients in the general solution for electric potential (A_n and B_n), and often only one set contains nonzero values. Conceptually, it is most convenient to imagine the electrode configuration in a local spherical coordinate system with its origin at a *source point* S , and discretize the system into concentric spherical shells about the source point that contain no charge

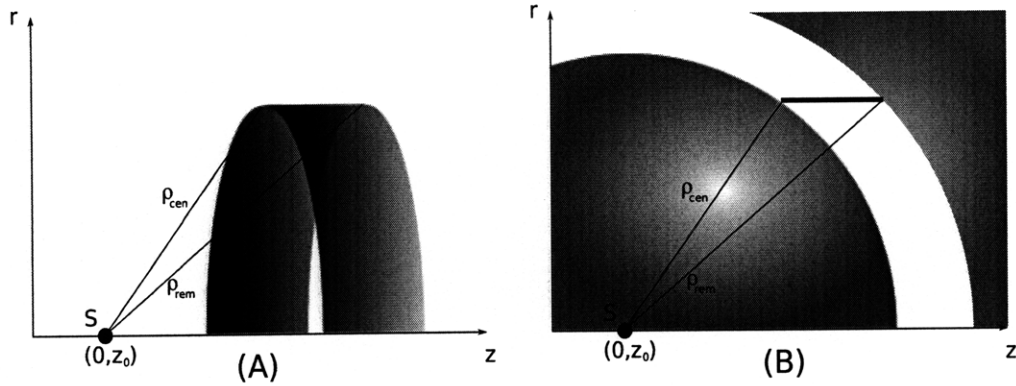


Figure 4-1: (A) A 3-dimensional rendering of an axially symmetric charged cylindrical electrode and (B) the regions of convergence for central and remote zonal harmonic expansion from a source point S .

(see Fig. 4-1). If there is no charge at the origin, the system will contain a finite spherical region with a boundary at the closest charge (defined by ρ_{cen} , the shortest distance from the origin to a charge). This region necessarily has $B_n = 0 \forall n$, since the potential at the origin must be finite. Assuming there is no charge radially outward to infinity, the system will also contain an infinitely large spherical shell with an inner boundary at the farthest charge (defined by ρ_{rem} , the longest distance from the origin to a charge). Likewise, this region has $A_n = 0 \forall n$, since the potential must approach zero for large radial values.¹

The two regions of space described above each have a unique set of coefficients and different formulae for electric potential and electric field computation. It is therefore natural to split the discussion of the zonal harmonic expansion technique between these two regions, hereafter referred to as *central* ($\rho < \rho_{cen}$) and *remote* ($\rho > \rho_{rem}$) expansions.

¹Regions can be constructed for certain geometries that would require both sets of coefficients to be nonzero (with charges restricting the inner and outer boundaries), but they are uncommon given KATRIN's geometrical configuration and in these regions another field method is used.

4.2.2 Derivation of electric field components from electric potential

Formalism

Before continuing, it is convenient to adopt the formalism of Glück [51]: the formalism uses cylindrical coordinates (r_{cyl}, z_{cyl}) , and redefines parameters to facilitate ease of implementation in programming. We redefine equation 4.1 as such:

$$\Phi(r_{cyl}, z_{cyl}) = \Phi_{cen}(r_{cyl}, z_{cyl}) + \Phi_{rem}(r_{cyl}, z_{cyl}), \quad (4.2)$$

where

$$\Phi_{cen}(r_{cyl}, z_{cyl}) = \sum_{n=0}^{\infty} \Phi_n^{cen}|_{z_0} \left(\frac{\rho}{\rho_{cen}} \right)^n P_n(\cos \theta) \quad (4.3)$$

and

$$\Phi_{rem}(r_{cyl}, z_{cyl}) = \sum_{n=0}^{\infty} \Phi_n^{rem}|_{z_0} \left(\frac{\rho}{\rho_{rem}} \right)^{-(n+1)} P_n(\cos \theta), \quad (4.4)$$

and $\rho = \sqrt{r_{cyl}^2 + (z_{cyl} - z_0)^2}$, $\theta = \arctan \frac{r_{cyl}}{(z_{cyl} - z_0)} = \arccos \frac{\rho}{(z_{cyl} - z_0)}$, and the coefficients Φ_n^{cen} , Φ_n^{rem} are evaluated with z_0 as the origin of the local spherical coordinate system.

The following substitutions have been made:

$$\begin{aligned} r &\rightarrow \rho = \sqrt{r_{cyl}^2 + (z_{cyl} - z_0)^2}, \\ \theta &\rightarrow \arctan \frac{r_{cyl}}{(z_{cyl} - z_0)}, \\ A_n &\rightarrow \Phi_n^{cen}|_{z_0} (\rho_{cen})^{-n}, \\ B_n &\rightarrow \Phi_n^{rem}|_{z_0} (\rho_{rem})^{(n+1)}, \end{aligned}$$

but have left intact the form of equation 4.1.

It is important to note that the n -th term of Equations 4.3 and 4.4 contain the respective terms $\left(\frac{\rho}{\rho_{cen}} \right)^n$ and $\left(\frac{\rho}{\rho_{rem}} \right)^{-(n+1)}$, which decrease rapidly for large n . It is possible to deduce from these scaling parameters that field points that have smaller values for $\left(\frac{\rho}{\rho_{cen}} \right)$ or $\left(\frac{\rho_{rem}}{\rho} \right)$ (and are therefore farther away from the nearest or farthest geometry primitive, respectively) will require fewer terms to converge upon the field

value (given a constant error tolerance). The general property that the speed of convergence is proportional to the distance from the geometry primitives is common to all of the zonal harmonic expansion formulae described in this chapter.

Central expansion

In the central region, $\Phi_{rem} = 0$, and we are left with $\Phi = \Phi_{cen}$. To derive analytic solutions for the electric field in the central region, we must use the following properties of zonal harmonics [49]:

$$\frac{\partial}{\partial z_{cyl}}(\rho^n P_n(\cos \theta)) = n\rho^{n-1} P_{n-1}(\cos \theta) \quad (4.5)$$

and

$$\frac{\partial}{\partial r_{cyl}}(\rho^n P_n(\cos \theta)) = -\sin \theta \rho^{n-1} P'_{n-1}(\cos \theta). \quad (4.6)$$

Applying 4.5 to 4.3, the electric field in the z_{cyl} -direction is

$$\begin{aligned} E_{z_{cyl}} &= -\frac{\partial}{\partial z_{cyl}} (\Phi_{cen}(r_{cyl}, z_{cyl})) = \\ &= -\sum_{n=1}^{\infty} \Phi_n^{cen}|_{z_0} \left(\frac{n}{\rho_{cen}}\right) \left(\frac{\rho}{\rho_{cen}}\right)^{n-1} P_{n-1}(\cos \theta). \end{aligned} \quad (4.7)$$

Similarly, applying 4.6 to 4.3 gives the electric field in the r_{cyl} -direction:

$$\begin{aligned} E_{r_{cyl}} &= -\frac{\partial}{\partial r_{cyl}} (\Phi_{cen}(r_{cyl}, z_{cyl})) = \\ &= \sum_{n=1}^{\infty} \Phi_n^{cen}|_{z_0} \left(\frac{\sin \theta}{\rho_{cen}}\right) \left(\frac{\rho}{\rho_{cen}}\right)^{n-1} P'_{n-1}(\cos \theta). \end{aligned} \quad (4.8)$$

Remote expansion

In the remote region, $\Phi_{cen} = 0$, leaving us with $\Phi = \Phi_{rem}$. For the derivation of Φ_{rem} , the following zonal harmonics relations are needed [52]:

$$\frac{\partial}{\partial z_{cyl}}(\rho^{-(n+1)} P_n(\cos \theta)) = -(n+1)\rho^{-(n+2)} P_{n+1}(\cos \theta) \quad (4.9)$$

and

$$\frac{\partial}{\partial r_{cyl}}(\rho^{-(n+1)}P_n(\cos\theta)) = -\sin\theta\rho^{-(n+2)}P'_{n+1}(\cos\theta). \quad (4.10)$$

Applying equations 4.9 and 4.10 to 4.4, we derive the electric field in the remote region to be

$$\begin{aligned} E_{z_{cyl}} &= -\frac{\partial}{\partial z_{cyl}}(\Phi_{rem}(r_{cyl}, z_{cyl})) = \\ &= \sum_{n=1}^{\infty} \Phi_{(n-1)}^{rem}|_{z_0} \frac{n}{\rho_{rem}} \left(\frac{\rho}{\rho_{rem}}\right)^{-(n+1)} P_n(\cos\theta) \end{aligned} \quad (4.11)$$

and

$$\begin{aligned} E_{r_{cyl}} &= -\frac{\partial}{\partial r_{cyl}}(\Phi_{rem}(r_{cyl}, z_{cyl})) = \\ &= \sum_{n=1}^{\infty} \Phi_{(n-1)}^{rem}|_{z_0} \frac{\sin\theta}{\rho_{rem}} \left(\frac{\rho}{\rho_{rem}}\right)^{-(n+1)} P'_n(\cos\theta). \end{aligned} \quad (4.12)$$

4.2.3 Calculating Source Constants

This section describes the computation of the coefficients to the zonal harmonic expansion, $\Phi_n^{cen}|_{z_0}$ and $\Phi_n^{rem}|_{z_0}$, hereafter referred to as *source constants*. The techniques described in this chapter were derived by Glück [51]. The method is first demonstrated using a trivial geometry in order to describe the principles of implementation. Following this, the method is applied to more general geometrical configurations for practical use.

Central source constants for a charged ring

Given a circular ring with charge Q and radius R and centered at Z , we shall place a source point S on the z -axis at $(0, z_0)$ (see fig. 4-2). In order to compute the coefficients of the Legendre polynomial expansion about S for electric potential, we must first determine the potential at F , an arbitrary on-axis point located at $(0, z)$, and then convert this solution to an infinite sum involving the Legendre polynomials and equate it piece-wise with our ansatz, defined in equation 4.2.

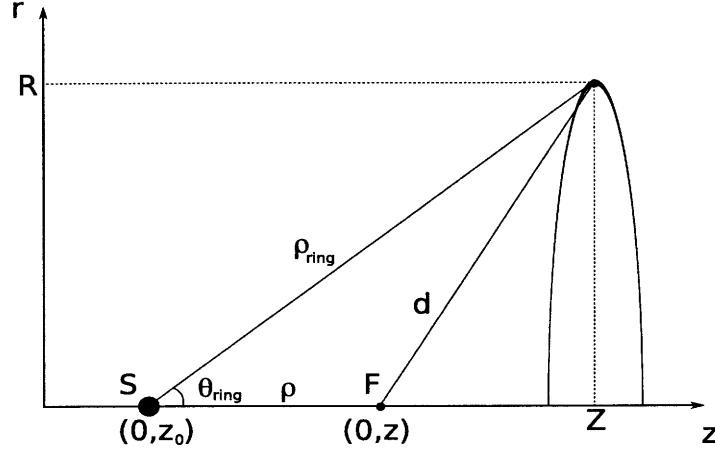


Figure 4-2: Graphical depiction of a charged ring with generating point (R, Z) , a central source point (S) , and an arbitrary on-axis field point (F) .

Since the distance d between infinitesimal segments of the ring and F is constant, the potential at F due to the charged ring (with linear charge density $\lambda = \frac{Q}{2\pi R}$) is simply

$$\Phi(F) = \frac{\lambda}{4\pi\epsilon_0} \int_0^{2\pi R} \frac{dl'}{d} = \frac{1}{4\pi\epsilon_0} \frac{Q}{d}. \quad (4.13)$$

We can convert this equation into a Legendre polynomial expansion by manipulating our definition of $\frac{1}{d}$ as follows: first, we define $\rho = |z_0 - z|$ and $\rho_{ring} = \sqrt{(Z - z_0)^2 + R^2}$. Then we can redefine d in terms of these variables as

$$d = \sqrt{\rho_{ring}^2 + \rho^2 - 2\rho_{ring}\rho \cos \theta_{ring}}, \quad (4.14)$$

where $\cos \theta_{ring} = \frac{|Z - z_0|}{\rho_{ring}}$. Substituting $h_{cen} = \frac{\rho}{\rho_{ring}}$ into equation 4.14 and inverting both sides, we obtain

$$\frac{1}{d} = \frac{1}{\rho_{ring} \sqrt{1 + h_{cen}^2 - 2h_{cen} \cos \theta_{ring}}}. \quad (4.15)$$

Since this is of the form of the Legendre polynomial generating function, we can

express equation 4.15 as

$$\frac{1}{d} = \frac{1}{\rho_{ring}} \sum_{n=0}^{\infty} h_{cen}^n P_n(\cos \theta_{ring}), \quad (4.16)$$

and recombine equations 4.13 and 4.16 to get

$$\Phi(F) = \frac{Q}{4\pi\epsilon_0} \frac{1}{\rho_{ring}} \sum_{n=0}^{\infty} h_{cen}^n P_n(\cos \theta_{ring}). \quad (4.17)$$

Now that we have a solution for the electric potential at point F in terms of Legendre polynomials, we can compare it to our solution derived using our ansatz (eq. 4.3). Since F was chosen to be on-axis (and therefore forms an angle $\theta = 0$ with the z -axis), we exploit the fact that Legendre polynomials are standardized so that $P_n(\cos 0) = P_n(1) = 1$, reducing our ansatz for point F to

$$\Phi(F) = \sum_{n=0}^{\infty} \Phi_n^{cen}|_{z_0} \left(\frac{\rho}{\rho_{cen}} \right)^n. \quad (4.18)$$

Comparing equations 4.17 and 4.18 and equating like terms, we arrive at a definition for the central source constants for source point S:²

$$\Phi_n^{cen}|_{z_0} = \frac{Q}{4\pi\epsilon_0} \frac{1}{\rho_{ring}} \left(\frac{\rho_{cen}}{\rho_{ring}} \right)^n P_n(\cos \theta_{ring}). \quad (4.19)$$

Remote source constants for a charged ring

The approach used in the previous section can be used for the computation of the remote source coefficients as well. Starting with equation 4.14, we can substitute $h_{rem} = \frac{\rho_{ring}}{\rho}$ into the equation and invert both sides to get

$$\frac{1}{d} = \frac{1}{\rho \sqrt{1 + h_{rem}^2 - 2h_{rem} \cos \theta_{ring}}} \quad (4.20)$$

²It is advantageous to omit the relation that, for the special case of a ring, $\rho_{cen} = \rho_{rem} = \rho_{ring}$. By keeping these values distinct, it will be easier to apply the results of the ring calculation to a general axially symmetric geometry configuration.

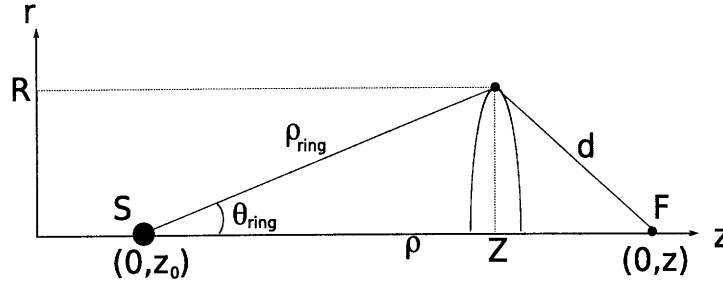


Figure 4-3: Graphical depiction of a charged ring with generating point (R, Z) , a remote source point (S) , and an arbitrary on-axis field point (F) .

which, as before, can be expressed in terms of Legendre polynomials as

$$\begin{aligned} \frac{1}{d} &= \frac{1}{\rho} \sum_{n=0}^{\infty} h_{rem}^n P_n(\cos \theta_{ring}) = \\ &= \frac{1}{\rho_{ring}} \sum_{n=0}^{\infty} (h_{rem})^{n+1} P_n(\cos \theta_{ring}) \end{aligned} \quad (4.21)$$

The remote source constants for source point S can then be computed in a similar manner as were the central source constants. They are defined as

$$\Phi_n^{rem}|_{z_0} = \frac{Q}{4\pi\epsilon_0} \frac{1}{\rho_{ring}} \left(\frac{\rho_{ring}}{\rho_{rem}} \right)^{(n+1)} P_n(\cos \theta_{ring}). \quad (4.22)$$

Source constants for a charged conic section

Using the results for the charged ring, it is a straightforward task to determine the formulae for the source coefficients of a charged axially symmetric conic section, such as the one depicted in Figure 4-4. Since the conic section can be seen as a composite of infinitesimally thin charged rings, the only steps needed to extend the results of Equations 4.19 and 4.22 are to properly parametrize the components of the formulae, and then to simply integrate over the length of the conic section. One method for achieving this is demonstrated below.

Given a conic section with charge density σ and described by the line connecting two points (R_a, Z_a) and (R_b, Z_b) , and a source point S located at $(0, z_0)$, we choose

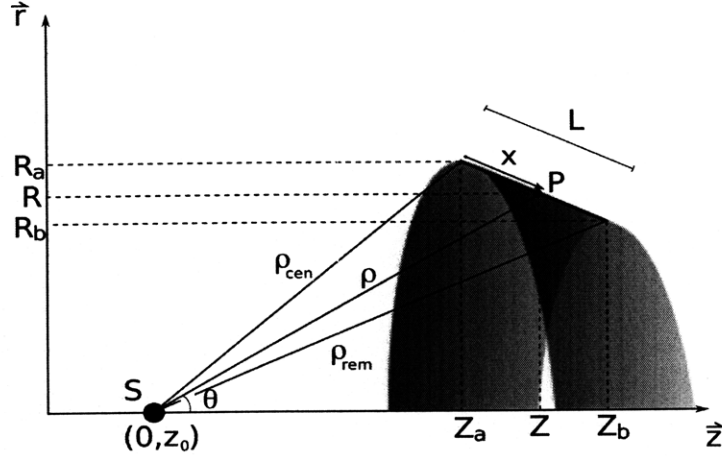


Figure 4-4: Graphical depiction of a charged conic section generated by the line connecting (R_a, Z_a) and (R_b, Z_b) with length L , and a central source point (S) .

as our parametrizing variable x , the length between a point P on the conic section's generating line and the endpoint of the line (see Fig. 4-4). With this parameterization, the definitions for our central and remote source constants, respectively, become

$$\Phi_n^{cen}|_{z_0} = \int_0^L dx \cdot \frac{(\sigma \cdot 2\pi R(x))}{4\pi\epsilon_0} \cdot \frac{1}{\rho(x)} \cdot \left(\frac{\rho_{cen}}{\rho(x)}\right)^n P_n(\cos(\theta(x))) \quad (4.23)$$

and

$$\Phi_n^{rem}|_{z_0} = \int_0^L dx \cdot \frac{(\sigma \cdot 2\pi R(x))}{4\pi\epsilon_0} \cdot \frac{1}{\rho(x)} \cdot \left(\frac{\rho(x)}{\rho_{rem}}\right)^{(n+1)} P_n(\cos(\theta(x))), \quad (4.24)$$

where

$$L = \sqrt{(Z_a - Z_b)^2 + (R_a - R_b)^2} \quad (4.25)$$

describes the length of the generating line segment,

$$R(x) = R_a + x \cdot \frac{(R_b - R_a)}{L} \quad (4.26)$$

and

$$Z(x) = Z_a + x \cdot \frac{(Z_b - Z_a)}{L} \quad (4.27)$$

define the (r, z) coordinates of P ,

$$\rho(x) = \sqrt{(R(x))^2 + (Z(x) - z_0)^2} \quad (4.28)$$

is the distance between P and the source point S , and

$$\cos(\theta(x)) = \frac{(Z(x) - z_0)}{\rho(x)}. \quad (4.29)$$

is the angle formed by the intersection of the z -axis and the line connecting P and S . For application purposes, these integrals can be computed numerically.

Source constants for a general axially symmetric system

Since electric potential is linear in charge (and therefore obeys the law of superposition), the generalization to M coaxial conic sections can be achieved by simply summing the source constants for each conic section:

$$\Phi_n^{cen}|_{z_0} = \sum_{m=1}^M (\Phi_n^{cen}|_{z_0})_m, \quad (4.30)$$

$$\Phi_n^{rem}|_{z_0} = \sum_{m=1}^M (\Phi_n^{rem}|_{z_0})_m. \quad (4.31)$$

For distances sufficiently far from the electrodes, it is also possible to use this tech-

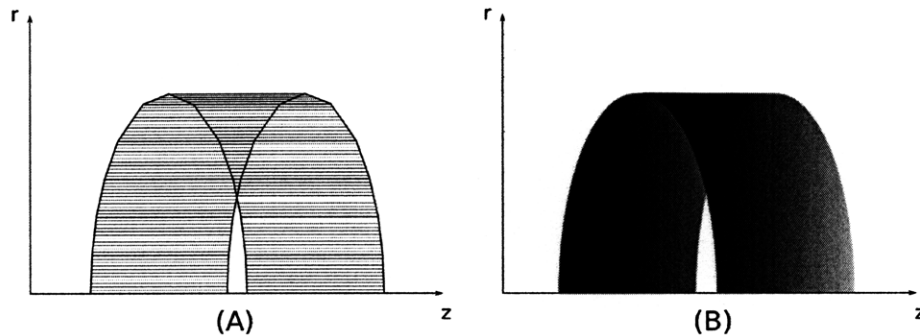


Figure 4-5: (A) An axially symmetric wire configuration and (B) its electrode approximation.

nique to describe the electric field for coaxial wire planes, by approximating them as conic sections (see Fig. 4-5).

4.3 Legendre polynomials in magnetostatics

In regions where the current density is zero, it is possible to define a *magnetic scalar potential* Ψ , such that $\nabla^2\Psi = 0$ and $\vec{B} = -\nabla\Psi$ [30]. In regions where it exists, Ψ is analogous to the electric potential Φ , as they both satisfy the Laplace equation and can be differentiated to calculate their respective fields. As such, a solution with the form of equation 4.1 must exist for Ψ as well when the geometries describing the magnetostatic fields are axially symmetric. Because of this fact, it is possible to apply the technique of Legendre polynomial expansion for solving magnetic fields, as well. The general form of the magnetic scalar potential in this expansion (modified to simplify the expressions for the magnetic field) is

$$\Psi(r_{cyl}, z_{cyl}) = \Psi_{cen}(r_{cyl}, z_{cyl}) + \Psi_{rem}(r_{cyl}, z_{cyl}), \quad (4.32)$$

where

$$\Psi_{cen}(r_{cyl}, z_{cyl}) = \sum_{n=0}^{\infty} \Psi_n^{cen}|_{z_0} \left(\frac{-\rho_{cen}}{n+1} \right) \left(\frac{\rho}{\rho_{cen}} \right)^{n+1} P_{n+1}(\cos\theta), \quad (4.33)$$

$$\Psi_{rem}(r_{cyl}, z_{cyl}) = \sum_{n=1}^{\infty} \Psi_{n+1}^{rem}|_{z_0} \left(\frac{\rho_{rem}}{n+1} \right) \left(\frac{\rho}{\rho_{rem}} \right)^{-(n+1)} P_n(\cos\theta), \quad (4.34)$$

and the following substitutions have been made:³

$$\begin{aligned}
 r &\rightarrow \rho = \sqrt{r_{cyl}^2 + (z_{cyl} - z_0)^2}, \\
 \theta &\rightarrow \arctan \frac{r_{cyl}}{(z_{cyl} - z_0)}, \\
 A_0 &\rightarrow 0, \\
 A_{n>0} &\rightarrow -\Psi_{n-1}^{cen}|_{z_0} \frac{1}{n+1} (\rho_{cen})^{-n}, \\
 B_0 &\rightarrow 0, \\
 B_{n>0} &\rightarrow \Psi_{n+1}^{rem}|_{z_0} \frac{1}{n+1} (\rho_{rem})^{n+2}.
 \end{aligned}$$

4.3.1 Regions of convergence

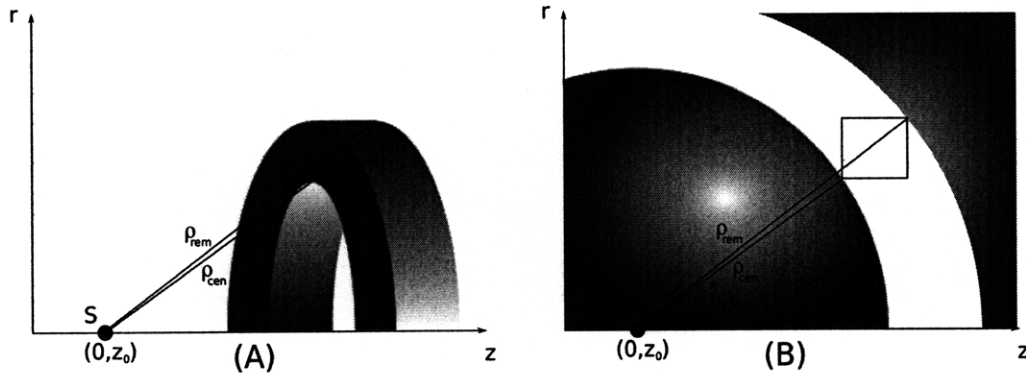


Figure 4-6: (A) A 3-dimensional rendering of an axially symmetric magnetic coil and (B) the regions of convergence for central and remote zonal harmonic expansion from a source point S .

Since equation 4.32 is only applicable in regions containing no current density, the Legendre polynomial expansion has restricted regions of convergence. It is once again convenient to describe the areas where the technique holds valid in terms of central and remote regions. The remote region is defined as a spherical shell whose outer radius extends to infinity, and whose inner radius is the distance between the source point to the farthest current (see Fig. 4-6), much like its electric counterpart. The

³In the central expansion, the zeroth term is a constant, and has no influence on the values of the magnetic field. In the remote expansion, the zeroth term is the magnetic monopole contribution, which can be omitted.

region of convergence for the central expansion is somewhat more subtle for magnetic fields, however, and must be described in the context of the geometry primitives that generate the field.

For the central expansion of the magnetic scalar potential, the radius of convergence extends from the source point to the closest region of current, as expected. However, since we are only interested in computing the magnetic field and not the scalar potential, we can extend our central radius of convergence for solenoids and for thick coils. For solenoids, Appendix B.2 describes how the magnetic field can be described in terms of the scalar potential for two rings located at the edges of the solenoid, thus extending the radius of convergence to be equivalent to a 2-ring configuration. By a similar argument, the central region of convergence for the magnetic field produced by a thick coil is determined by a 4-ring configuration, with two rings located at the outer and inner radii of each edge of the coil [53].

4.3.2 Derivation of magnetic field components from magnetic scalar potential

The derivation of the magnetic field components from equation 4.32 is achieved by once again employing the special properties of the derivatives of zonal harmonics (Eqns. 4.5, 4.6, 4.9, and 4.10) onto the central and remote definitions of the magnetic scalar potential (Eqns. 4.33 and 4.34). The results of these derivations are stated below:

Central expansion

The magnetic field in the central region is defined as

$$\begin{aligned}
 B_{z_{cyl}} &= -\frac{\partial}{\partial z_{cyl}} (\Psi_{cen}(r_{cyl}, z_{cyl})) = \\
 &= \sum_{n=0}^{\infty} \Psi_n^{cen}|_{z_0} \left(\frac{\rho}{\rho_{cen}} \right)^n P_n(\cos \theta)
 \end{aligned} \tag{4.35}$$

and

$$\begin{aligned}
B_{r_{cyl}} &= -\frac{\partial}{\partial r_{cyl}} (\Psi_{cen}(r_{cyl}, z_{cyl})) = \\
&= -\sin \theta \sum_{n=1}^{\infty} \Psi_n^{cen}|_{z_0} \left(\frac{1}{n+1} \right) \left(\frac{\rho}{\rho_{cen}} \right)^n P'_n(\cos \theta). \tag{4.36}
\end{aligned}$$

Remote expansion

The magnetic field in the remote region is defined as

$$\begin{aligned}
B_{z_{cyl}} &= -\frac{\partial}{\partial z_{cyl}} (\Psi_{rem}(r_{cyl}, z_{cyl})) = \\
&= \sum_{n=2}^{\infty} \Psi_n^{rem}|_{z_0} \left(\frac{\rho}{\rho_{rem}} \right)^{-(n+1)} P_n(\cos \theta) \tag{4.37}
\end{aligned}$$

and

$$\begin{aligned}
B_{r_{cyl}} &= -\frac{\partial}{\partial r_{cyl}} (\Psi_{rem}(r_{cyl}, z_{cyl})) = \\
&= \sum_{n=2}^{\infty} \Psi_n^{rem}|_{z_0} \frac{\sin \theta}{n} \left(\frac{\rho}{\rho_{rem}} \right)^{-(n+1)} P'_n(\cos \theta). \tag{4.38}
\end{aligned}$$

4.3.3 Calculating Source Constants

This section describes the computation of the source constants $\Psi_n^{cen}|_{z_0}$ and $\Psi_n^{rem}|_{z_0}$ for different geometrical primitives. Since the magnetic fields are more readily calculable than the scalar potential, it is convenient to utilize the methods of Garrett [49] and Glück [50] for determining the source constants from the fields. As with the electric source constants, the method is first demonstrated using a trivial geometry in order to describe the principles of implementation, followed by its application to more general geometrical configurations for practical use.

Central source constants for a current loop

Given a circular current loop with current I and radius R and centered at Z , we place a source point S on the z -axis at $(0, z_0)$ (see fig. 4-7). The method for computing the

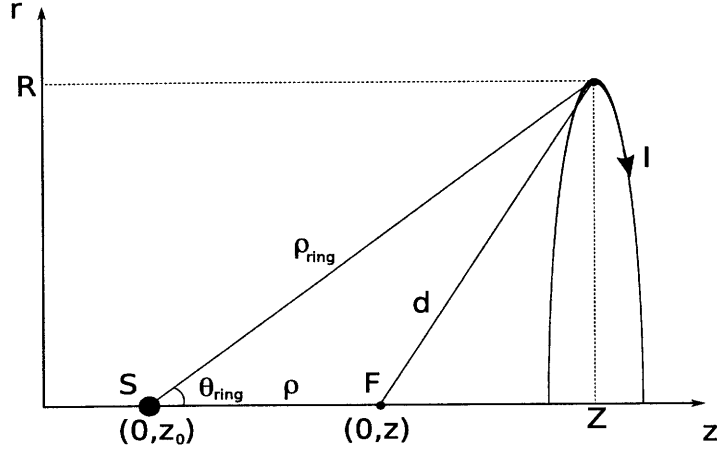


Figure 4-7: Graphical depiction of a current loop with generating point (R, Z) , a central source point (S) , and an arbitrary on-axis field point (F) .

source constants at S is similar to that of the charged ring (Sec. 4.2.3), with a few key changes: we compare the derived calculation of the z -component of the magnetic field with 4.35 at an arbitrary point F on the z -axis, since its computation is more straightforward than that of the magnetic scalar potential.

Symmetry arguments allow us to conclude *a priori* that $B_r = 0$ for all on-axis field points. Invoking the *Biot-Savart Law*[40][30], we can determine that the z -component of the magnetic field is

$$B_z(F) = \frac{\mu_0}{4\pi} I \int_0^{2\pi R} \frac{dl'}{d^2} \cos \theta_{ring} = \frac{\mu_0 I R^2}{2 d^3}. \quad (4.39)$$

As before, d is redefined in terms of $\rho = |z_0 - z|$ and $\rho_{ring} = \sqrt{(Z - z_0)^2 + R^2}$ to be Equation 4.14, and this is in turn converted into a Legendre polynomial expansion using $h_{cen} = \left(\frac{\rho}{\rho_{cen}}\right)$:

$$\frac{1}{d} = \frac{1}{\sqrt{\rho_{ring}^2 + \rho^2 - 2\rho_{ring}\rho \cos \theta_{ring}}} = \frac{1}{\rho_{ring}} \sum_{n=0}^{\infty} h_{cen}^n P_n(\cos \theta_{ring}). \quad (4.40)$$

Taking the derivative of $\frac{1}{d}$ with respect to $\cos \theta_{ring}$ yields

$$\begin{aligned} \frac{\partial}{\partial (\cos \theta_{ring})} \left(\frac{1}{d} \right) &= \frac{\rho_{ring} \cdot \rho}{(\rho_{ring}^2 + \rho^2 - 2\rho_{ring}\rho \cos \theta_{ring})^{\frac{3}{2}}} = \\ &= \frac{1}{\rho_{ring}} \sum_{n=0}^{\infty} h_{cen}^n P'_n(\cos \theta_{ring}). \end{aligned} \quad (4.41)$$

Further simplification of Equation 4.41 yields

$$\frac{1}{d^3} = \left(\frac{1}{\rho_{ring}} \right)^3 \sum_{n=0}^{\infty} h_{cen}^n P'_{n+1}(\cos \theta_{ring}). \quad (4.42)$$

Substituting Equation 4.42 into 4.39 and equating the result to our ansatz (Eq. 4.35), we get

$$\frac{\mu_0 I}{2} \frac{R^2}{\rho_{ring}^3} \sum_{n=0}^{\infty} \left(\frac{\rho}{\rho_{ring}} \right)^n P'_{n+1}(\cos \theta_{ring}) = \sum_{n=0}^{\infty} \Psi_n^{cen}|_{z_0} \left(\frac{\rho}{\rho_{cen}} \right)^n, \quad (4.43)$$

which can be algebraically manipulated to determine the value of the central source constants $\Psi_n^{cen}|_{z_0}$:

$$\Psi_n^{cen}|_{z_0} = \frac{\mu_0 I}{2} \cdot \frac{\sin^2 \theta_{ring}}{\rho_{cen}} \cdot \left(\frac{\rho_{cen}}{\rho_{ring}} \right)^{(n+1)} P'_{n+1}(\cos \theta_{ring}). \quad (4.44)$$

Remote source constants for a current loop

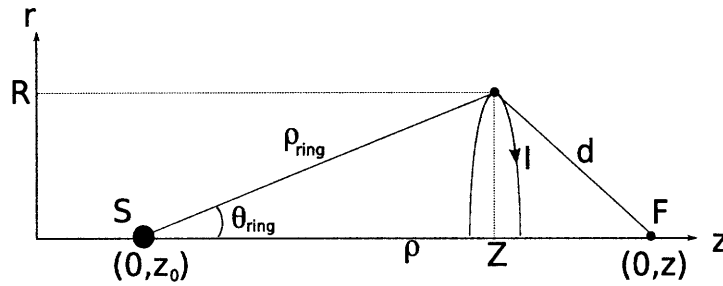


Figure 4-8: Graphical depiction of a current loop with generating point (R, Z) , a remote source point (S) , and an arbitrary on-axis field point (F) .

The derivation of the remote source constants for a current loop is similar to to

that of the central source constants for the same loop. Much like what was done for a charged ring, $h_{rem} = (\frac{\rho_{ring}}{\rho})$ is used to redefine d , the distance between the on-axis field point F and the ring. Taking the derivative of $\frac{1}{d}$ with respect to $\cos \theta_{ring}$ yields

$$\begin{aligned} \frac{\partial}{\partial (\cos \theta_{ring})} \left(\frac{1}{d} \right) &= \frac{\rho_{ring} \cdot \rho}{(\rho_{ring}^2 + \rho^2 - 2\rho_{ring}\rho \cos \theta_{ring})^{\frac{3}{2}}} = \\ &= \frac{1}{\rho} \sum_{n=0}^{\infty} h_{rem}^n P'_n(\cos \theta_{ring}). \end{aligned} \quad (4.45)$$

Simplifying Equation 4.45, we get

$$\frac{1}{d^3} = \left(\frac{1}{\rho_{ring}} \right)^3 \sum_{n=1}^{\infty} h_{rem}^{(n+2)} P'_n(\cos \theta_{ring}). \quad (4.46)$$

Inserting Equation 4.46 into 4.39 and equating it to our ansatz (Eq. 4.37), we get

$$\frac{\mu_0 I}{2} \cdot \frac{R^2}{\rho_{ring}^3} \cdot \sum_{n=2}^{\infty} h_{rem}^{(n+1)} P'_{n-1}(\cos \theta_{ring}) = \sum_{n=2}^{\infty} \Psi_n^{rem}|_{z_0} \left(\frac{\rho}{\rho_{rem}} \right)^{-(n+1)}, \quad (4.47)$$

which, when analyzed piecewise, produces the definition for the remote source constants for a current loop:

$$\Psi_n^{rem}|_{z_0} = \frac{\mu_0 I}{2} \cdot \frac{\sin^2 \theta_{ring}}{\rho_{rem}} \cdot \left(\frac{\rho_{ring}}{\rho_{rem}} \right)^n P'_{n-1}(\cos \theta_{ring}). \quad (4.48)$$

Source constants for an infinitely thin solenoid

Using the results derived in the previous section, it is possible to determine the source points from an infinitely thin solenoid (like the one described in Fig. 4-9) by analytically integrating Equations 4.44 and 4.48 over the length of the solenoid. For the central expansion coefficients, we begin with

$$\Psi_n^{cen}|_{z_0} = \frac{\mu_0 \cdot |\vec{k}|}{2} \int_{Z_a}^{Z_b} \frac{\sin^2(\theta(Z))}{\rho_{cen}} \left(\frac{\rho_{cen}}{\rho(Z)} \right)^{(n+1)} P'_{n+1}(\cos(\theta(Z))) \cdot dZ, \quad (4.49)$$

where

$$\rho(Z) = \sqrt{R^2 + (Z - z_0)^2} \quad (4.50)$$

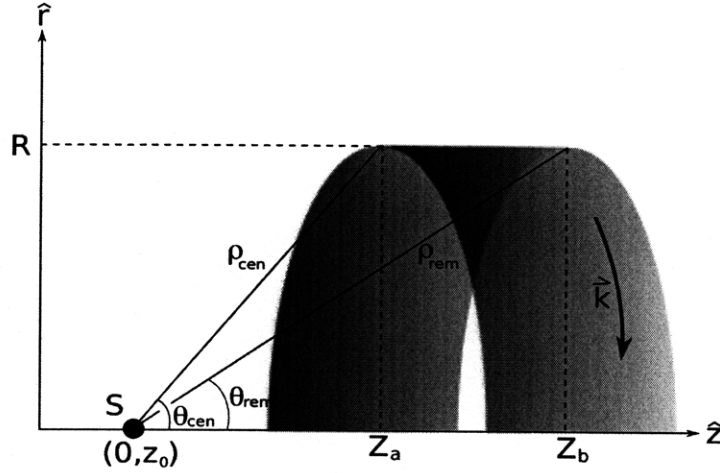


Figure 4-9: Graphical depiction of a solenoid generated by the line connecting (R, Z_a) and (R, Z_b) with surface current density \vec{k} , and a central source point (S) .

and

$$\theta(Z) = \arccos\left(\frac{Z - z_0}{\rho(Z)}\right) \quad (4.51)$$

for $Z_a \leq Z \leq Z_b$. We can use the recursive nature of the derivatives of the zonal harmonics to rewrite the integrand of Equation 4.49, which we label as

$$\psi_n^{cen}|_{z_0}(Z) = \frac{\sin^2(\theta(Z))}{\rho_{cen}} \left(\frac{\rho_{cen}}{\rho(Z)}\right)^{(n+1)} P'_{n+1}(\cos(\theta(Z))), \quad (4.52)$$

as follows: Using the property of the Legendre polynomials [49] that

$$\sin^2(\theta) \cdot P'_n(\cos(\theta)) = \frac{(-1)^{n-1}}{(n-1)!} \cdot \rho^n \cdot \frac{\partial^n \cos(\theta)}{\partial Z^n}, \quad (4.53)$$

Equation 4.52 becomes

$$\psi_n^{cen}|_{z_0}(Z) = (\rho_{cen})^n \cdot \frac{(-1)^n}{n!} \cdot \frac{\partial^{(n+1)} \cos(\theta(Z))}{\partial Z^{(n+1)}}. \quad (4.54)$$

Similarly, we can write $\psi_{n+1}^{cen}|_{z_0}$ as

$$\psi_{n+1}^{cen}|_{z_0}(Z) = (\rho_{cen})^{(n+1)} \cdot \frac{(-1)^{n+1}}{(n+1)!} \cdot \frac{\partial^{(n+2)} \cos(\theta(Z))}{\partial Z^{(n+2)}}. \quad (4.55)$$

Equation 4.55 can now be rewritten in terms of Equation 4.54 as

$$\psi_{n+1}^{cen}|_{z_0}(Z) = -\frac{\rho_{cen}}{(n+1)} \cdot \frac{\partial}{\partial Z} (\psi_n^{cen}|_{z_0}). \quad (4.56)$$

With this relation, performing the integration in Equation 4.52 for the case $n > 1$ becomes trivial:

$$\begin{aligned} \Psi_n^{cen}|_{z_0} &= \frac{\mu_0 \cdot |\vec{k}|}{2} \cdot \int_{Z_a}^{Z_b} \psi_n^{cen}|_{z_0} \cdot dZ = \\ &= \frac{\mu_0 \cdot |\vec{k}|}{2} \int_{Z_a}^{Z_b} dZ \cdot \left(-\frac{\rho_{cen}}{n}\right) \cdot \frac{\partial}{\partial Z} (\psi_{n-1}^{cen}|_{z_0}) = \\ &= -\frac{\mu_0 \cdot |\vec{k}|}{2} \cdot \frac{\rho_{cen}}{n} \cdot [\psi_{n-1}^{cen}|_{z_0}(Z_b) - \psi_{n-1}^{cen}|_{z_0}(Z_a)]. \end{aligned} \quad (4.57)$$

For $n = 0$, the Legendre polynomial term is equal to unity, and the integral can be performed in a straightforward manner to produce

$$\Psi_0^{cen}|_{z_0} = \frac{\mu_0 \cdot |\vec{k}|}{2} \left(\frac{(Z_b - z_0)}{\sqrt{R^2 + (Z_b - z_0)^2}} - \frac{(Z_a - z_0)}{\sqrt{R^2 + (Z_a - z_0)^2}} \right). \quad (4.58)$$

Similarly, to compute the remote source coefficients for the solenoid in Figure 4-9 we start with

$$\Psi_n^{rem}|_{z_0}(Z) = \frac{\mu_0 \cdot |\vec{k}|}{2} \int_{Z_a}^{Z_b} \frac{\sin^2(\theta(Z))}{\rho_{rem}} \left(\frac{\rho(Z)}{\rho_{rem}}\right)^n P'_{n-1}(\cos(\theta(Z))) \cdot dZ. \quad (4.59)$$

Once again, we label the integrand of Equation 4.59 as

$$\psi_n^{rem}|_{z_0}(Z) = \frac{\sin^2(\theta(Z))}{\rho_{rem}} \left(\frac{\rho(Z)}{\rho_{rem}}\right)^n P'_{n-1}(\cos(\theta(Z))). \quad (4.60)$$

Using the relation

$$\psi_n^{rem}|_{z_0}(Z) = \frac{\rho_{rem}}{n+1} \cdot \frac{\partial}{\partial Z} (\psi_{n+1}^{rem}|_{z_0}) \quad (4.61)$$

derived in Appendix B, Equation 4.59 becomes

$$\begin{aligned}
 \Psi_n^{rem}|_{z_0} &= \frac{\mu_0 \cdot |\vec{k}|}{2} \int_{Z_a}^{Z_b} \psi_n^{rem}|_{z_0} \cdot dZ = \\
 &= \frac{\mu_0 \cdot |\vec{k}|}{2} \int_{Z_a}^{Z_b} dZ \cdot \left(\frac{\rho_{rem}}{n+1} \right) \cdot \frac{\partial}{\partial Z} (\psi_{n+1}^{rem}|_{z_0}) = \\
 &= \frac{\mu_0 \cdot |\vec{k}|}{2} \cdot \frac{\rho_{rem}}{n+1} \cdot [\psi_{n+1}^{rem}|_{z_0}(Z_b) - \psi_{n+1}^{rem}|_{z_0}(Z_a)]. \quad (4.62)
 \end{aligned}$$

Source constants for a thick coil

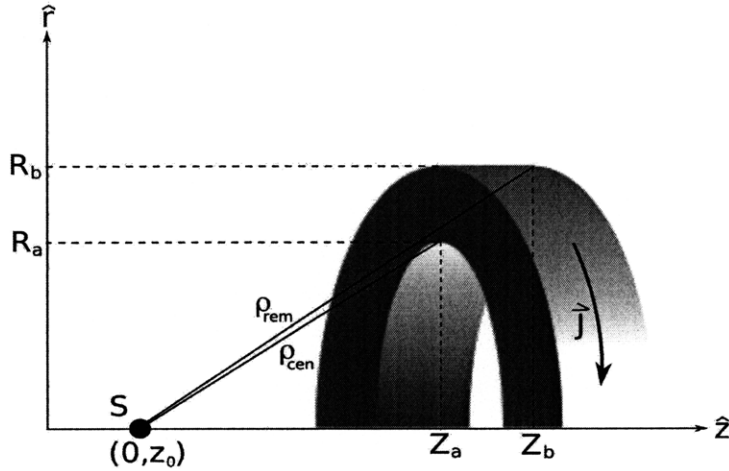


Figure 4-10: Graphical depiction of a thick coil generated by the rectangle with corners (R_a, Z_a) and (R_b, Z_b) with volume current density \vec{J} , and a central source point (S) .

In a similar fashion, we determine the source constants for a thick coil (such as the one depicted in Fig. 4-4) by using Equations 4.57 and 4.62 for an infinitely thin solenoid and integrating over the thickness of the coil $(R_b - R_a)$. For the central expansion, our source constants are defined as

$$\Psi_n^{cen}|_{z_0} = \frac{\mu_0 \cdot |\vec{J}|}{2} \cdot \int_{R_a}^{R_b} \tilde{\psi}_n^{cen}|_{z_0}(R) \cdot dR, \quad (4.63)$$

where

$$\tilde{\psi}_n^{cen}|_{z_0}(R) = \frac{\rho_{cen}}{n} \cdot [\psi_{n-1}^{cen}|_{z_0}(Z_b) - \psi_{n-1}^{cen}|_{z_0}(Z_a)], \quad (4.64)$$

and $\psi_n^{cen}|_{z_0}(Z)$ is defined in Equation 4.52 with implicit dependencies upon R . The remote source constants are defined as

$$\Psi_n^{rem}|_{z_0} = \frac{\mu_0 \cdot |\vec{J}|}{2} \cdot \int_{R_a}^{R_b} \tilde{\psi}_n^{rem}|_{z_0}(R) \cdot dR, \quad (4.65)$$

where

$$\tilde{\psi}_n^{rem}|_{z_0}(R) = \frac{\rho_{rem}}{n+1} \cdot [\psi_{n+1}^{rem}|_{z_0}(Z_b) - \psi_{n+1}^{rem}|_{z_0}(Z_a)], \quad (4.66)$$

and $\psi_n^{rem}|_{z_0}(Z)$ is defined in Equation 4.60, once again with implicit dependencies upon R . The integrals described in Equations 4.63 and 4.65 can be computed using numerical integration techniques.

4.4 Summary

The method of zonal harmonic expansion facilitates the fast computation of axially symmetric electric and magnetic fields within the central and remote regions of convergence, with the speed of computation proportional to the distance between the field point and the nearest geometry primitive. Methods of computing the source points for various axially symmetric geometry primitives have been described, facilitating the computation of electric and magnetic fields from relatively complex geometry configurations comprised of these primitives. When the assumption of axial symmetry is valid and field points are sufficiently far from the geometry primitives, the method of zonal harmonics is the most effective technique for fast and accurate field computation.

Chapter 5

Field Interpolation with an Adaptive Refinement Field Map

5.1 Introduction

5.1.1 Features of current routines

The techniques of elliptic integral computation and zonal harmonic expansion described in Chapters 3 and 4, respectively, are applicable to the computation of both electric and magnetic fields. In theory, a combination of the two methods adequately constitutes a complete time-independent electromagnetic simulation package on its own. For practical use, however, it is important to understand the specific circumstances to which each of these methods are suited and, more importantly, to identify the situations that highlight their shortcomings.

The method of zonal harmonic expansion described in Chapter 4 provides for fast and accurate electric field calculations in regions far from geometry primitives, where the expansion converges quickly. It is limited to axially symmetric geometries, however, and cannot be used in regions close to electrode surfaces. The elliptic integral method of calculation, described in Chapter 3, is applicable in all space (and indeed is necessary for the computation of the charge densities of each of the electrode sub-elements, an essential step for both the elliptic field calculation and

the zonal harmonic expansion). The amount of time necessary to perform elliptic integrals over each sub-element is rather large, unfortunately, and the computation time for a single field point quickly becomes unwieldy when a geometry configuration has many sub-elements.

For many simulations, the shortcomings of these two methods do not play a large role. For example, a simulation of electron transport through nearly the entirety of KATRIN (with axially symmetric approximations for the pre- and main-spectrometer) is deftly handled by continuous use of zonal harmonic expansions, and the elliptic integral method may only need to be used sporadically. In this situation, it is clear that all of the necessary tools for performing a fast and accurate simulation are already constructed.

There are many instances, however, where these limitations cause the aforementioned techniques to be difficult, if not impossible, to implement practically. Examples where this is the case are studies of radiation from the electrodes, simulations of calibration via an electron gun, and precision calculations where axial symmetry approximations can no longer be made. Ways around these limitations include using more powerful tools for computation, and different techniques for field computation, such as field mapping.

5.1.2 General features of a field map

The basic idea behind implementing a field map is quite simple: a grid is placed on the region where computation is desired, the function is computed at the nodes of the grid and saved to file. Once the grid and field values are determined, an interpolating function is used to approximate the function value within the grid using the predetermined field values at the nodes of the grid. Since field maps have become a standard technique in computational analysis, it suffices to curtail any further description of their general attributes; the reader is encouraged to see [54] and other numerical analysis texts for more details. Instead, it is important to focus on the features of field maps relative to the methods of elliptic integral calculation and zonal harmonic expansion.

Since a field map can be implemented in any region where the interpolated function is valid, and since the electric and magnetic fields can be computed in all space using elliptic integral calculations, a field map theoretically has no restrictions on its regions of use. However, practical application places limitations on the size of the map. The time it takes to generate a field map and the speed of traversing its nodes are both proportional to the size of the map, naturally favoring smaller maps for faster generation and implementation. Table 5.1 relates these general properties of a field map to the comparative features of the other two methods.

Method	Regions of applicability	Dimension	Computation time dependency	Relative speed of computation
Elliptic Integrals	all space	2, 3	# of sub-elements	slow
Zonal Harmonic	away from geometry	2	distance from geometry	fastest
Field Map	all space	2, 3	size of map	faster

Table 5.1: Features of field computation methods (assuming that the desired accuracy from each method is equivalent)

Fortunately, the features (both positive and negative) of a field map correspond well with those of the method of zonal harmonic expansion. Where the zonal harmonic expansion method can cover most of space (with use of multiple source points) with relatively fast computation times, the regions where it fails can be covered by a field map, thereby eliminating the necessity (and time) of repeated elliptic integral computations. It is still possible to use a field map for geometries that do not possess axial symmetry, but for large regions of computation a field map may become impractical and another form of calculation may be needed.

5.2 Interpolation technique

5.2.1 Reduced multivariate Hermite interpolation

The interpolation method employed in `KatrinField` is a variant of a fourth order reduced multivariate Hermite interpolation technique [44]. Similar methods may be

found in [55], [56] and [57]. During the construction of the map, a d -dimensional grid of nodes is placed over the region of interest, and at each node the field value and its d gradient components are computed and stored¹. Once the grid is in place, a field point within the grid is computed as follows: first, a d -dimensional box with 2^d nodes as its vertices is formed to encompass the field point. The coordinates of the field point are then rescaled to a local frame, where the box is centered at the origin and the lengths of the sides of the box are all $2 \times$ unity (see Fig. 5-1). The function is then approximated using third order polynomials, constructed to match the $(d + 1) \times 2^d$ boundary conditions ($(d + 1)$ values per node $\times 2^d$ nodes).

5.2.2 Features of the interpolator

Compared to other methods, the Hermite interpolation method possesses two key features. Since only the 2^d nodes that form the surrounding box are used for a single computation, the method facilitates the organization of the nodes into boxes. This is useful for constructing node traversal algorithms, and it also sidesteps the issues involving hanging nodes [58] and neighbor-finding techniques [59] present in many other interpolation methods. Also, because the method only uses the function value and its first partial derivatives (as opposed to mixed partials), inaccuracies resulting from repeated numerical differentiation are avoided and fewer terms are required within the interpolation (in contrast to the method introduced in [60], for example).

5.2.3 Derivation of the interpolator in d dimensions

We now follow the derivation for the Hermite interpolating function from the 2^d nodes, each containing $(d+1)$ parameters, originally determined by Glück [44]. We shall label the function whose values we are trying to interpolate as $F(\vec{p})$, and the interpolating function $G(\vec{p})$, where \vec{p} represents the point in space where the field value is to be determined. The interpolating box is defined to be centered at the origin, with sides

¹For our purposes, the dimensionality d is either 2 (for axially symmetric systems) or 3.

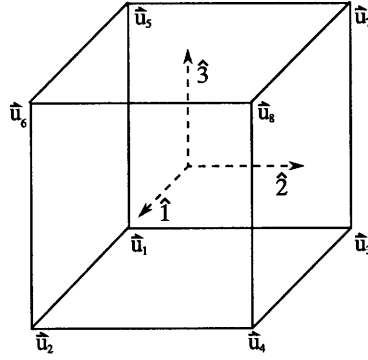


Figure 5-1: For $d = 3$, a cube centered at the origin with sides of length 2 used for interpolation. Axes are labeled as \hat{i} , $i = 1, 2, 3$. Vertices are labeled as \vec{u}_j , $j = 1, 2, \dots, 8$.

of length $2 \times$ the unit length (see Fig. 5-1). We define as our ansatz

$$G(\vec{p}) = \sum_{i=1}^{2^d} \sum_{j=0}^d g_{ij} \Phi_{ij}(\vec{p}), \quad (5.1)$$

where

$$g_{ij} = \begin{cases} F(\vec{u}_i) & j = 0 \\ \left. \frac{\partial F(\vec{p})}{\partial \hat{j}} \right|_{\vec{p}=\vec{u}_i} & j = 1, \dots, d \end{cases} \quad (5.2)$$

and \vec{u}_i represents the position of the i -th vertex of the cube in d -space, and $\Phi_{ij}(\vec{p})$ is a scalar function. Our task is to determine a form for $\Phi_{ij}(\vec{p})$ that satisfies the $(d+1) \times 2^d$ boundary conditions of the cube.

We begin by proposing an ansatz for $\Phi_{ij}(\vec{p})$:

$$\Phi_{ij}(\vec{p}) = u_{ij} \prod_{k=1}^d \phi_{jk}(t), \quad (5.3)$$

where

$$u_{ij} = \begin{cases} 1 & j = 0 \\ \vec{u}_i \cdot \hat{j} = (\vec{u}_i)_j & j = 1, \dots, d \end{cases}$$

and

$$t = (\vec{u}_i)_k (\vec{p})_k.$$

Enforcing the condition that the interpolated function equal the original function at the vertices ($G(\vec{u}_n) = g_{n0}$, $n = \{1, 2, \dots, 2^d\}$), we are immediately able to determine that $\Phi_{ij}(\vec{u}_n) = \delta_{in}\delta_{j0}$. Applying this restriction to Equation 5.3 gives us the following relation:

$$\Phi_{ij}(\vec{u}_n) = u_{ij} \prod_{k=1}^d \phi_{jk}((\vec{u}_i)_k (\vec{u}_n)_k) = \delta_{in}\delta_{j0}. \quad (5.4)$$

If the vectors \vec{u}_i and \vec{u}_n describe different vertices of the cube ($i \neq n$), then for at least one $k = k'$ the term in the product of Equation 5.4 will be $\phi_{jk'}(-1)$.² Similarly, if \vec{u}_i and \vec{u}_n describe the same vertex of the cube ($i = n$), Equation 5.4 becomes

$$u_{ij} \prod_{k=1}^d \phi_{jk}(1) = \delta_{j0}. \quad (5.5)$$

The δ_{in} term on the right side of equation 5.4 can therefore be enforced by requiring

$$\phi_{jk}(-1) = 0 \forall j, k, \quad (5.6)$$

while, since $k > 0$, the δ_{j0} term can be enforced by requiring that

$$\phi_{jk}(1) = 1 - \delta_{jk}. \quad (5.7)$$

These two requirements describe the boundary conditions on $\phi_{jk}(t)$ that require the interpolated function value to be exact at the 2^d vertices of the box.

Next, we require that the directional derivatives of the interpolated function be

²Since the cube is centered at the origin with sides of $2 \times$ unit length, the components of the vectors describing the vertices will be of the form $(\vec{u}_i)_k = \pm 1$. When computing $t = (\vec{u}_i)_k (\vec{u}_n)_k$, it becomes clear that, if $i \neq n$, one of the d components of \vec{u}_i and \vec{u}_n must differ, whereas if $i = n$, t will equal $(\pm 1)^2 = 1$.

exact at the vertices as well. That is, we require that

$$\partial_l(G(\vec{p}))|_{\vec{p}=\vec{u}_n} = \sum_{i=1}^{2^d} \sum_{j=0}^d g_{ij} \partial_l(\Phi_{ij}(\vec{p}))|_{\vec{p}=\vec{u}_n} = g_{nl}. \quad (5.8)$$

Applying this restriction to Equation 5.3 gives us

$$\partial_l(\Phi_{ij}(\vec{p}))|_{\vec{p}=\vec{u}_n} = \partial_l \left(u_{ij} \prod_{k=1}^d \phi_{jk}((\vec{u}_i)_k(\vec{p})_k) \right) |_{\vec{p}=\vec{u}_n} = \delta_{in} \delta_{jl}. \quad (5.9)$$

Taking the partial derivative of Equation 5.3 with respect to \hat{l} , we get

$$\partial_l(\Phi_{ij}(\vec{p})) = u_{ij} \cdot (\vec{u}_i)_l \cdot \phi'_{jl}((\vec{u}_i)_l(\vec{p})_l) \cdot \prod_{k=1, k \neq l}^d \phi_{jk}((\vec{u}_i)_k(\vec{p})_k). \quad (5.10)$$

Applying Equation 5.10 to Equation 5.9 in the case where $l = 1$, we obtain the following condition:

$$u_{ij} \cdot u_{i1} \cdot (\phi'_{j1}(u_{i1}u_{n1})) \cdot (\dots) \cdot (\phi_{jd}(u_{id}u_{nd})) = \delta_{in} \delta_{j1}. \quad (5.11)$$

We can see from Equation 5.11 that, if $i \neq n$, there exists a k' such that either $\phi'_{j(k'=1)}$ or $\phi_{j(k' \neq 1)}$ takes -1 as its argument. We can therefore satisfy the δ_{in} term on the right side of the equation by requiring that $\phi'_{jk}(-1) = 0 \forall j, k$.³

Similarly, if $i = n$ both $\phi'_{j(k'=1)}$ and the $\phi_{j(k' \neq 1)}$ terms take 1 as their argument. We can enforce the δ_{jl} term on the right side of equation 5.11 by requiring that $\phi'_{jk}(1) = \delta_{jk}$.⁴

³This requirement is sufficient, since it is already required that $\phi_{jk}(-1) = 0 \forall j, k$.

⁴Requiring that $\phi'_{jk}(1) = \delta_{jk}$ ensures that the prefactors $u_{ij} \cdot u_{il} = 1$, since $(u_{ij})^2 = 1 \forall i, j$.

We now have the following boundary conditions for $\phi_{jk}(t)$:

$$\phi_{jk}(-1) = 0 \tag{5.12}$$

$$\phi_{jk}(+1) = 1 - \delta_{jk} \tag{5.13}$$

$$\phi'_{jk}(-1) = 0 \tag{5.14}$$

$$\phi'_{jk}(+1) = \delta_{jk} \tag{5.15}$$

Next, we let ϕ_{jk} be a cubic interpolant of the following form:

$$\phi_{jk}(t) = f_1(t) + f_2(t)\delta_{jk}, \tag{5.16}$$

where

$$f_1(t) = c_1t^3 + c_2t^2 + c_3t + c_4 \tag{5.17}$$

and

$$f_2(t) = e_1t^3 + e_2t^2 + e_3t + e_4, \tag{5.18}$$

and c_i and e_i are constants. Solving the related linear algebraic equations, we get the following equation:

$$\phi_{jk}(t) = \frac{1}{4} \left((-t^3 + 3t + 2) + (2t^3 + t^2 - 4t - 3)\delta_{jk} \right). \tag{5.19}$$

Though the final equation is too cumbersome for print in a single equation, it is clear that Equations 5.1, 5.3 and 5.19 constitute the interpolating function we set out to find.

5.3 Adaptive-Refinement Field Map

5.3.1 General technique

The two main issues for computing a field map are finding a quick and accurate interpolating function (see Sec. 5.2), and striking a balance between node density

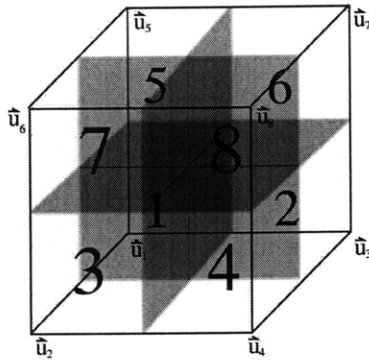


Figure 5-2: For $d = 3$, a depiction of a parent cube and its 8 subcubes.

and accuracy. A field with too many nodes will invariably produce a large file and be computationally expensive to navigate, while a field with too few nodes will lack sufficient information to perform accurate interpolations, resulting in a decrease in overall accuracy. For the latter issue, we use an adaptive-refinement field map [58].

To construct an adaptive-refinement field map, a uniform grid is created that covers the region of interest. Then, the interpolated field value is compared against the actual field value for each of the boxes in the grid. In regions where the error of the interpolated value exceeds a predefined limit, the box is further subdivided into smaller boxes (see Fig. 5-2). For the sake of discussion, the original box is referred to as a *parent box*, while boxes that result from the subdivision are referred to as *children boxes*. The process of subdivision continues until the error across the entire map is uniformly less than the given limit.

5.3.2 Quad-trees and oct-trees

The method of adaptive-refinement lends itself naturally to the use of quad-trees and oct-trees for 2 and 3 dimensions, respectively (see Fig. 5-3) [59]. This form of management is achieved by saving within each box information about its parent and children boxes. The search for the appropriate box for interpolating a given field

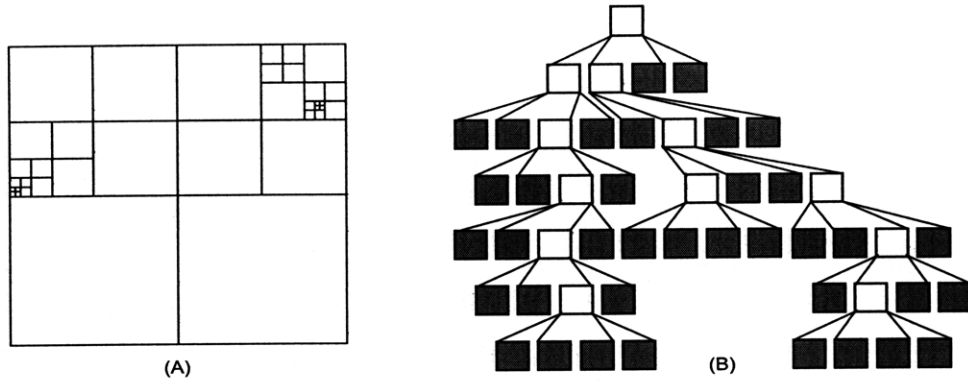


Figure 5-3: For $d = 2$, (A) an example of an adaptive refinement field mesh and (B) its corresponding quad-tree. In (B), Shaded regions represent boxes where the error of interpolation is acceptable for computation, and white regions represent boxes that required further splitting. Though only the shaded boxes are used for field computation (assuring a uniform maximal error), the white boxes are kept in the tree to facilitate the searching process.

point is then accomplished by traversing the tree from parent box to children boxes, hereafter referred to as a top-down search. According to [61], searches performed in this manner have an average time cost of $\sim \frac{2}{d} \cdot \log n$, where d is the dimensionality (as before), and n represents the number of boxes in the tree. In comparison, the average time cost for a sequential search is $\sim \frac{2^d - 1}{2^{(d+1)}} \cdot n$, which clearly proves more costly for large n .⁵ Similarly, tree navigation can occur in a bottom-up search, where each parent box is tested until a parent box is found to contain the field point. By using both top-down and bottom-up searches in tandem, the time cost of repeatedly navigating the field map can be even further reduced.

5.3.3 Constructing the field map

Two methods for constructing an adaptive-refinement field map are to either sequentially construct each branch of the tree, or to sequentially construct each level of boxes. The method described in this section is an amalgam of the two. At the highest level, each box in the grid (hereafter referred to as a *meta-box*) has its own “branch” of

⁵The time cost $\frac{2^d - 1}{2^{(d+1)}} \cdot n$ is obtained by first noting that, for a sequential search, only $\frac{2^d - 1}{2^d}$ of the boxes in the tree are used in computation. Of these, $\sim \frac{1}{2}$ must be traversed for each search.

the field map (which is a quad or oct-tree), and these are built sequentially. The construction of the trees in each meta-box, however, is performed one level at a time.

While the sequential creation of each meta-box is self-explanatory, the level-by-level process of constructing the trees in each meta-box is best explained by the following pseudocode:

```

1: construct the first box, and assign its children as the next  $2^d$  boxes in the array
2: define integers  $firstBox = 0$ ,  $lastBox = 0$ ,  $nBoxes = 1$ 
3: for  $n = 0$  to  $nLevel$  do {loop over the levels of the tree}
4:    $firstBox \leftarrow lastBox$ ,  $lastBox \leftarrow nBoxes$ 
5:   for  $i = firstBox$  to  $lastBox$  do {loop over the # of boxes in level  $n$ }
6:     if box  $i$  must be subdivided then
7:       for  $j = 0$  to  $2^d$  do
8:         construct child box  $j$ , assign its parent as  $i$ , and compute its field points
9:         if box  $j$  must be subdivided and  $(n + 1) \neq$  last level in the tree then
10:          assign box  $j$ 's children as  $nBoxes$  to  $nBoxes + 2^d$ 
11:           $nBoxes \leftarrow nBoxes + 2^d$ 
12:        else
13:          assign box  $j$ 's children as  $-1$  {null parameter indicating no children}
14:        end if
15:        add box  $j$  to the array of boxes
16:      end for
17:    end if
18:  end for
19: end for

```

There are several reasons for this method of construction: by having each meta-box contain its own individual tree, we are able to save a large map over multiple files with logical divisions in file management. Meanwhile, by creating each individual file using the level-by-level approach, each tree naturally acquires a logical organizational structure, and each box must be saved only once (once its parameters are stored, they are not changed). A one-time instantiation of the boxes works well with many

optimized tree-creating algorithms, where rapid access is favored over ease of creation.

5.4 Summary

The methods of an adaptive-refinement field map and a multivariate Hermite interpolator complement the existing methods of direct field calculation (Chapter 3) and zonal harmonic expansion (Chapter 4) well, providing for an efficient means to compute fields in regions that are frequently traversed and would otherwise have slow computation times. Admittedly, the field map technique lacks both the elegance and physically intuitive nature of the previous two methods, favoring instead a brute-force means of computation. However, since access to large computer clusters is becoming more common, techniques that require massive computational power are now much more practical for application.

Chapter 6

Validation

6.1 Introduction

In order to confirm that the field solving methods are producing sensible results and to understand the sources and magnitude of error implicit within the methods, it is essential to perform tests to validate the routines. This chapter describes various tests designed to both validate the methods described in this thesis as they are implemented in `KatrinField`, and to quantify the accuracies achieved using these methods. The tests cover all three field calculating methods for various geometry primitives.

6.2 BEM and direct calculation tests

Since the self-capacitance of an electrode is determined by the ratio of the electrode's net charge to its potential, a numerical measurement of the capacitance requires use of the BEM to determine the charge distribution on an electrode, and the direct calculation method compute the potential due to the computed charge distribution. By selecting simple geometries whose capacitances are either analytically soluble or known to high precision, it is possible to obtain concrete comparisons between the computed capacitances and their accepted values. As a result, the numerical measurement of an electrode's self-capacitance provides insight into the accuracy of both of these techniques.

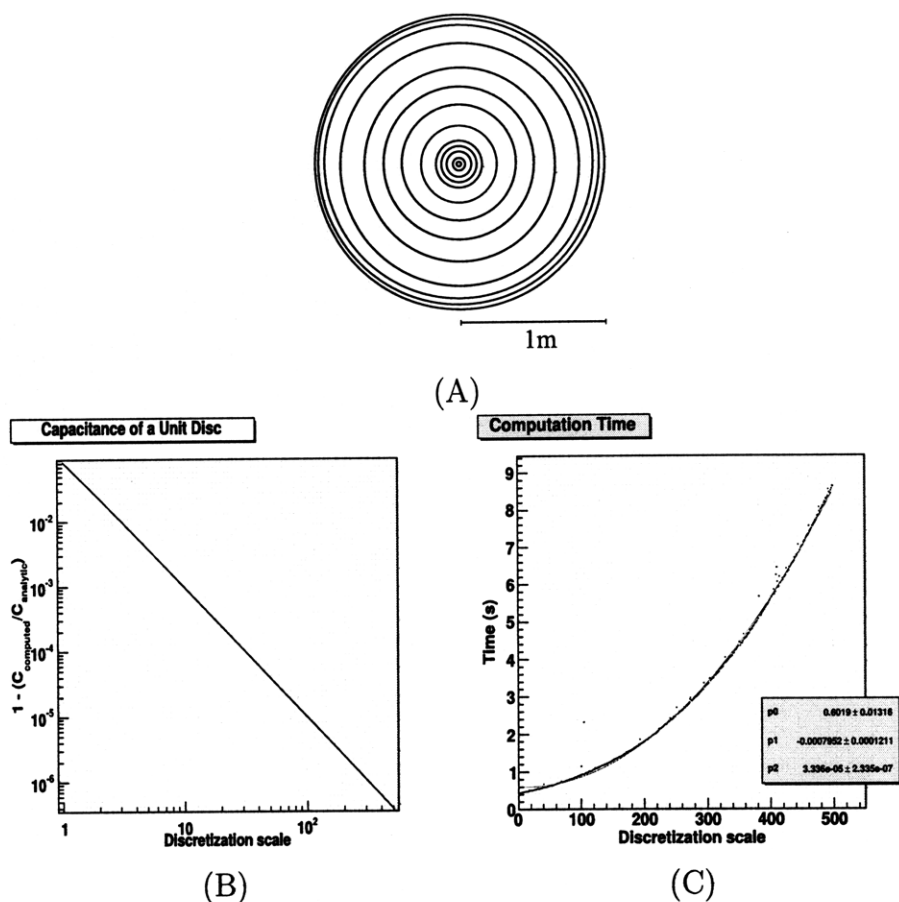
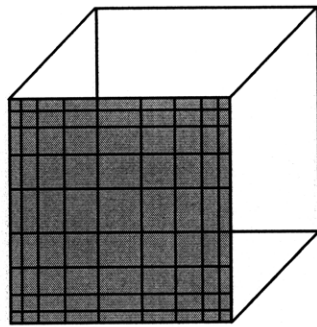


Table 6.1: (A) Measurement of the capacitance of a unit disc by discretizing the disc into concentric circles with decreasing thicknesses at the edge and center. (B) Comparative accuracy of the computed capacitance and (C) the time of computation with respect to the number of circular sub-elements.

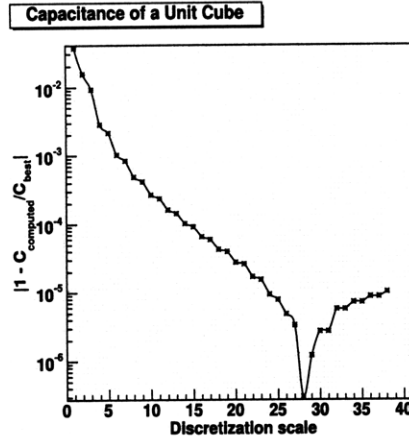
The first validation test performed compares the numerical capacitance $C_{computed}$ of a unit disc (see Table 6.1 (A)) to the analytic value $C_{analytic} = 8\pi\epsilon_0$ [62]. As can be seen in Table 6.1 (B), the computed capacitance of the unit disc inversely proportional to the number of discretized sub-elements used to perform the computation. As expected, Table 6.1 (C) shows a quadratic relationship between the number of sub-elements and the computation time, as the process of solving the linear algebraic Equation 3.29 scales with the square of the number of sub-elements.

The next validation test compares the numerical capacitance of a unit cube (see Table 6.2 (A)) to the value $C_{best} = 0.6606782 \pm 1 \times 10^{-7}$, computed in [63].¹ The

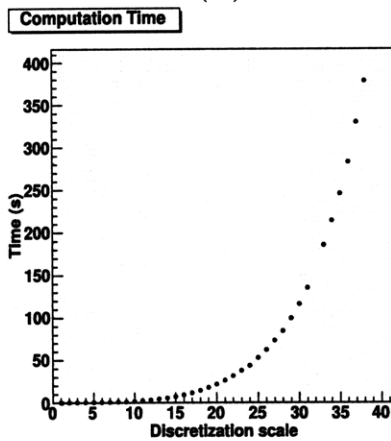
¹This test is modified from a test originally performed by Dr. Ferenc Glück [44].



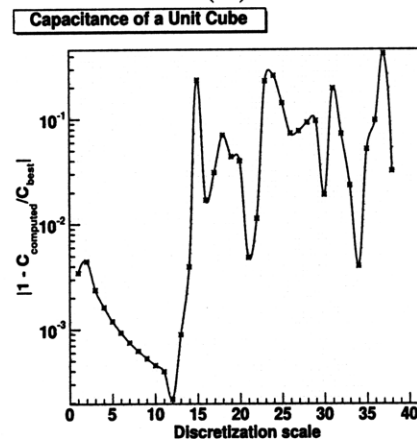
(A)



(B)



(C)



(D)

Table 6.2: (A) Measurement of the capacitance of a unit cube by discretizing the cube faces into rectangles with decreasing areas at the edges. (B) Comparative accuracy of the computed capacitance and (C) the time of computation with respect to the number of rectangle sub-elements. (D) Same test as performed in (B), but with each rectangle split into two right triangles.

computation was performed first using rectangles (see Table 6.2 (B)), and then using triangles (see Table 6.2 (D)). The capacitance measurements for both rectangular and triangular sub-elements both initially converge upon the expected value. Further tests are being performed in order to explain the sudden divergences from the true value in both plots, though preliminary analysis indicates that the divergences may be due to compounding errors from the potential calculation of each sub-element. In its current form, however, it appears that rectangular sub-elements achieve a sufficiently stable accuracy for use in field calculation.

Finally, the last validation test for the direct calculation method compares electric

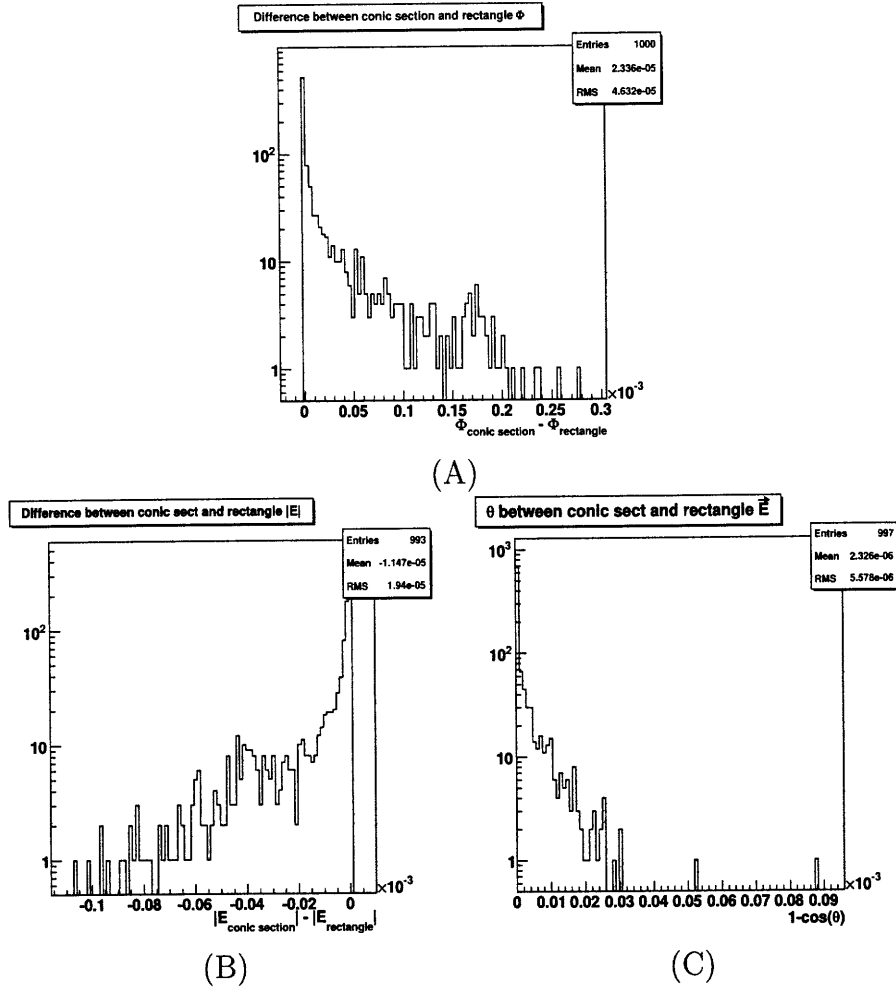


Table 6.3: A comparison of the direct computation method for a cylinder described by conic sections and by rectangles. Figure (A): The difference between the electric potential values for the two geometries. Figure (B): The difference between the magnitude of the computed \vec{E} -field values for the two geometries. Figure (C): The angle θ between the computed \vec{E} -field vectors for the two geometries.

field and potential at randomly selected points due to a cylinder held at unit potential. The cylinder is constructed first using conic sections, and then with multiply repeated rectangles.² Using the two different representations of the same geometry, electric field values at 1000 points are computed, and the difference between the potential and magnitude of the \vec{E} -field, as well as the cosine of the angle between the \vec{E} -field vectors, are placed into histograms. The results of this test are displayed in Table 6.3, and demonstrate an agreement between the two geometrical configurations to $\sim 10^{-5}$.

²This test is modified from a test originally performed by Dr. Ferenc Glück [44].

6.3 Comparison between direct calculation and zonal harmonic methods

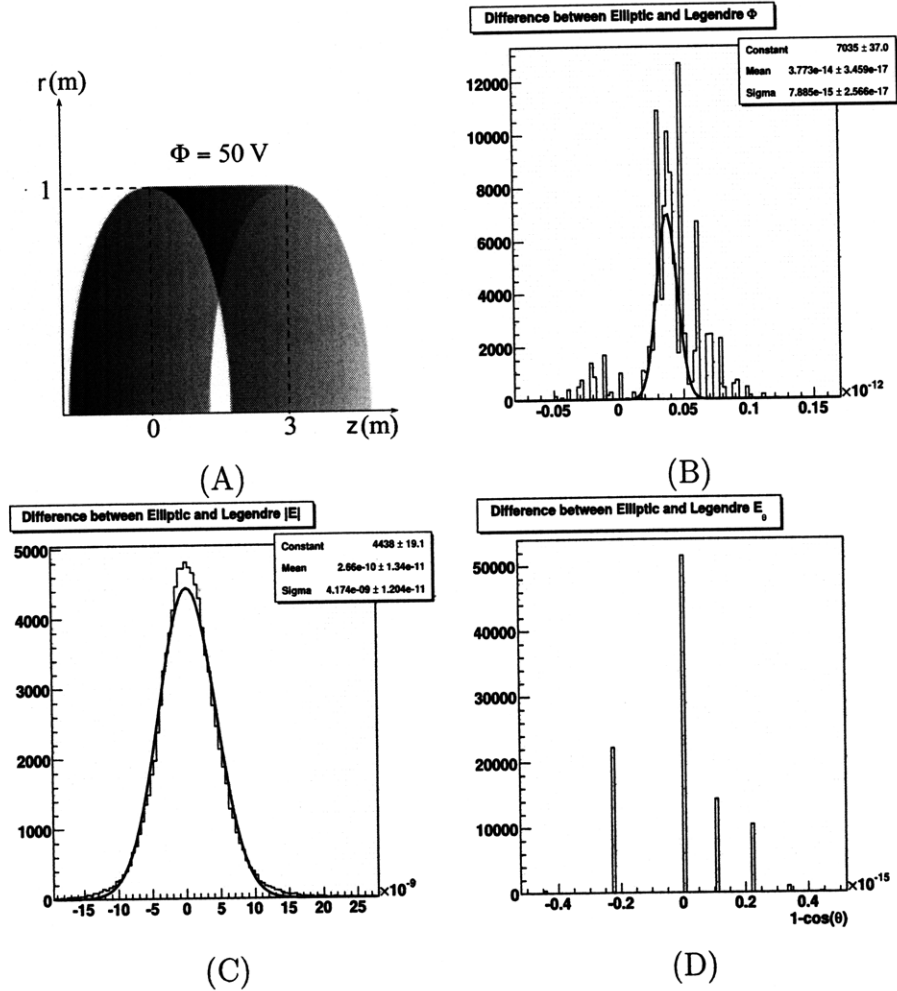
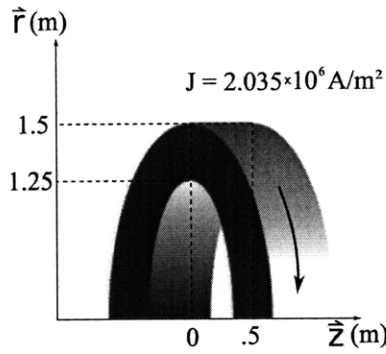
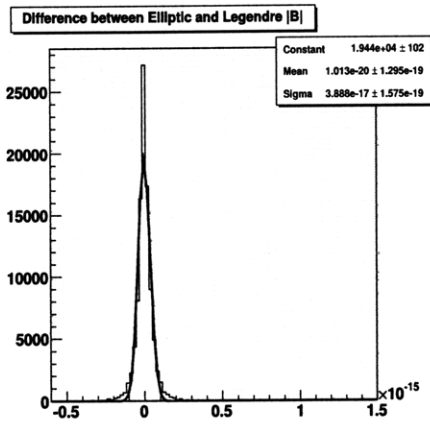


Table 6.4: Figure (A): Comparison of the direct and zonal harmonic field computation techniques for a cylinder electrode. Figure (B): The difference between the two methods' values for computing the electric potential. Figure (C): The difference between the magnitude of the \vec{E} -field computed by the two methods. Figure (D): The angle θ between the two \vec{E} -field vectors computed by the two methods.

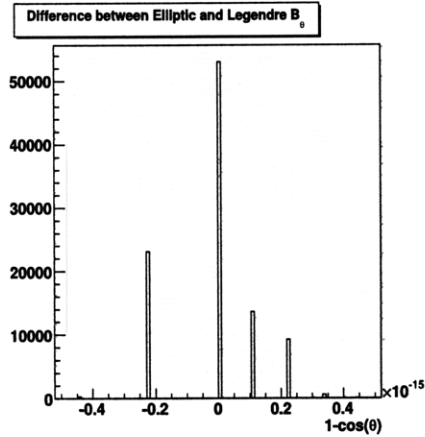
The validation tests in this section are designed to compare the zonal harmonic methods (where the field values are computed via Legendre polynomial expansion) for electric potential and electric and magnetic fields to the direct calculation methods (where the field values are computed from the charges and currents directly). For the electric potential and electric fields, a cylinder is used with dimensions defined



(A)



(B)



(C)

Table 6.5: Figure (A): Comparison of the direct and zonal harmonic field computation techniques for a thick coil magnet. Figure (B): The difference between the magnitude of the \vec{B} -field computed by the two methods. Figure (C): The angle θ between the two \vec{B} -field vectors computed by the two methods.

in Table 6.4 (A), and 10^5 points are chosen at random from both inside and outside the cylinder. From Table 6.4 (B), it can be seen that the the electric potential values computed by the two methods are accurate to nearly machine accuracy ($\sim 10^{-16}$). Since the direct computation method utilizes numerical differentiation to compute the electric fields, however, the magnitude of the electric fields as computed by both methods is only accurate to $\sim 10^{-9}$ (see Table 6.4 (C)). This demonstrates the inherent inaccuracy of the numerical differentiation technique, so chosen to balance accuracy and computation speed. From Table 6.4 (D) it can be seen that the angle θ between the electric field vectors for both methods is accurate to machine accuracy, resulting in stratified binning.

Similarly, the magnetic field tests are performed using a single thick coil with dimensions defined in Table 6.5 (A), with 10^5 points chosen at random both inside and outside of the coil. As can be seen from Table 6.5 (B) and (C), both the magnitude and angle between the magnetic fields are accurate to machine accuracy. It is unsurprising that the magnetic field values are more accurate than those for the electric field, since there is no accuracy loss resulting from the BEM and numerical differentiation techniques.

6.4 Field map tests

While the use of field maps are fully implemented in `KatrinField`, the construction of a field map that would produce competitive field values to the direct and zonal harmonic methods requires computation on a dedicated grid. Currently, `KatrinField` is designed to accomplish this very task by using MPI (Message Passing Interface) protocols [64]. These routines are currently in testing, but have not yet reached completion.

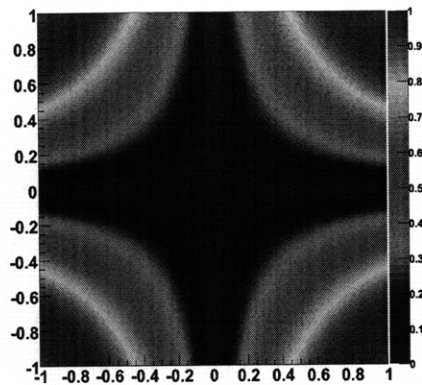
In order to demonstrate the functionality of the field map routines, a test program has been constructed that reproduces the values of a 2-dimensional function $F(x, y)$,

$$F(x, y) = \sin(2 \cdot x \cdot y). \quad (6.1)$$

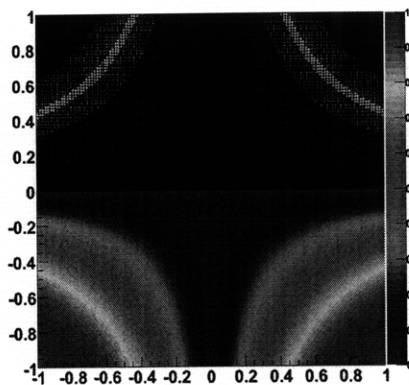
The field map created has a tolerance of 10^{-6} , and has 8 levels of cube splitting. As can be seen in Table 6.6, the desired minimum accuracy is achieved across the map.

6.5 Summary

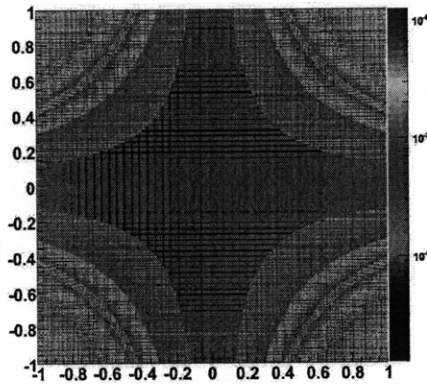
The validation tests described in this chapter demonstrate the basic functionality of the BEM method of charge computation and the direct, zonal harmonic and field map methods of field calculation. In addition, the tests expose the intrinsic errors associated with each method, providing for a general understanding of the accuracy of the field calculation program `KatrinField` as a whole. With these tests in mind, a



(A)



(B)



(C)

Table 6.6: A 2-dimensional field map, with tolerance 10^{-6} and 8 levels of cube splitting, of a sample function. Figure (A): an image of the original function. Figure (B): the original function with an overlay of the field map cubes. Figure (C): an image of the difference between the original and interpolated field values.

user is able to better understand the application of the components of `KatrinField`, and how to apply each method to maximize the utility of the program.

Chapter 7

Conclusion

Simulation of the electromagnetic design is vital for nearly every phase of the KATRIN experiment. In this thesis, pre-existing and new methods for fast and accurate field calculation were introduced within a unified object-oriented framework for use by the KATRIN collaboration for determining design specifications, quantifying background signals and simulating particle transport.

BEM techniques have been described and demonstrated for use in for computing charge densities on electrode surfaces. By discretizing electrode surfaces into sub-elements for which an analytic solution for the electric potential exists, it has been shown that the electric field due to an arbitrary electrode configuration can be computed in all regions of space. Similarly, analytic solutions to thick coil magnets have been derived to facilitate the computation of the magnetic field for an arbitrary configuration of magnets used in the KATRIN experiment. With these techniques, the electrostatic and magnetostatic fields used in KATRIN can be computed everywhere.

Using zonal harmonic expansion techniques, it has been demonstrated that the electric and magnetic fields from an axially symmetric configuration of electrodes and coil magnets can be rapidly computed with high accuracy in regions where repeated field calculations are often necessary in simulation. Approximations have been described for nearly axially symmetric systems, allowing these techniques to be applied to a larger subset of electrode configurations (including those present in KATRIN's pre- and main spectrometers). As a result, the zonal harmonic expansion techniques

provide methods for rapidly computing KATRIN's electromagnetic fields within its regions of applicability.

Bridging these two techniques, an adaptive-refinement field mapping method has been introduced for the purpose of fast and accurate calculations in regions where zonal harmonic expansions fail to converge. By computing field maps over regions where repeated field calculation is necessary but computationally expensive, it is possible to construct arbitrary regions in space where the field is readily and quickly calculable. This allows for rapid field computation in the entire KATRIN experiment, with no regions of exemption.

Most importantly, the `KatrinField` program utilizes these three field-solving techniques all together, offsetting the weaknesses of one method with the strengths of another. The interplay of these techniques within a cohesive object-oriented structure allows for `KatrinField` to be used ubiquitously across all of KATRIN's simulation projects. As different techniques and improvements upon the existing methods for field computation emerge, it will be possible to augment this framework as necessary, providing a uniform means of electromagnetic computation for the KATRIN experiment.

Appendix A

Formulae for the potential of a right triangular sub-element

```
double I_3(double a,double b,double u)
{
    // This function computes the following indefinite integral
    // analytically:
    //  $F = \int du \operatorname{asinh}((a + b*u)/((u^2 + 1)^{(1/2)}))$ 
    // This came out of
    // Mathematica

    double p[12]; // repeated values calculated beforehand to
                  // increase speed

    p[0] = a*a;    // a^2
    p[1] = a*p[0]; // a^3
    p[2] = a*p[1]; // a^4
    p[3] = a*p[2]; // a^5
    p[4] = a*p[3]; // a^6
    p[5] = b*b;    // b^2
```

```

p[6] = b*p[4]; // b^3
p[7] = b*p[5]; // b^4
p[8] = b*p[6]; // b^5
p[9] = u*u; // u^2
p[10] = sqrt(1 + p[0] + 2*a*b*u + (1 + p[5])*p[9]);
p[11] = sqrt(1 + p[5]);

```

```

double value = u*asinh((a + b*u)/sqrt(1 + p[9])) +
  (atan((p[2]*b*p[10] +
    2*p[0]*p[6]*
    p[10] +
    p[8]*p[10] -
    p[3]*(2*b*(1 + p[9]) +
    u*p[10]) +
    a*p[6]*(2*(1 + p[5])*(1 + p[9]) -
    b*u*p[10]) -
    2*p[1]*b*(1 + p[9] +
    b*u*p[10])))/
  (p[4] + 2*p[3]*b*u +
    4*p[1]*p[6]*u + 2*a*p[8]*u +
    p[7]*(1 + (1 + p[5])*p[9]) -
    p[0]*p[5]*
    (2 + 3*p[5] + 2*(1 + p[5])*p[9]) +
    p[2]*(1 + p[9] -
    p[5]*(2 + 3*p[9])))) -
  atan((-p[2]*b*
    p[10]) -
    2*p[0]*p[6]*
    p[10] -
    p[8]*p[10] +

```

```

    p[3]*(-2*b*(1 + p[9]) +
        u*p[10]) +
    2*p[1]*b*(-1 - p[9] +
        b*u*p[10]) +
    a*p[6]*(2*(1 + p[5])*(1 + p[9]) +
        b*u*p[10]))/
    (p[4] + 2*p[3]*b*u +
        4*p[1]*p[6]*u + 2*a*p[8]*u +
        p[7]*(1 + (1 + p[5])*p[9]) -
        p[0]*p[5]*
            (2 + 3*p[5] + 2*(1 + p[5])*p[9]) +
        p[2]*(1 + p[9] -
            p[5]*(2 + 3*p[9])))) +
    (2*a*log(u + b*(a + b*u) +
        sqrt((1 + p[5])*
            (1 + p[0] + 2*a*b*u +
                (1 + p[5])*p[9]))))/
    p[11])/2.;

return value;
}

double I_4(double a, double u)
{
    // This function computes the following indefinite integral
    // analytically:
    // F=\int du \asinh(a/((u^2 + 1)^(1/2))). This came out of
    // Mathematica.

    double p[2]; // repeated values calculated beforehand to

```

```
        // increase speed

    p[0] = sqrt(1. + u*u);
    p[1] = sqrt(1. + a*a + u*u);

    double value = u*asinh(a/p[0]) - atan(a*u/p[1]) + a*log(u + p[1]);

    return value;
}
```

Appendix B

Zonal Harmonic Expansion Relations

B.1 Recursion relation for the remote source points of a solenoid

Beginning with

$$\psi_n^{rem}|_{z_0} = \frac{\sin^2(\theta(Z))}{\rho_{rem}} \left(\frac{\rho(Z)}{\rho_{rem}} \right)^n P'_{n-1}(\cos(\theta(Z))), \quad (\text{B.1})$$

where

$$\rho(Z) = \sqrt{R^2 + (Z - z_0)^2} \quad (\text{B.2})$$

and

$$\theta(Z) = \arccos\left(\frac{Z - z_0}{\rho(Z)}\right), \quad (\text{B.3})$$

we set out to prove that

$$\psi_n^{rem}|_{z_0} = \frac{\rho_{rem}}{n+1} \cdot \frac{\partial}{\partial Z} (\psi_{n+1}^{rem}|_{z_0}). \quad (\text{B.4})$$

To do so, we will employ the following identities involving Legendre polynomials [49]:

$$\frac{\partial^n(\cos(\theta))}{\partial Z^n} = (-1)^{(n-1)} \cdot \frac{(n-1)!}{\rho^n} \cdot \sin^2(\theta) \cdot P'_n(\cos(\theta)), \quad (\text{B.5})$$

and

$$(2n + 1) \cdot \cos(\theta) \cdot P'_n(\cos(\theta)) = n \cdot P'_{n+1}(\cos(\theta)) + (n + 1) \cdot P'_{n-1}(\cos(\theta)), \quad (\text{B.6})$$

as well as the relation

$$\frac{\partial}{\partial Z} (\rho^n) = n(Z - z_0)\rho^{(n-2)}. \quad (\text{B.7})$$

We begin by applying Equation B.5 to $\psi_{n+1}^{rem}|_{z_0}$, converting it into a form with no explicit Legendre polynomials:

$$\psi_{n+1}^{rem}|_{z_0} = \frac{1}{\rho_{rem}} \cdot \left(\frac{\rho}{\rho_{rem}}\right)^{(n+1)} \cdot \frac{(-1)^{(n-1)}}{(n-1)!} \cdot \rho^n \cdot \frac{\partial^n(\cos(\theta))}{\partial Z^n}. \quad (\text{B.8})$$

By applying the product rule in tandem with Equation B.7, we take the derivative of Equation B.8 with respect to Z :

$$\begin{aligned} \frac{\partial}{\partial Z} (\psi_{n+1}^{rem}|_{z_0}) &= \left(\frac{1}{\rho_{rem}}\right)^{(n+2)} \cdot \frac{(-1)^{(n-1)}}{(n-1)!} \cdot \frac{\partial}{\partial Z} \left[\rho^{(2n+1)} \cdot \frac{\partial^n(\cos(\theta))}{\partial Z^n} \right] = \\ &= \left(\frac{1}{\rho_{rem}}\right)^{(n+2)} \cdot \frac{(-1)^{(n-1)}}{(n-1)!} \cdot \left[(2n + 1) \cdot (Z - z_0) \cdot \rho^{(2n-1)} \cdot \frac{\partial^n(\cos(\theta))}{\partial Z^n} + \right. \\ &\quad \left. + \rho^{(2n+1)} \cdot \frac{\partial^{(n+1)}(\cos(\theta))}{\partial Z^{(n+1)}} \right]. \end{aligned} \quad (\text{B.9})$$

We now substitute explicit terms for the Legendre polynomials back into Equation B.9:

$$\begin{aligned} \frac{\partial}{\partial Z} (\psi_{n+1}^{rem}|_{z_0}) &= \left(\frac{1}{\rho_{rem}}\right)^{(n+2)} \cdot \left[(2n + 1) \cdot \rho^n \cdot \cos(\theta) \cdot \sin^2(\theta) \cdot P'_n(\cos(\theta)) - \right. \\ &\quad \left. - n \cdot \rho^n \cdot \sin^2(\theta) \cdot P'_{n+1}(\cos(\theta)) \right]. \end{aligned} \quad (\text{B.10})$$

Equation B.10 can be simplified by substituting Equation B.6 for P'_n , leaving us with

$$\frac{\partial}{\partial Z} (\psi_{n+1}^{rem}|_{z_0}) = \left(\frac{\rho}{\rho_{rem}}\right)^n \cdot \frac{1}{\rho_{rem}^2} \cdot [(n + 1) \cdot \sin^2(\theta) \cdot P'_{n-1}(\cos(\theta))]. \quad (\text{B.11})$$

Finally, we substitute Equation B.1 into B.11, yielding the recursion relation that we

set out to find:

$$\frac{\partial}{\partial Z} (\psi_{n+1}^{rem}|_{z_0}) = \frac{(n+1)}{\rho_{rem}} \cdot \psi_n^{rem}|_{z_0}. \quad (\text{B.12})$$

B.2 Relating the boundary conditions for a solenoid to the boundary conditions for two rings at its edges

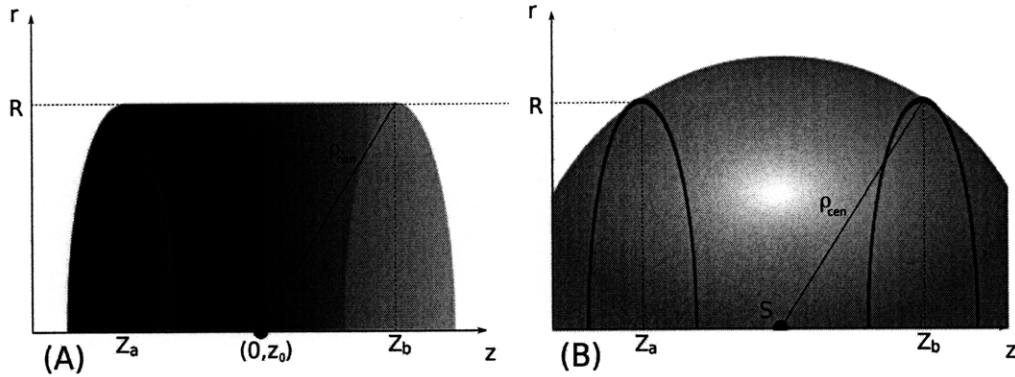


Figure B-1: (A) A 3-dimensional rendering of an axially symmetric solenoid and (B) the regions of convergence for central zonal harmonic expansion of the z and r -components of the magnetic field from a source point S . In both images, $(Z_a - z_0) = (z_0 - Z_b)$ (in other words, the source point is located in the middle of the geometries).

In this section, we show that the central region of convergence for the magnetic fields of a solenoid is equivalent to the central region of convergence for the magnetic scalar potential of two rings located at the edges of the solenoid, each with a current \vec{I} related to the surface current of the solenoid by

$$\frac{|\vec{I}|}{\rho_{cen}} = |\vec{k}|, \quad (\text{B.13})$$

and where $\frac{\vec{I}_2}{|I_2|} = \frac{\vec{k}}{|k|}$.

We begin by drawing a relationship between the source constants for the geometries depicted in Figures B-1(A) and B-1(B). Recalling the general equation for the

source constant from a ring (Eq. 4.44),

$$\psi_n^{cen}|_{z_0}(Z) = \frac{\sin^2(\theta(Z))}{\rho_{cen}} \left(\frac{\rho_{cen}}{\rho(Z)} \right)^{(n+1)} P'_{n+1}(\cos(\theta(Z))), \quad (\text{B.14})$$

we can determine the source constants for the solenoid from Equation 4.62 to be

$$\tilde{\Psi}_n^{cen}|_{z_0} = -\frac{\mu_0 \cdot |\vec{k}|}{2} \cdot \frac{\rho_{cen}}{n} \cdot [\psi_{n-1}^{cen}|_{z_0}(Z_b) - \psi_{n-1}^{cen}|_{z_0}(Z_a)]. \quad (\text{B.15})$$

From Equation 4.44, the source constants for the pair of rings is

$$\Psi_n^{cen}|_{z_0} = \frac{\mu_0 \cdot |\vec{I}|}{2} \cdot [\psi_n^{cen}|_{z_0}(Z_b) - \psi_n^{cen}|_{z_0}(Z_a)]. \quad (\text{B.16})$$

Comparing Equations B.15 and B.16, we can immediately see that

$$\Psi_n^{cen}|_{z_0} = -\tilde{\Psi}_{n+1}^{cen}|_{z_0} \cdot (n+1). \quad (\text{B.17})$$

Now that we have a relationship between the source constants of the two geometries, we can draw comparisons between their formulae for computing the scalar potential and magnetic fields. From Equation 4.35 B_z^S , the z-component of the magnetic field for the solenoid, becomes

$$\begin{aligned} B_z^S &= \sum_{n=0}^{\infty} \tilde{\Psi}_n^{cen}|_{z_0} \left(\frac{\rho}{\rho_{cen}} \right)^n P_n(\cos \theta) = \\ &= \tilde{\Psi}_0^{cen}|_{z_0} - \sum_{n=1}^{\infty} \Psi_{n-1}^{cen}|_{z_0} \cdot \frac{\rho_{cen}}{n} \cdot \left(\frac{\rho}{\rho_{cen}} \right)^n \cdot P_n(\cos \theta) = \\ &= \tilde{\Psi}_0^{cen}|_{z_0} - \sum_{n=0}^{\infty} \Psi_n^{cen}|_{z_0} \cdot \frac{\rho_{cen}}{(n+1)} \cdot \left(\frac{\rho}{\rho_{cen}} \right)^{(n+1)} \cdot P_{n+1}(\cos \theta). \end{aligned} \quad (\text{B.18})$$

Now, the summation in Equation B.18 is precisely that describing the magnetic scalar potential for the two-loop configuration, Ψ^L (from Equation 4.33):

$$\Psi^L = \sum_{n=0}^{\infty} \Psi_n^{cen}|_{z_0} \cdot \frac{-\rho_{cen}}{(n+1)} \cdot \left(\frac{\rho}{\rho_{cen}} \right)^{(n+1)} \cdot P_{n+1}(\cos \theta). \quad (\text{B.19})$$

We can now rewrite Equation B.18 as

$$B_z^S = \tilde{\Psi}_0^{cen}|_{z_0} + \Psi^L, \quad (\text{B.20})$$

which, since $\tilde{\Psi}_0^{cen}|_{z_0} = 0$ from Equation 4.58, clearly has the same convergence region as the 2-loop system.

Equation 4.36 gives us B_r^S , the r -component of the magnetic field for the solenoid:

$$\begin{aligned} B_r^S &= -\sin\theta \sum_{n=1}^{\infty} \tilde{\Psi}_n^{cen}|_{z_0} \left(\frac{1}{n+1}\right) \left(\frac{\rho}{\rho_{cen}}\right)^n P'_n(\cos\theta) = \\ &= \sin\theta \sum_{n=1}^{\infty} \Psi_{n-1}^{cen}|_{z_0} \left(\frac{\rho_{cen}}{n(n+1)}\right) \left(\frac{\rho}{\rho_{cen}}\right)^n P'_n(\cos\theta). \end{aligned} \quad (\text{B.21})$$

Recalling the equation for the scalar potential of the 2-loop configuration, Equation B.19 can be rewritten as

$$\Psi^L = \sum_{n=1}^{\infty} \Psi_{n-1}^{cen}|_{z_0} \left(\frac{-\rho_{cen}}{n}\right) \left(\frac{\rho}{\rho_{cen}}\right)^n P_n(\cos\theta). \quad (\text{B.22})$$

Since Ψ^L is an *analytic* function over its region of convergence, we are guaranteed that the derivative of Equation B.22 with respect to θ must also converge in the same region. Taking this derivative, we get

$$\frac{\partial \Psi^L}{\partial \theta} = \sin\theta \cdot \sum_{n=1}^{\infty} \Psi_{n-1}^{cen}|_{z_0} \left(\frac{\rho_{cen}}{n}\right) \left(\frac{\rho}{\rho_{cen}}\right)^n P'_n(\cos\theta). \quad (\text{B.23})$$

By comparing the terms of Equations B.21 and B.23, we can see that every term in B_r^S is smaller than the respective term in $\frac{\partial \Psi^L}{\partial \theta}$ by a factor of $\left(\frac{1}{n+1}\right)$. We can therefore state that Equation B.21 is guaranteed to converge in the same region as B.23.

Appendix C

KatrinField

KatrinField is a toolkit written in C++ for solving electrostatic and magnetostatic fields by employing the techniques outlined in Chapters 3, 4 and 5. At its inception, KatrinField was merely a port of the existing algorithms of Dr. Ferenc Glueck [44] into an object-oriented framework for use in GEANT4 [65] simulations of the Katrin experiment. It has since been augmented to include refinements of the existing techniques and new methods for field computation, with the intention of its use as a more general framework for electrostatic and magnetostatic field computation.

The toolkit is partitioned into the following components:

- **Geometry:** container classes that hold the various geometry primitives for use in field calculation,
- **Elliptic:** routines for directly calculating the electric and magnetic fields using the methods described in Chapter 3,
- **Legendre:** routines and container classes for creating, storing and implementing the central and remote zonal harmonic expansions outlined in Chapter 4,
- **FieldMap:** routines for the creation and application of field maps described in Chapter 5,
- **Field:** a master container class that holds the geometry and field methods, and classes to control the input and output for the geometry and the parameters of the individual field methods, and

- **Test:** simple programs that demonstrate the utility of the `KatrinField` toolkit.

With the exception of the test programs, the general properties of each of these components are described in this chapter (the results of the test programs can be found in Chapter 6).

In its current form, the `KatrinField` toolkit is complete: all of the geometry primitives and field methods described in this thesis are fully implemented. It is static, however, and additional geometry primitives and field solving methods cannot be included without altering the existing routines. The next iteration will attempt to make the toolkit more dynamic, allowing users to easily construct additional geometry primitives and field solving techniques without affecting the existing routines or the program structure. In doing so, `KatrinField` will be applicable to more general tasks requiring field calculation, making it more valuable to a larger subset of the physics community.

C.1 Components of `KatrinField`

C.1.1 Geometry

Geometry primitives

Geometry primitives describe the actual sub-elements which comprise the geometry of the simulation. The available geometry primitives for use in `KatrinField` are described in Table C.1.

Depending on their symmetry properties, primitives are either represented as singular instances or as collections of identical sub-elements repeated about the z -axis. For example, a `ConicSect` describes a single conic section electrode with only one placement in the system because it is naturally axially symmetric, whereas a `Wire` describes a collection of multiply placed wire segments about the azimuthal axis (see Fig. 4-5 for a graphical representation). Each collective primitive has associated with it a list of coordinates (like `WireCoord`, for example) that describes the locations of each primitive in the collection.

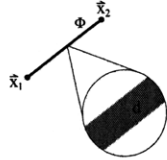
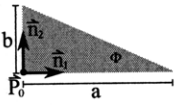
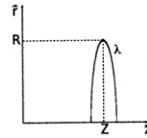
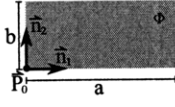
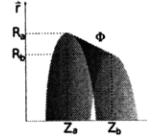
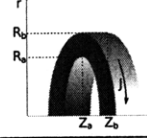
Geometry Primitive	Graphical Description	Axially Symmetric	Associated Classes
Wire		no	WireGroup Wire WireCoord
Triangle		no	TriGroup Triangle TriCoord
Ring		yes	Ring
Rectangle		no	RectGroup Rectangle RectCoord
Conic Section		yes	ConicSect
Thick Coil		yes	CoilGroup Coil

Table C.1: Available geometry primitives.

The description of wires, rectangles and triangles as repeated copies has several advantages. While individual placements of these primitives would break the axial symmetry of a system, multiply repeated instances about the azimuthal axis allow us to partially recover this symmetry. For geometries that have multiply repeated primitives (such as the wires in Katrin's main spectrometer [28]), we can approximate these geometry collections with axially symmetric sub-elements, enabling the use of the zonal harmonic expansion technique. In addition, we greatly reduce the number of independent sub-elements for which charge densities must be computed by effectively reducing the dimensionality of the system. For systems that have no axially symmetric

approximation, the user can simply treat each instance of these sub-elements as having only one copy.

Geometry approximations

If a field calculation is sufficiently far from a collection of asymmetric electrode primitives, it is beneficial to approximate the collection with a simpler sub-element. The example of substituting a `Wire` with a `ConicSect` to recover the technique of zonal harmonic expansion has already been described in Section 4.2.3. Similarly, `Wire`, `Rectangle` and `Triangle` collections may each be approximated as an axially symmetric `Ring`. The parameters that determine when these approximations hold valid are compared against the ratio of the size of the sub-element to its distance from the field point, and also by how many repeated instances of the primitive are in the collection. When the approximation of an entire electrode collection as a single axisymmetric electrode cannot be used (for example, if the field point is too close to one of the electrodes in the collection), the remaining electrodes in the collection can sometimes be approximated as a simple point charge. The point charge approximation exists for individual `Rectangle` and `Triangle` instances when the area of the sub-element surface is small compared to its distance from the field point. In the current iteration of `KatrinField`, the parameters that determine when to use geometry approximations are defined by the user.

Geometry groups

To reduce the number of independent electrode sub-elements even further, it is possible to collect asymmetric primitive collections into groups that have the same potential, and approximate the the charge density across them as equal.¹ While this process effectively reduces the accuracy of the field calculation, it is often necessary to restrict the number of independent sub-elements present in the system, as the time cost of computing the charge densities is proportional to the cube of the number of independent sub-elements [44]. Each primitive group (like `WireGroup`, for example)

¹We are essentially extending the first approximation discussed in Section 3.2.7 to a larger surface.

contains a list of the sub-elements that belong to the group, as well as their collective potential and charge density. If the user does not wish to group electrode primitives in this manner, each asymmetric electrode can be defined as the sole member of an electrode group.

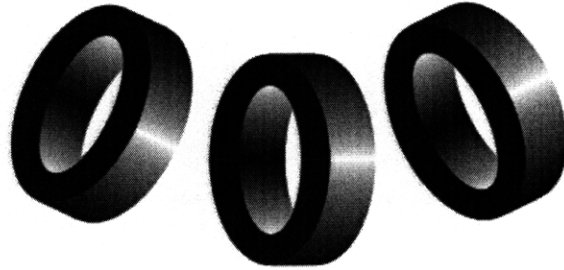


Figure C-1: A graphical representation of magnetic coils that share different axes.

Magnetic coils are also collected into groups, where each group of coils shares a common axis of symmetry. This facilitates the computation of the magnetostatic field in systems that have *tilted coils*, like those present in KATRIN's transport system (see Fig. C-1) [28]. By separating the coils in this fashion, we can use the zonal harmonic expansion technique to compute the magnetic field as a superposition of multiple axisymmetric systems.

Geometry containers

The geometry containers `E_Geometry` and `B_Geometry` hold `TClonesArrays`² of the geometry primitives that contribute to the electric and magnetic fields, respectively. In addition, `E_Geometry` contains methods for discretizing an electrode into smaller sub-elements, so that the approximation of constant charge density across a single sub-element holds valid. There is also a left/right symmetry parameter, which mirrors the electrode geometry across a plane normal to the z -axis at a specified z -coordinate. Since certain subsections of the KATRIN experiment contain electrodes that possess

²A `TClonesArray` is special type of array in ROOT [66] that is optimized to hold repeated instances of simple objects. It is optimized to increase the speed of data access and to minimize storage memory.

this symmetry, the left/right symmetry parameter is merely a means to simplify the geometry definitions.

C.1.2 Elliptic

The primary utility of the two classes `Elliptic_EField` and `Elliptic_BField` is to loop over all of the geometry primitives and apply the formulae derived in Chapter 3 to directly compute the electric and magnetic field, respectively, as a sum of the contributions from each primitive. Because it holds the direct calculation methods for computing the electric potential from each of the electrode types, `Elliptic_EField` also contains the method for computing the charge densities on all of the electrodes. To compute the charge densities, Equation 3.29 is solved via Gaussian elimination using ROOT's linear algebra package [66]. `Elliptic_EField` is also responsible for creating the additional primitives that can approximate the field produced from more complex geometry configurations, and holds the parameters that determine when these approximating primitives are valid.

C.1.3 Legendre

When a geometry is, or can be approximated as, axially symmetric, `Legendre_EField` and `Legendre_BField_1Group` contain the routines for computing and implementing the zonal harmonic expansion technique described in Chapter 4. Since each coil group has a different axis of symmetry, `Legendre_BField_1Group` implements the technique for only one coil group, while the container class `Legendre_BField` computes the aggregate field from all of the coil groups using a combination of the zonal harmonic expansion and direct calculation techniques. User-defined inputs are used to define the convergence parameters of the expansions (see Sec. C.1.5).

In order to maximize the utility of the technique, multiple remote and central source points are used to cover a larger net region of convergence (see Fig. C-2). The locations of these source points are determined using parameters set by the user. By default, the locations of the first and last field points are determined by the geometry.

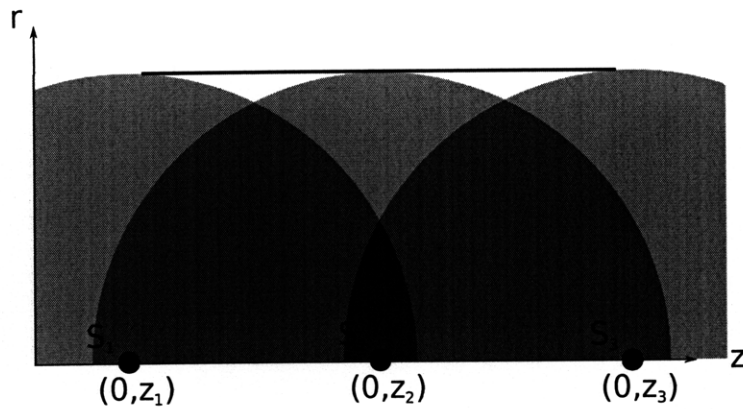


Figure C-2: A graphical representation of the central regions of convergence for three source points. Within each region of convergence, the coefficients corresponding to the nearest source point can be used in an expansion to solve for the fields. By using multiple source points, the technique of zonal harmonic expansion can be applied in a larger region of space.

The positions of these source points, their radii of convergence and source constants are held in the container class `SourcePoints`.

C.1.4 FieldMap

General structure

Both 2 and 3-dimensional field maps are created using the methods described in Chapter 5. The class `FieldMap_dD` (where $d = 2, 3$) contains all of the `MetaCube_dD` instances that comprise the field map, as well as the routines for construction and implementation³. Each `MetaCube_dD` instance in the map contains two ROOT TTrees organized as linear 2^d -trees comprising repeated `FieldPoint_dD` and `InterpolationCube_dD` instances, and searching algorithms for navigating the TTrees. In addition, each `FieldMap_dD` instance has a `FieldMapHeader` that holds persistent parameters describing the map. Because field maps continuously interact with precisely organized files, the saving and retrieval of persistent field map data occurs within the individual `MetaCube_dD` instances, rather than being controlled by a higher-level class.

³A `MetaCube_dD` is the class representation of the meta-box described in Section 5.3.3.

Tree splitting

To prevent individual files in the field map from becoming too large, `FieldMap_dD` also contains a method for automatically splitting meta-boxes into smaller meta-boxes during the creation of the map. This prevents the premature completion of a given region of the field map due to file size constraints, which would otherwise cause the field map to have disparate accuracies across the map. The maximum size for an individual file in the field map is set to 2 GigaBytes, a commonly accepted file size limit in modern computing.

Parallel computaton

Because the creation of a field map is a very time and CPU-intensive task, `FieldMap_dD` has been written with an optional mode that allows users to construct the field map using parallel computation techniques. `KatrinField` is currently being designed to run routines for field map generation on a computer grid, using MPI protocols [64] to facilitate field map construction that is uniformly distributed across the grid.

C.1.5 Field

The class `KatrinField` (which shares the name of the toolkit) holds the geometry containers and field solving methods and is responsible for the high-level functioning of the toolkit, such as the initialization and implementation of the geometry and field-solving classes. The order in which computations are carried out is dictated by this class to be *legendre* \rightarrow *fieldmap* \rightarrow *elliptic*, to ensure that the fastest applicable method is used for a given field point. The `KatrinField` class also contains methods for input and output for the geometry descriptions and the zonal harmonic expansion source points and coefficients, and can compare active geometry configurations against those saved to file (field map-specific data is handled by the field map classes themselves).

The class `KatrinField` also contains a subclass `ParameterConfig`, which is responsible for setting the parameters for the components of the toolkit. `ParameterConfig`

KatrinField component	Parameter	Description	Default value
Geometry	wireDiscPower	determines the distribution of the Wire sizes	2
	wireDiscScale	# of Wire sub-elements is \propto scale	4
	conicSectDiscPower	determines the distribution of conicSect sizes	2
	conicSectDiscScale	# of conicSect sub-elements is \propto scale	4
	isSymmetric	boolean flag for electrode left/right symmetry	false
	isAxiallySymmetric	boolean flag for electrode axial symmetry	true
	zMirror	z -coordinate of the plane of left/right electrode symmetry	~
(e/b)GeometryVerbose	verbose level for geometry (0 to 5)	1	
Elliptic	rectGroupToRingApproxParam	approximates RectGroup/TriGroup as Ring	0.15
	rectCoordToPSApproxParam	approximates single Rectangles/Triangles as point sources	40
	wireToConicSectApproxParam	approximates WireGroup as ConicSect	3
	wireGroupToRingApproxParam	approximates WireGroup as Ring	0.15
(e/b)EllipticVerbose	verbose level for direct \vec{E}/\vec{B} -field calculation (0 to 5)	1	
Legendre	(e/b)FieldProxToSP	restricts expansion if field point is close to source point	1.e-12 m
	(e/b)FieldConvergenceParam	ratio of final term in expansion to total sum of expansion	1.e-15
	(e/b)FieldConvergenceRatio	ratio of max. radius of convergence relative to $\rho_{cen/rem}$.99
	(e/b)FieldDel_z	distance between source points along z -axis	0.04 m
	(e/b)FieldNRemoteCoeffs	# of coefficients used in remote expansion	500
	(e/b)FieldNCentralCoeffs	# of coefficients used in central expansion	500
(e/b)LegendreVerbose	verbose level for zonal harmonic expansion of \vec{E}/\vec{B} -field (0 to 5)	1	
FieldMap	eFieldIsFieldMap	boolean flag for using a field map	false
	eFieldMaxCubeSize	size of the highest-level cube in map	0.5 m
	eFieldNLevel	# of levels in map	5
	eFieldTolerance	accuracy of the map	1.e-6
	eField(X/Y/Z)Min	minimum $x/y/z$ -coordinate of map	~
	eField(X/Y/Z)Max	maximum $x/y/z$ -coordinate of map	~
eFieldMapVerbose	verbose level for field map (0 to 5)	1	
Field	fieldVerbose	verbose level for main class & I/O routines (0 to 5)	1

Table C.2: Table of available parameters to be set by the user.

operates in a similar fashion to a Messenger class within the GEANT4 framework [65], and is designed to accept arguments written in the form of a GEANT4 macro. Table C.2 lists the available parameters that can be set by the user.

C.2 Summary

In its current form, the KatrinField toolkit is capable of taking as input complex geometries comprised of multiple user-defined geometry primitives, and outputting the electric and magnetic fields that result from these geometries using the techniques described in Chapters 3, 4 and 5. By utilizing ROOT's preexisting routines for optimized input and output of data to persistent memory, the toolkit is able to distinguish between multiple geometries and reuse previously computed charge densities, source points and field maps in order to facilitate the repeated testing of geometry configurations. The interaction between complementary field-solving methods within the toolkit produces a unified field calculation method that is faster and more comprehen-

sive than any singular method. While a subsequent iteration is required to achieve more flexibility and utility to the greater physics community, `KatrinField` is currently well suited for use in many simulations of the electrostatic and magnetostatic fields present in the KATRIN experiment.

Bibliography

- [1] S. Eidelman et al., *Review of Particle Physics*. Phys. Lett. B 592, 1, <http://pdg.lbl.gov>, 2004.
- [2] B. T. Cleveland et al., *Measurement of the solar electron neutrino flux with the Homestake chlorine detector*. Astrophys. J. 496, 505, 1998.
- [3] J. N. Abdurashitov et al., Phys. Rev. Lett. 77:4708, 1996.
- [4] W. Hampel et al., Phys. Lett. B447:127, 1999.
- [5] Y. Fukuda et al., *Evidence for Oscillation of Atmospheric Neutrinos*. Phys. Rev. Lett. Vol. 81, Num. 8, 1998.
- [6] Peter Fisher, Boris Kayser and Kevin S. McFarland, *Neutrino Mass and Oscillation*. arXiv:hep-ph/9906244v1, 1999.
- [7] Q. R. Ahmad et al., *Measurement of the Rate of $\nu_e + d \rightarrow p + p + e^-$ Interactions Produced by 8B Solar Neutrinos at the Sudbury Neutrino Observatory*. Phys Rev Lett 87 071301. 2001.
- [8] T. Araki et al., *Measurement of Neutrino Oscillation with KamLAND: Evidence of Spectral Distortion*. Phys Rev Lett 94 081801. 2005.
- [9] M. Agleilta et al., Europhys. Lett. 8:611, 1989.
- [10] W. Allison et al., Phys. Lett. B391:491, 1997.
- [11] R. Becker-Szendy, et al., Phys. Rev. D46:3720, 1992.

- [12] Ch. Berger et al., *Phys. Lett.* B227:489, 1989.
- [13] Y. Ashie et al., *Measurement of atmospheric neutrino oscillation parameters by Super-Kamiokande I*. *Physical Review D* 71, 112005. 2005.
- [14] M. H. Ahn et al., *Measurement of Neutrino Oscillation by the K2K Experiment*. arXiv:hep-ex/0606032v3. 2006.
- [15] P. Adamson et al., *A Study of Muon Neutrino Disappearance Using the Fermilab Main Injector Neutrino Beam*. arXiv:0711.0769v1, 2007.
- [16] M. C. Gonzalez-Garcia, *Global Analysis of Neutrino Data*. arXiv:hep-ph/0410030v1. 2004.
- [17] B. Aharmim et al., *Independent Measurement of the Total Active ^8B Solar Neutrino Flux Using an Array of ^3He Proportional Counters at the Sudbury Neutrino Observatory*. *Phys. Rev. Lett.* 101, 111301. 2008.
- [18] Stewart J. Freedman and Boris Kayser, *The Neutrino Matrix*. arXiv:physics/0411216 v2, 2004.
- [19] Kai Zuber, *Neutrino Physics*. IOP Publishing Ltd, 2004.
- [20] J. M. Conrad, *Neutrino Experiments*. arXiv:hep-ex/0708.2446v1. 2008.
- [21] P. D. B. Collins, A. D. Martin and E. J. Squires, *Particle Physics and Cosmology*. John Wiley & Sons, Inc. 1989.
- [22] H. V. Klapdor-Kleingrothaus and I. V. Krivosheina, *The Evidence for the Observation of $0\nu\beta\beta$ Decay: The Identification of $0\nu\beta\beta$ Events From the Full Spectra*. *Mod. Phys. Lett. A* V. 21, No. 20, p. 1547. 2006.
- [23] Benjamin Monreal, *Personal correspondence*.
- [24] John. G. Learned, Stephen T. Dye, Sandip Pakvasa and Robert C. Svoboda, *Determination of Neutrino Mass Hierarchy and θ_{13} With a Remote Detector of Reactor Antineutrinos*. hep-ex/0612022, 1998.

- [25] D. Ayres et al., *Letter of Intent to build an Off-axis Detector to study ν_μ to ν_e oscillations with the NuMI Neutrino Beam*. arXiv:hep-ex/0210005, 2002.
- [26] Y. Itow et al., *The JHF-Kamioka neutrino project*. hep-ex/0106019, 2001.
- [27] A. Osipowicz et al., *KATRIN: A next generation tritium beta decay experiment with sub-eV sensitivity for the electron neutrino mass*. hep-ex/0109033. 2001.
- [28] J. Angrik et al., *KATRIN Design Report 2004*. <http://www-ik.fzk.de/katrin>. 1996.
- [29] A. Picard et al., *A solenoid retarding spectrometer with high resolution and transmission for keV electrons*. Nuclear Instruments and Methods in Physics Research B63, 345-358. 1992.
- [30] J. D. Jackson, *Classical Electrodynamics: Third Edition*. John Wiley & Sons, Inc. 1998.
- [31] Jessica Dunmore, *Pixelation-Dependence of Transmission Function*, KATRIN internal document,
- [32] Karen Hugenberg, *Design of the electrode system for the KATRIN main spectrometer*. Diploma Thesis, Institut für Kernphysik, Westfälischen Wilhelms-Universität Münster, 2008.
- [33] M. Szilagy, *Electron and Ion Optics*. Plenum Press, New York. 1988.
- [34] D. Poljak and C. A. Brebbia, *Boundary Element Methods for Electrical Engineers*. WIT Press, Boston, 1st Edition, 2005.
- [35] W. S. Hall, *The Boundary Element Method*. Kluwer Academic Publishers, The Netherlands, 1st Edition, 1994.
- [36] D. J. Cartwright, *Underlying Principles of the Boundary Element Method*. WIT Press, Boston, 1st Edition, 2001.

- [37] Lothar Gaul, Martin Kögl and Marcus Wagner, *Boundary Element Methods for Engineers and Scientists*. Springer-Verlag, Berlin Heidelberg, 1st Edition, 2003.
- [38] C. A. Brebbia and R. Butterfield, *Boundary Element Techniques in Engineering*. Butterworth (Publishers) Inc., 1st Edition, 1980.
- [39] C. A. Brebbia and S. Walker, *Formal equivalence of direct and indirect boundary element methods*. Appl. Math. Modelling, Vol 2, 132-134, June 1978.
- [40] David J. Griffiths, *Introduction to Electrodynamics: Third Edition*. Prentice Hall. 1999.
- [41] Ferenc Glück, *New electric field calculation program for wire electrodes with support structure*. KATRIN internal document, 2006.
- [42] Ferenc Glück, *Axisymmetric electric field calculation by BEM and elliptic integrals*. to be published.
- [43] Ferenc Glück, *BEM electric field calculation for electrodes with discrete rotational symmetry*. to be published.
- [44] Ferenc Glück, *Untitled- research notes and personal correspondence*.
- [45] M. W. Garrett, *Calculation of Fields, Forces, and Mutual Inductances of Current Systems by Elliptic Integrals*. Journal of Applied Physics 34, 9. 1963.
- [46] Ferenc Glück, *Field and trajectory calculations with high accuracy and small computation time*. KATRIN internal document, 2006.
- [47] Ferenc Glück, *Magnetic field calculation of coils by elliptic integrals*. to be published.
- [48] E. Durand, *Électrostatique Tome I: Les Distributions*. Masson et C^{ie}. 1964.
- [49] M. W. Garrett, *Axially Symmetric Systems for Generating and Measuring Magnetic Fields. Part I*. Journal of Applied Physics 22, 9. 1951.

- [50] Ferenc Glück, *Magnetic field calculation of coils by zonal harmonic expansion*. to be published.
- [51] Ferenc Glück, *Axisymmetric electric field calculation by zonal harmonic expansion*. to be published.
- [52] V. Frerichs, W. G. Kaenders, and D. Meschede, *Analytic Construction of Magnetic Multipoles from Cylindric Permanent Magnets*. Applied Physics A 55, 242-249. 1992.
- [53] M. W. Garrett, *Thick Cylindrical Coil Systems for Strong Magnetic Fields with Field or Gradient Homogeneities of the 6th to 20th Order*. Journal of Applied Physics 38, 6. 1967.
- [54] Kendall E. Atkinson, *An Introduction to Numerical Analysis*. John Wiley & Sons, Inc. 1989.
- [55] František Melkes, *Reduced Piecewise Bivariate Hermite Interpolations*. Numer. Math. 19, 326-340. 1972.
- [56] Kurt M. Christoffel, Joel M. Bowman, and Bastiaan J. Braams, *A local interpolation method for direct classical dynamics calculations*. Journal of Chemical Physics Volume 115, Number 24. 2001.
- [57] S. Carter, J. M. Bowman, B. J. Braams, *On using low-order Hermite interpolation in 'direct dynamics' calculations of vibrational energies using the code 'MULTIMODE'*. Chemical Physics Letters 342, 636-642. 2001.
- [58] A. Tabarraei, N. Sukumar, *Adaptive computations using material forces and residual-based error estimators on quadtree meshes*. Comput. Methods Appl. Mech. Engrg. 196 2657-2680. 2007.
- [59] Hanan Samet, *The Quadtree and Related Hierarchical Data Structures*. Computing Surveys, Vol. 16, No. 2, June 1984.

- [60] F. Lekien and J. Marsden, *Tricubic interpolation in three dimensions*. International Journal for Numerical Methods in Engineering, Vol. 63, pp.455-471, March 3 2005.
- [61] Philippe Flajolet, Gaston Gonnet, Claude Puech, and J. M. Robson, *Analytic Variations on Quadtrees*. Algorithmica 10:473-500. 1993.
- [62] F. H. Read, *Improved Extrapolation Technique in the Boundary Element Method to Find the Capacitances of the Unit Square and Cube*. Journal of Computational Physics 133, 1-5. 1997.
- [63] Chi-Ok Hwang, Michael Mascagni, *Electrical capacitance of the unit cube*. Journal of Applied Physics 99, 7. 2004.
- [64] *The Message Passing Interface (MPI) standard Homepage*. <http://www-unix.mcs.anl.gov/mpi/index.htm>, 2008.
- [65] S. Agostinelli et al., *GEANT4 - a simulation toolkit*. doi:10.1016/S0168-9002(03)01368-8. 2003.
- [66] Rene Brun and Fons Rademakers, *The ROOT System Home Page*. <http://root.cern.ch/>, 2008.